Universidade de Aveiro Departamento de Física
2017

José Daniel Lago da Silva Neves Gouveia

Propriedades magnéticas de sistemas electrónicos quânticos com geometrias não-triviais

Magnetic properties of quantum electronic systems with non-trivial geometries

José Daniel Lago da Silva Neves Gouveia

Propriedades magnéticas de sistemas electrónicos quânticos com geometrias não-triviais

Magnetic properties of quantum electronic systems with non-trivial geometries

Tese apresentada à Universidade de Aveiro para cumprimento dos requisitos necessários à obtenção do grau de Doutor em Física, realizada sob a orientação científica do Doutor Ricardo Assis Guimarães Dias, Professor Auxiliar do Departamento de Física da Universidade de Aveiro.

Apoio financeiro da FCT e do FSE no âmbito do
III Quadro Comunitário de Apoio

Aos meus pais, que são muito lindos, fazem comida deliciosa, e dão-me tudo sem pedir nada em troca.

the jury

presidente / president	Professor Doutor **Mário Guerreiro Silva Ferreira** Professor Catedrático da Universidade de Aveiro
vogais / examiners committee	Doutor **José Manuel Pereira Carmelo** Professor Catedrático da Universidade do Minho
	Doutor **Vitor José Babau Torres** Professor Catedrático da Universidade de Aveiro
	Doutora **Iveta Rombeiro do Rego Pimentel** Professora Associada da Faculdade de Ciências, Universidade de Lisboa
	Doutor **Eduardo Filipe Vieira de Castro** Professor Auxiliar do Instituto Superior Técnico, Universidade de Lisboa
	Doutor **Ricardo Guimarães Dias** Professor Auxiliar da Universidade de Aveiro (orientador)

acknowledgements

First and foremost, I would like to thank my parents, to whom I dedicate this work. The certainty that our parents are the ones who made our whole life possible is a feeling common to all of us. Thank you!

In terms of scientific advice and orientation, the hero is of course Professor Ricardo Dias. Aside from being the favorite teacher of almost every student that the Department of Physics of the UA has seen, he is also an extremely competent and motivating thesis supervisor. Thank you!

Professors Paula Carvalho, Sá Esteves and Alexander Plakhov, from the Department of Mathematics, were crucial for their assistance with some mathematical subtleties regarding saddle points and differential equations. Thank you!

I would also like to thank Ivo Maceira, alongside whom the calculations and numerical simulations related to the evolution of quantum states were performed. Thank you!

I thank my beautiful girlfriend Sara, for her enduring support, for making me a better person, for making me like dogs, for making me smile more, for making me eat healthier food, and for distracting me while I am trying to work. Thank you!

Finally, I thank all my friends, especially Alexandre. Were it not for their reminders, I would distractedly have skipped half the meals in the last years. Thank you!

keywords

Hubbard model, magnetism, mean-field, Hartree-Fock, decorated lattices, localized states, flat-band systems, Lieb lattice

abstract

The Hubbard model is one of the simplest models to describe the motion and interaction of electrons in solids. It has been widely studied due to its applications in the description of organic conductors and in the search for high-T_c superconductivity.

The aim of this thesis is to contribute for the better understanding of the behavior of the two-dimensional Hubbard model when the geometry of the lattice is changed, namely by twisting the boundary conditions or introducing geometric frustration.

We begin by extending the mean-field magnetic phase diagram of the Hubbard model in a square lattice, by adding the possibility of spin density modulation, in contrast with previous studies. This was done by considering a square lattice divided into two sublattices, which were allowed to have different spin densities. We found that, in some regions of the phase diagram, nonuniform spin density throughout the lattice leads to a lower free energy.

Secondly, we introduce a variation of the square lattice, which we call the helicoidal lattice. This lattice and the square lattice are equivalent in the thermodynamic limit, as they differ only in the boundary conditions. We present an effective Hamiltonian that describes the first-order energy corrections due to transversal hoppings in the strong-coupling limit, and show that interesting spin dynamics arises, even without the Heisenberg correction, due to hole hoppings in the transversal direction. We present an analytic expression for the energy correction in the case of one hole and one inverted spin. The numerically-obtained corrections for higher number of inverted spins are also shown.

Thirdly, we present a unifying picture for localized states of decorated square lattices. This unification is presented in the form of what we call the "origami rules", which include folding and unfolding localized states of tight-binding Hamiltonians. We show that localized states of decorated lattices of the Lieb, Mielke and Tasaki classes can be obtained from each other by applying these rules.

We then focus on the decorated lattices of the Lieb class. We begin by studying the time evolution of its localized states when a magnetic field is slowly applied perpendicularly to the plane of the lattice. We find that, as stated by the adiabatic theorem, the localized eigenstate remains localized as long as there is an energy gap between its energy and the rest of the Hamiltonian spectrum. Furthermore, we show that the way that the localized state evolves can be described by a simple three-level toy Hamiltonian, whose solution is analogous to a classical precession motion.

Lastly, we introduce the Hubbard interaction in the Lieb lattice and, using the mean-field approximation, obtain the magnetic phase diagram of this lattice, previously absent from the literature. We find that, in the case of bipartite lattices with a different number of atoms on each sublattice, the traditional mean-field approach fails to yield correct results at half-filling. Therefore, we follow a more complex (generalized Hartree-Fock) mean-field approach, which allows the sublattices to have different magnetizations and charge densities. Under these new considerations, the mean-field approach correctly reproduces the exact results at half-filling, given by Lieb's theorem and the uniform density theorem.

palavras-chave

modelo de Hubbard, magnetismo, campo médio, Hartree-Fock, redes decoradas, estados localizados, sistemas de *flat bands*, rede de Lieb

resumo

O modelo de Hubbard é um dos modelos mais simples para descrever o movimento e a interacção de electrões em sólidos. Tem sido largamente estudado pelas suas aplicações na descrição de condutores orgânicos e na procura de supercondutividade a cada vez mais altas temperaturas.

O objectivo desta tese é contribuir para a melhor compreensão do comportamento do modelo de Hubbard a duas dimensões quando a geometria da rede é alterada, nomeadamente torcendo as condições de fronteira ou introduzindo frustração geométrica.

Começa-se por fazer uma extensão do diagrama de fases magnéticas do modelo de Hubbard numa rede quadrada usando a aproximação de campo médio, introduzindo a possibilidade de modulação da densidade de *spin*, contrastando assim com estudos anteriores. Isto foi conseguido dividindo a rede quadrada em duas sub-redes, podendo as suas densidades de *spin* ser diferentes. Concluiu-se que, em algumas regiões do diagrama de fases, esta densidade de *spin* modulada permite ao sistema baixar a sua energia livre.

Em segundo lugar, introduz-se uma variação da rede quadrada, a que chamamos rede helicoidal. Estas duas redes são equivalentes no limite termodinâmico, visto que apenas diferem nas condições de fronteira. É apresentado um Hamiltoniano efectivo que descreve as correcções de energia em primeira ordem devidas aos saltos transversais no limite de acoplamento forte (*strong-coupling limit*). Devido à introdução destes saltos, observa-se uma dinâmica de *spins*, mesmo no limite de interacção electrónica infinita (ou seja, sem as correcções de Heisenberg). É apresentada uma expressão analítica para a correcção energética no caso de uma lacuna e um *spin* invertido, bem como representações gráficas das correcções para vários *spins* invertidos, obtidas numericamente.

Em terceiro lugar, apresenta-se uma unificação dos estados localizados de redes quadradas decoradas. Esta unificação é apresentada na forma de "regras de origami", que incluem dobrar e desdobrar estados localizados de Hamiltonianos sem interacções (*tight-binding*). Mostra-se que os estados localizados das redes decoradas de Lieb, Mielke e Tasaki podem ser obtidos uns a partir dos outros aplicando estas regras.

Seguidamente, dá-se ênfase às redes decoradas da classe de Lieb. Começa-se por estudar a evolução temporal dos seus estados localizados quando um campo magnético é aplicado lentamente e perpendicularmente ao plano da rede. Conclui-se que, em concordância com o teorema adiabático, o estado localizado mantém-se localizado desde que haja uma diferença energética finita entre a sua energia e o resto do espectro do Hamiltoniano. Além disto, mostra-se que a forma como o estado localizado evolui pode ser descrita por um Hamiltoniano mais simples, com apenas três níveis energéticos, cuja solução é análoga a um movimento de precessão clássico.

Finalmente, introduz-se a interacção de Hubbard na rede de Lieb e, usando a aproximação de campo médio, obtém-se o diagrama de fases magnéticas desta rede, previamente inexistente na literatura. Conclui-se que, no caso de redes bipartidas com diferente número de átomos em cada sub-rede, a abordagem de campo médio tradicional não reproduz resultados correctos na situação de um electrão por sítio (*half filling*). Posto isto, segue-se uma abordagem em campo médio mais complexa (Hartree-Fock generalizada), que permite que as sub-redes tenham diferentes magnetizações e densidades de carga. Com estas modificações, a nova abordagem de campo médio já reproduz correctamente os resultados exactos em *half filling*, dados pelo teorema de Lieb e pelo teorema da densidade uniforme.

Contents

Chapter 1

Introduction

While I was writing this thesis, I asked people who do not work in Physics what quantum mechanics was for them. In short, the answer was: the physics of very small things, which behave in random ways. As a follow-up, I was often asked the question "if these things behave randomly, isn't quantum mechanics pointless?" and, to their amazement, it turns out that it is not. While, from the classical point of view, quantum mechanics professes to describe a reality in which events in the future can affect the past, and particles can have several values of the same property at the same time or travel in two opposite directions simultaneously, it is responsible for many of the technological advances of the last hundred years. These include CD, DVD and Blu-ray players, extremely precise clocks, higher resolution microscopes, lasers, more and more miniaturized electronics, personal computers, and everything that contains transistors, and uncrackable codes. Even the whole field of chemistry (and through it, biology and medicine) would be no more than a huge set of mysterious rules which only apply to very few cases. Naturally, chemists would eventually and inevitably invent quantum mechanics when attempting to systematize all those rules.

At this point, the non-physicist person might ask "but if everything is random, how can there be controllable quantum mechanical devices?". And the answer is that, while there is a large set of probabilities (or realities), these probabilities are not necessarily random. We humans are so smart that we are able to use these simultaneous possibilities, this uncertainty, to our advantage. Quantum mechanics is therefore the branch of Physics which studies what these probabilities are, how we can affect them, and how they evolve. The transition from the quantum level to the macroscopic level still confounds the mind. At the quantum level, observation forces the many possibilities to become only one, chosen with a certain known probability. In the words of Pascual Jordan [1], "Observations not only disturb what has to be measured, they produce it. We compel [particles] to assume a definite position. We ourselves produce the results of measurements". Our common sense, however, dictates that at the macroscopic scale, the state of our surroundings does not depend on whether we are with our eyes open or closed. A well-known quote by Einstein, in one of his many denials of quantum physics, is given by Abraham Pais [2]: "We often discussed his notions on objective reality. I recall that during one walk Einstein suddenly stopped, turned to me and asked whether I really believed that the moon exists only when I look at it".

The Hubbard model

The state of a classical system is the set of all its (possibly time-dependent) properties. In contrast, the state of a quantum system is the set of all possible values for its properties, and their respective probabilities. The Schroedinger equation is a partial differential equation whose solution (the wave function) describes the evolution of a quantum system; the probability distribution equals the square of the absolute value of the wave function. Depending on the geometry of a system, not all probability distributions are possible. The Hubbard model [3] is the simplest model of interacting particles (fermions or bosons) in a lattice. Its solution provides the possible distributions of the particles in the lattice, and their respective energies, taking into account the energy gain due to particle mobility (the kinetic term, through the hopping parameter t) and the energy cost of particle proximity (the on-site interaction term, through the interaction parameter U). It works well for particles in periodic potentials at low temperatures. as long as long-range particle interactions are negligible.

The Bethe ansatz [4] was proposed in 1931 to find the exact eigenvalues and eigenvectors of the one-dimensional (1D) Heisenberg model, and was later extended to other models, such as the Hubbard model. It provides the solution of the Hubbard model in one dimension, which can be used to describe quasi-one-dimensional organic conductors. Nonetheless, it is the two-dimensional (2D) Hubbard model that has attracted the most interest, particularly since the discovery of high-temperature superconductivity, which was observed for example in yttrium barium copper oxides [5] (the first material known to exhibit superconductivity above 77 K), with a quasi-2D structure.

In 1D, it has been shown that the Hubbard model does not display long-range magnetic order [6, 7]. In 2D, the model has no exact solution, and is therefore studied using approximations such as mean-field theory, variational approaches, numerical Quantum Monte Carlo, or considering some limiting cases such as infinite on-site repulsion ($U \to \infty$). In three dimensions (3D), the ground state is known to be antiferromagnetic close to a half-filled band (one electron per lattice site) for high enough U [8]. The purpose of this thesis is motivated by the lack of knowledge we have on the transition from a 1D setting to a immensely different 3D one, in particular on the appearance of magnetic behavior. We focus on several 2D geometries, starting from the trivial case of a square lattice, and moving on to non-trivial lattices, such as the helicoidal lattice, and decorated square lattices, emphasizing the Lieb lattice. With the objective of better understanding them, we apply the Hubbard model to these lattices, either by solving it exactly in some cases or employing perturbation or mean-field theory.

At half-filling, the ground state of the Hubbard model in a square lattice is known to display antiferromagnetism, and is described by the Heisenberg antiferromagnetic exchange term [9]. If the number of electrons and the number of lattice sites differ by 1, Nagaoka's theorem predicts a ferromagnetic ground state [10]. Farther from half-filling, however, little is known. While mean-field calculations by Kanamori [11] state that for very large U, a system doped slightly away from half-filling is always ferromagnetic, Monte Carlo calculations by Vilk [12], state that the Hubbard model on a square lattice is never ferromagnetic. This contradiction serves to show that the Hubbard model is still far from understood.

A review by Marder [13] includes six phase diagrams of the 2D Hubbard model. The phase diagrams were obtained by six different groups, using a variety of approximations. Among the included diagrams, three are mean-field approaches: one where the allowed magnetic phases were paramagnetism, ferromagnetism, antiferromagnetism and ferrimagnetism [14], another which adds spiral states to the list of phases [15], and a third one which considers

finite temperature [16]. A fourth phase diagram is for a $\sqrt{10} \times \sqrt{10}$ square lattice and the authors find the magnetic phase diagram of the effective Hamiltonian in the strong-coupling limit, restricting the Hilbert space to states with only singly-occupied sites [17]. The last two diagrams were obtained using a variational [18] and a functional integral approach [19]. The diagrams are remarkably different despite corresponding to the same system.

Mean-field approximation

We know that we cannot truly speak about magnetic order in finite systems (or any other kind of order, for that matter, because phase transitions occur when the partition function has a singularity, and partition functions of finite systems do not display singularities). A theorem by Mermin and Wagner [20] states that at any finite temperature, one- and two-dimensional systems with finite-range exchange interaction can be neither ferromagnetic nor antiferromagnetic. Alas, all real-life systems are finite. Fortunately, macroscopic systems are so large that their behavior is very close to that of an infinite system. In addition, the mean-field theory does not really distinguish between finite and infinite systems [21], and can predict magnetic order even in the case of small lattices, as we will see. There is both a negative and a positive side to this. The bad side is that it predicts magnetic phase transitions in 1D and 2D, when we know that they do not occur. The good side is that the magnetic phases predicted in higher dimensions are quite accurate. Alternatively, we can say that phase transitions occur for a certain finite system with N degrees of freedom and free energy F_N if and only if F_∞ has a singularity [22]. This definition conveniently allows us to rely on results for infinite cases to give us information on finite ones.

Mean-field numerical studies of the Hubbard model in a square lattice date back many decades. First, when using mean-field theory to obtain the magnetic phase diagram of the Hubbard model in a square lattice, one would compare the free energy of three possible magnetic states of the lattice: paramagnetic, ferromagnetic and antiferromagnetic [14, 18, 23–25]. This consideration would then yield a phase diagram, which consisted of a map showing, on each point (n, U), which magnetic phase has the lowest free energy (n is the ratio between number of electrons and number of sites). Later, spiral phases were also included (a generalization of the traditional phases), increasing the complexity of the phase diagram [26, 27]. More recently, the possibility of spatial phase separation was also considered [16, 28, 29], i.e., regions of the phase diagram where several traditional magnetic phases are degenerate, and consequently coexist in the lattice.

All the aforementioned progress still imposes two very important restrictions: that the magnetization, m, and electronic density, n, are the same on every site of the lattice. One consequence of this is that the usual mean-field calculations can consist simply of finding the mean-field free energy, and then minimizing it with respect to the magnetization [27]. If, contrariwise, one wishes to find out if the ground state of the system has a uniform particle density, one cannot simply minimize the mean-field free energy with respect to n. In fact, to overcome these restrictions, a generalized Hartree-Fock theory was derived by Bach and collaborators [30]. One of the main points of the derivation is that, while the mean-field free energy, F_{HF}, is the free-energy of a system modeled by the mean-field Hamiltonian, the minimum of the exact free-energy, F, is not found by minimizing the mean-field free energy with respect to the mean-field parameters m and n, but instead by finding one of its saddle points,

$$\min_{n,m}(F) = \min_{m} \max_{n}(F_{\mathrm{HF}}). \tag{1.1}$$

This often passes unnoticed by researchers because, when forcing n to be the same in the whole system, this expression reduces to a minimization problem in F_{HF}. The derivation of the generalized Hartree-Fock theory was later extended away from half-filling [31]. Alternative approaches can be found in Refs. [32], [33] and [34]. Curiously, some authors present the generalized Hartree-Fock results for the sake of completeness, but do not apply them to their mean-field analysis. This means that space modulation of the parameters m and n has not yet been studied in detail. For instance, in Ref. [28], although it is emphasized that finding a saddle point of F_{HF} corresponds to minimizing the grand-canonical free energy (that is, finding the minimum of the grand-canonical free energy corresponding to a many-body state of independent fermions), the electronic density in this Reference is assumed to be the same on all lattice sites.

In Chapter 3 of this thesis, we further extend the study of the phase diagram of the Hubbard model on a square lattice, by allowing the mean-field parameters to vary along the lattice. To be more specific, we divide the square lattice into two sublattices, and allow each sublattice to have its own value of m. On a side note, we also allowed the system to modulate n, but found that both sublattices had the same ground-state n (an expected outcome, due to the symmetry of the square lattice), and consequently did not include this result in the published paper.

Variations of the square lattice

Variations of the square lattice may exhibit interesting phenomena. In this work, we study two ways to obtain variations of the square lattice: twisting its boundaries and inserting additional sites and longer-range hoppings. Despite the limited number of lattices presented here, some of our results also apply to other geometries.

In Chapter 4, we introduce the Hubbard model in a helicoidal lattice, which strongly resembles the square lattice, except for the boundary conditions. In practice, our study of this lattice in the strong-coupling limit is done first by considering only hoppings along the helix ($t_{||}$), i.e., as if the helix was simply a linear chain of atoms, and then introducing hoppings across helix steps ($t_{\perp}$) as a perturbation. In this perspective, the helix acts as a bridge between the 1D and 2D models.

The existence of chemical compounds with helical geometry, such as DNA, has long served as motivation for the study of electronic behavior in helicoidal lattices, both with and without Coulomb-like interactions [35–37]. One of the first studies of the Hubbard model in a helicoidal lattice considered a 1D chain of atoms with both nearest- and third-nearest-neighbor hoppings [38]. The study consisted on Bethe ansatz calculations, and first-order phase transitions were found in this system, caused by the competition between the usual 1D nearest-neighbor hoppings and the newly-introduced third-nearest-neighbor hoppings. Later, the model was generalized to nearest- and arbitrarily-nearest-neighbor hoppings [39]. This generalization included a Bethe ansatz analysis of a helix with infinite diameter in order to recover some of the properties of the 2D Hubbard model. More recently, the helicoidal geometry was studied using the discrete nonlinear Schroedinger equation, rather than the Hubbard model [40]. That study was partly motivated by the recently-proposed experimental implementation of helix-shaped trapping potential for cold atoms [41], which could also be used to test the results we present in Chapter 4. Our study of the Hubbard model on a helix is motivated by the common belief that spin dynamics in the strong-coupling limit is only a consequence of the Heisenberg (J) correction. Here, we show that, even for infinite U (where the J correction is zero), interesting spin dynamics arises due to the introduction of the $t_{\perp}$

term of the Hamiltonian.

In Chapters 5-8, we study the Hubbard model in decorated square lattices, mainly focusing on those of Lieb's class. Decorated lattices are obtained by adding extra sites or hoppings longer-range hopping terms to trivial lattices, such as the square lattice. The most well-known decorated square lattices are the Lieb [42], Mielke [43] and Tasaki [44] lattices, in increasing order of complexity (Fig. 1.1). The Lieb lattice has three atoms per unit cell, and can be obtained from the square lattice by removing a third of its atoms (or by inserting an extra atom between every pair of nearest neighbors). The Mielke lattice can be obtained from the square lattice by adding next-nearest-neighbor hoppings at every other square, and the Tasaki lattice is obtained from the square lattice by inserting an atom at the center of each square, as well as next-nearest-neighbor hoppings for the original atoms.

Flat-band systems

The presence of a flat band in the energy spectrum in the absence of an external magnetic field is a common feature in the Lieb, Mielke and Tasaki lattices. The Lieb lattice stands out from the other two, however, as the flat band of the former intercalates the itinerant bands [45], shaped like Dirac cones with symmetric energies [46], and arises simply due to its topology, while that of the latter results from the relation between the nearest-neighbor and more-distant-neighbor hopping parameters and has an energy lower than that of the itinerant bands. The eigenstates of the tight-binding Hamiltonian whose energies lie in the flat band are mostly localized states, i.e., they do not "see" the boundaries of the lattice and remain eigenstates if more unit cells are added to the system. In their most compact form, the localized states have non-zero probability density only on a small region of the lattice, and are trapped in that region unless a magnetic field is applied. In Chapter 5, the compact forms of the zero-flux localized states of the Lieb, Mielke and Tasaki lattices are shown. We also develop a set of rules that allow one to find a localized state of a lattice knowing a localized state of a different lattice, both in the zero- and infinite-U limits, with one electron and one hole, respectively.

Due to the Hubbard U and a generalized Hund's rule, one finds ferromagnetism at half-filling of the flat band [42, 47, 48]. This metallic (flat-band) ferromagnetism has motivated the experimental study of decorated 2D lattices and the search for crystal structures which display the geometry of the decorated lattices. However, obstacles such as the lifting of the degeneracy of the flat band by the Jahn-Teller effect [49] (lattices with a degenerate eigenstate may undergo a geometrical distortion which lifts this degeneracy, if that would lower its energy) or the difficulty in controlling the filling of the lattice (so as to ensure we are working in the flat-band region of the spectrum) hinder this research and call for different approaches. Alternative experimental realizations of flat-band systems include quantum dot arrays [50], arrays of optical waveguides [51, 52], exciton-polariton condensates [53, 54], and cold atoms in optical lattices [55, 56].

Time-dependent perturbations

Another important remark is that the Lieb lattice retains its flat band in the presence of an external magnetic field, whereas the flat band of the Mielke and Tasaki lattices becomes dispersive. In all three cases, the plots of energy values vs magnetic field display fractal Hofstadter butterflies [57]. The adiabatic theorem [58], by Born and Fock, states the following:

A physical system remains in its instantaneous eigenstate if a given perturbation is

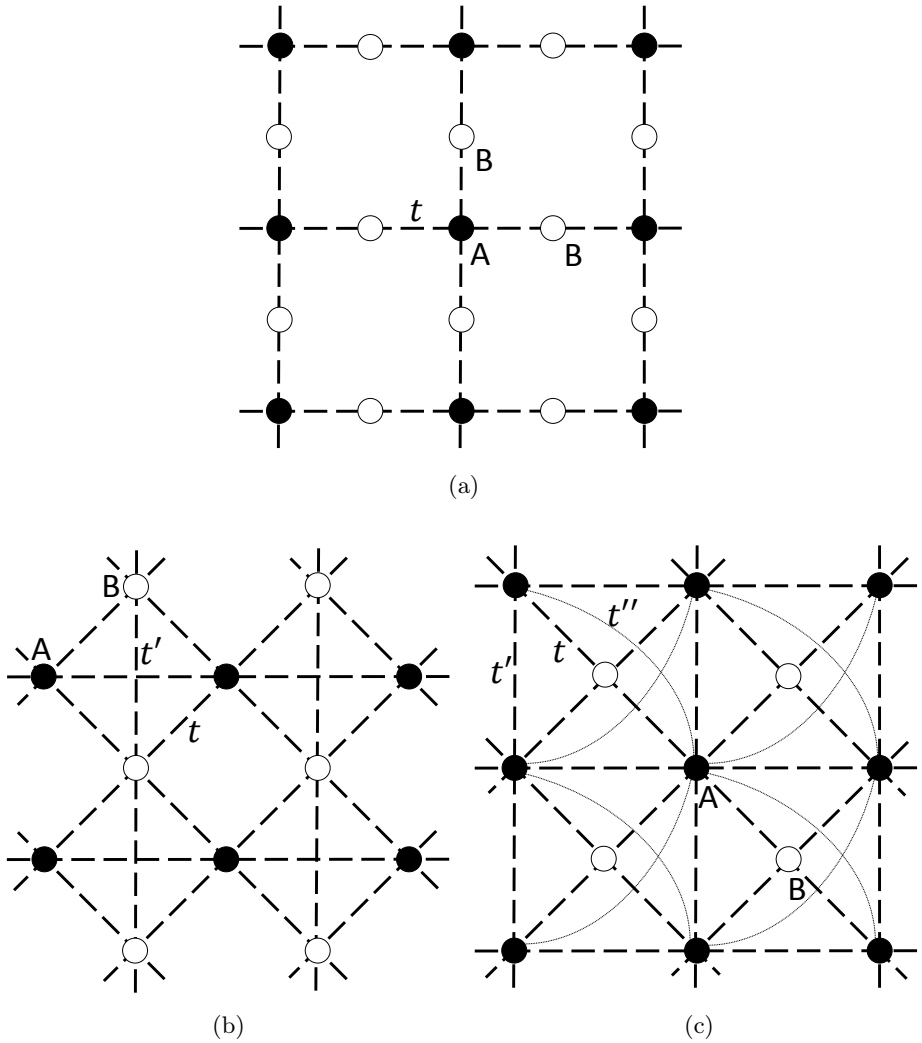

Figure 1.1: Three examples of decorated lattices: the Lieb (a), Mielke (b) and Tasaki (c) lattices. The lines connect sites between which the hopping term is finite. The tight-binding dispersion relation of the Lieb lattice includes a flat band due to its geometry. For the other two lattices to display a flat band in their energy spectrum, the relation $t = t' = 2t''$ is required. The relative thickness of the lines within each lattice reflects this relation, corresponding to the situation in which a flat band is present.

acting on it slowly enough and if there is a gap between the eigenvalue and the rest of the Hamiltonian's spectrum.

If a quantum-mechanical system is initially ($t = 0$) in a state $\psi(x, 0)$, which is an eigenstate of the initial Hamiltonian, $H(0)$ and a time-dependent perturbation is applied and causes the Hamiltonian to change over time, becoming $H(t)$, the eigenstate evolves according to the time-dependent Schroedinger equation,

$$i\hbar\frac{\partial}{\partial t}\psi(x,t) = H(t)\psi(x,t), \tag{1.2}$$

imposing the condition that at $t = 0$ the system is in state $\psi(x, 0)$. The adiabatic theorem states that the state of the system at a certain later time $t_1 > 0$ strongly depends on how much time has passed since we began introducing the perturbation (in this case, that is t_1). On the one hand, if $t_1 \to \infty$, the process is perfectly adiabatic and the evolved state of the system, $\psi(x, t_1)$, is now an eigenstate of the new Hamiltonian, $H(t_1)$. Generally, this means that the spatial probability densities encoded in $\psi(x, 0)$ have changed, and therefore $|\psi(x_i, t_1)|^2 \neq |\psi(x_i, 0)|^2$, for each point of space x_i. On the other hand, if the perturbation acts suddenly, the Hamiltonian changes almost instantly from $H(0)$ to $H(t_1)$, corresponding to the limit $t_1 \to 0$. In this case, the system does not have enough time to adapt its configuration, and the spatial probability distribution remains the same ($|\psi(x_i, t_1)|^2 = |\psi(x_i, 0)|^2$). If the distribution is the same but the Hamiltonian changed, it stands to reason that the evolved state of the system is typically no longer an eigenstate of the Hamiltonian, but instead a linear combination of eigenstates whose probability densities amount to the initial one [59].

In Chapter 6, we verify Born's adiabatic theorem for the case of localized states in the Lieb lattice and describe their evolution in more detail by presenting a simple toy model such that the evolution of one of its eigenstates mimics that of the localized states in the Lieb lattice. We emphasize that the Lieb lattice is not the only decorated lattice to display a flat band in the presence of a magnetic field. In fact, the AB_2 chain [60] shares this property, and additionally also has three atoms per unit cell, and is also bipartite. Although the results are not explicitly shown here, they are essentially the same as those obtained for the Lieb lattice.

There have recently been many works that address the time-evolution of non-interacting eigenstates of lattice Hamiltonians in the context of topological insulators [55, 61, 62]. Such works focus on the Berry phases acquired by the states under periodic perturbations. In our work, we take a different point of view and study the localized component of an evolving state, going beyond the adiabatic regime.

Bipartite lattices

A lattice is said to be bipartite if it can be divided into two sublattices, A and B, such that every electron hopping connects atoms of different sublattices. Two of the most important and general theorems on bipartite lattices are the uniform density theorem [63] and Lieb's theorem [42]. These theorems are described in more detail in the next chapter, and roughly state that, for the Hubbard model in bipartite lattices at half-filling, the electronic density on each site is unitary, and the total spin on each unit cell is given by $\frac{1}{2}|N_B - N_A|$, where N_B and N_A are the number of B sites and A sites in a unit cell, respectively. Both results are independent of the Hubbard U.

In the case of a bipartite square lattice, the theorems simply imply that the charge density is the same on every site, and that the total spin per unit cell is zero. As mean-field calculations

often assume uniform charge and spin density, the application of the mean-field approximation to the square lattice naturally agrees with what the theorems state, even when it yields a wrong on-site magnetization.

On decorated lattices, this is not as simple. For example, the Lieb lattice has three atoms per unit cell: two of one sublattice, say B, and one of the other sublattice, say A. Whatever the choice of site labeling, the number of sites of each type is different, and therefore the total spin on a unit cell is $1/2$. In Chapter 7, we show that only a mean-field study that allows modulation of spin density can produce this result. Such is the use of the generalized Hartree-Fock theory. We begin by building the mean-field magnetic phase diagram of the Lieb lattice, as none existed in the literature, by using the usual mean-field approach, i.e. assume fixed charge and spin densities in the whole lattice. That assumption guarantees that the uniform density theorem is satisfied, but fails to agree with Lieb's theorem at low U. We then redo our numerical calculations, allowing the system to modulate both its charge and spin density (Chapter 8) and successfully obtain the results predicted by both theorems, namely we obtain a ferrimagnetic phase at half-filling, with a total spin independent of U. Although we allow the system to modulate its electronic density, the numerical mean-field calculation correctly predicts a uniform density at half-filling. Away from half-filling, the relative occupation of the sublattices is a known result from the literature [64], and our mean-field calculations correctly reproduce it as well, both for small and large U.

Organization of the thesis

This thesis contains slightly modified versions of published or submitted peer-reviewed papers from Science Citation Index (SCI) journals (Chapter 3 and Chapters 5-8). The most obvious modification is the format. For instance, depending on the journal on which the papers were published or to which they were submitted, the two-collumn format was changed to one-collumn, and the font size was decreased or increased to become the same throughout the whole thesis. The size of some figures was increased (in some of the original papers, we were forced to reduce the size of some figures in order to fit within the page limit). The position of some figures may have been changed automatically by LaTeX. No information was added or removed. The order chosen for the chapters is not the chronological order in which the papers were published. Instead, they are presented in an order which confers more cohesion to this thesis: we study the Hubbard model on a square lattice, and then on variations of the square lattice, beginning with the helicoidal lattice and going on to decorated square lattices.

In **Chapter 2**, we review some known results on the Hubbard model. We briefly discuss the basics of the Hubbard model by studying it in the limiting cases $t = 0$ and $U = 0$. We then review two important theorems on the Hubbard model: Lieb's theorem and the uniform density theorem, which deal with the total spin and occupation of bipartite lattices at half-filling, respectively. In the last section of this chapter, we briefly discuss the Hubbard model in a ring, in the $U \to \infty$ limit, whose solution coincides with that of the same model in a helicoidal lattice, when transversal hopping is neglected.

Chapter 3 addresses the Hubbard model in a square lattice. We use the mean-field approximation to deal with the interaction term and extend the results of the literature on the mean-field magnetic phase diagram of the Hubbard model in a square lattice. Whereas in the literature the lattice is assumed to display the same magnetization (m) at every site, here we divide the square lattice into two sublattices (1 and 2) and allow (not force) each of them to

have a different magnetization (m_1 and m_2). We then find that, by allowing that modulation, the states with $m_1 \neq m_2$ are in fact more stable (have lower energy) than states with uniform magnetization in some regions of the phase diagram. This Chapter is an adaptation of

> J. D. Gouveia and R. G. Dias, *Spiral ferrimagnetic phases in the two-dimensional Hubbard model*. Solid State Communications, Volume 185, May 2014, Pages 21-24
>
> DOI: 10.1016/j.ssc.2014.01.004

Chapter 4 presents the quantum spin queue model (QSQM), introduced as a tool to tackle the Hubbard model on a helix allowing hops in both longitudinal and transversal directions in the strong-coupling limit ($U \to \infty$) with one empty site (called the hole). If all spins are aligned (the ferromagnetic configuration), the problem is reduced to a spinless tight-binding problem for the hole. We solve the model with one inverted spin analytically to study the effect of $t_\perp$ on the spin configuration. The eigenvalues of the QSQM Hamiltonian are also shown for several inverted spins.

Chapter 5 introduces decorated lattices. We present a set of rules which allow one to obtain localized states of a decorated lattice, starting from a localized state on a different lattice. The rules include any subjacent changes to the hopping parameters or the energy of the state, and can be applied to both the tight-binding and the strong-coupling limits, yielding particle or hole localized states respectively. As an example, we show how the rules can be applied to obtain a localized state of the Tasaki lattice, starting from one of the Lieb lattice. This Chapter is an adaptation of

> R. G. Dias and J. D. Gouveia, *Origami rules for the construction of localized eigenstates of the Hubbard model in decorated lattices*. Scientific Reports 5, Article number: 16852 (2015)
>
> DOI: 10.1038/srep16852

Chapter 6 is focused on the time evolution of localized states in decorated lattices, due to the slow introduction of a magnetic field perpendicular to the lattice. In the Lieb lattice, as the magnetic flux increases slowly and linearly with time, the positive- and negative-energy bands periodically touch the flat band. This causes a localized state of the Lieb lattice with no flux to change its localized component over time, in a step-like pattern. We conceive a toy model with only three states, one of which has zero energy (the same energy of the flat band of the Lieb lattice). The energy of the other toy states periodically crosses the zero-energy line, to mimic the behavior of the Lieb lattice. We then compare the evolution of localized states of the Lieb lattice with that of the zero-energy state of the toy model. This Chapter is an adaptation of

> J. D. Gouveia, I. A. Maceira and R. G. Dias, *Time evolution of localized states in Lieb lattices*. arXiv:1607.04326 [quant-ph] (2016)

Chapter 7 comprehends magnetism in the Lieb lattice. We use the mean-field approximation to build the Hubbard interaction vs electronic density magnetic phase diagram of the Lieb lattice. Far from half-filling, the diagram was found to be similar to that of the square lattice, but at half-filling the ground state of the Lieb lattice is ferrimagnetic, rather than antiferromagnetic. This can be justified with Lieb's theorem [42], and happens because the unit cell of the Lieb lattice has a different number of atoms of each type. This Chapter is an adaptation of

J. D. Gouveia and R. G. Dias, *Magnetic phase diagram of the Hubbard model in the Lieb lattice.* Journal of Magnetism and Magnetic Materials, Volume 382, 15 May 2015, Pages 312-317

DOI: 10.1016/j.jmmm.2015.02.005

In **Chapter 8**, we extend the mean-field study of the Lieb lattice by allowing each sublattice to have a different magnetization (m) and electronic density (n). For that, we use the generalized Hartree-Fock theory. This theory has existed for tens of years but it had never been applied, as authors often consider the aforementioned mean-field parameters to be uniform in the whole lattice. We show that, by employing this more complex mean-field approach, the mean-field results coincide with those predicted by both Lieb's theorem and the uniform density theorem. This Chapter is an adaptation of

J. D. Gouveia and R. G. Dias, *Spin and charge density waves in the Lieb lattice.* Journal of Magnetism and Magnetic Materials, Volume 405, 1 May 2016, Pages 292-303

DOI: 10.1016/j.jmmm.2015.12.096

Finally, a summary of the conclusions of all chapters is presented.

References

[1] M. Jammer. *The Philosophy of Quantum Mechanics*. Wiley, 1974.

[2] A. Pais. "Einstein and the quantum theory". *Rev. Mod. Phys.* 51 (1979), pp. 863–914.

[3] F. H. L. Essler et al. *The One-Dimensional Hubbard Model*. Cambridge Press, 2005.

[4] H. Bethe. "Zur Theorie der Metalle". *Zeitschrift für Physik* 71 (1931), pp. 205–226.

[5] M. K. Wu et al. "Superconductivity at 93 K in a new mixed-phase Y-Ba-Cu-O compound system at ambient pressure". *Phys. Rev. Lett.* 58 (1987), pp. 908–910.

[6] E. H. Lieb and F. Y. Wu. "Absence of Mott Transition in an Exact Solution of the Short-Range, One-Band Model in One Dimension". *Phys. Rev. Lett.* 20.25 (1968), pp. 1445–1448.

[7] S. Takada. "Long-Range Order in Ground States and Collective Modes in One- and Two-Dimensional Models". *Progress of Theoretical Physics* 54.4 (1975), p. 1039.

[8] K. Kubo and M. Uchinami. "The Antiferromagnetic Ground State of a Half-Filled Hubbard Model". *Progress of Theoretical Physics* 54.5 (1975), p. 1289.

[9] R. G. Dias and J. M. B. Lopes dos Santos. "Simple representation of the eigenstates of the $U \to \infty$ one-dimensional Hubbard model". *Journal de Physique I* 2 (1992), pp. 1889–1897.

[10] Y. Nagaoka. "Ferromagnetism in a Narrow, Almost Half-Filled s Band". *Physical Review* 147 (1966), pp. 392–405.

[11] J. Kanamori. "Electron Correlation and Ferromagnetism of Transition Metals". *Progress of Theoretical Physics* 30.3 (1963), p. 275.

[12] Y. M. Vilk, L. Chen, and A.-M. S. Tremblay. "Theory of spin and charge fluctuations in the Hubbard model". *Phys. Rev. B* 49 (1994), pp. 13267–13270.

[13] M. P. Marder. *Condensed Matter Physics*. John Wiley and Sons, 2000.

[14] J. Dorantes-Dávila, J. L. Morán-López, and M. Avignon. "Ground-state solutions of the Hubbard model". *Phys. Rev. B* 27 (1983), pp. 575–577.

[15] S. Sarker et al. "Spiral states in the square-lattice Hubbard model". *Physical Review B* 43 (1991), pp. 8775–8778.

[16] W. Schumacher. "On incommensurate phases in the magnetic phase diagram of the hubbard model". *physica status solidi (b)* 119.1 (1983), pp. 235–238.

[17] E. Kaxiras and E. Manousakis. "Ground state of the strong-coupling Hubbard Hamiltonian: A numerical diagonalization study". *Phys. Rev. B* 37 (1988), pp. 656–659.

[18] S. N. Coppersmith and C. C. Yu. "Phase diagram of the Hubbard model: A variational wave-function approach". *Phys. Rev. B* 39 (1989), pp. 11464–11474.

[19] A. Richter, G. Röpke, and F. Goedsche. "Functional Integral Approach for the Hubbard Model with Arbitrary Electron Density". *physica status solidi (b)* 88.1 (1978), pp. 189–198.

[20] N. D. Mermin and H. Wagner. "Absence of Ferromagnetism or Antiferromagnetism in One- or Two-Dimensional Isotropic Heisenberg Models". *Physical Review Letters* 17.22 (1966), pp. 1133–1136.

[21] P. Fazekas. *Lecture Notes on Electron Correlation and Magnetism*. Series in Modern Condensed Matter Physics. World Scientific, 1999.

[22] P. Mainwood. *Phase Transitions in Finite Systems*. 2005.

[23] D. R. Penn. "Stability Theory of the Magnetic Phases for a Simple Model of the Transition Metals". *Phys. Rev.* 142 (1966), pp. 350–365.

[24] E. Kaxiras and E. Manousakis. "Ground state of the strong-coupling Hubbard Hamiltonian: A numerical diagonalization study". *Phys. Rev. B* 37 (1988), pp. 656–659.

[25] A. Richter, G. Röpke, and F. Goedsche. "Functional Integral Approach for the Hubbard Model with Arbitrary Electron Density". *Physica Status Solidi B Basic Research* 88 (1978), pp. 189–198.

[26] S. Sarker et al. "Spiral states in the square-lattice Hubbard model". *Phys. Rev. B* 43 (1991), pp. 8775–8778.

[27] M. Dzierzawa. "Hartree-Fock theory of spiral magnetic order in the 2-d Hubbard model". *Z. Phys. B* 86 (1992), pp. 49–52.

[28] E. Langmann and M. Wallin. "Mean Field Magnetic Phase Diagrams for the Two Dimensional $t - t' - U$ Hubbard Model". *Journal of Statistical Physics* 127 (2007), pp. 825–840.

[29] P. A. Igoshev et al. "Incommensurate magnetic order and phase separation in the two-dimensional Hubbard model with nearest- and next-nearest-neighbor hopping". *Phys. Rev. B* 81 (2010), p. 094407.

[30] V. Bach, E. H. Lieb, and J. P. Solovej. "Generalized Hartree-Fock theory and the Hubbard model". *Journal of Statistical Physics* 76 (1994), pp. 3–89.

[31] V. Bach and J. Poelchau. "Hartree-Fock Gibbs states for the Hubbard model". *Markov Processes and Rel Fields* 2(1) (1996), pp. 225–240.

[32] E. Langmann and M. Wallin. "Restricted path integral approach to the doped Hubbard model". *Europhysics Letters* 37 (3) (1997), pp. 219–224.

[33] E. Langmann and M. Wallin. "Mean-field approach to antiferromagnetic domains in the doped Hubbard model". *Physical Review B* 55 (1997), pp. 9439–9451.

[34] J. de Woul. "A restricted Hartree-Fock study of the 2D Hubbard model". MA thesis. Royal Institute of Technology, 2007.

[35] M. Peyrard and A. R. Bishop. "Statistical mechanics of a nonlinear model for DNA denaturation". *Phys. Rev. Lett.* 62 (1989), pp. 2755–2758.

[36] G. Gaeta. "On a model of DNA torsion dynamics". *Physics Letters A* 143.4 (1990), pp. 227–232.

[37] T. Dauxois. "Dynamics of breather modes in a nonlinear "helicoidal" model of DNA". *Physics Letters A* 159.8 (1991), pp. 390–395.

[38] W. Wang and S. Xiong. "Possible first order phase transition in the one-dimensional helical Hubbard model". *Physics Letters A* 156.7 (1991), pp. 415–418.

[39] S.-J. Xiong. "Bethe ansatz study of 1+1 dimensional Hubbard model". *ZEITSCHRIFT FUR PHYSIK B CONDENSED MATTER* Volume 89, Number 1 (1992), pp. 29–34.

[40] J. Stockhofe and P. Schmelcher. "Modulational instability and localized breather modes in the discrete nonlinear Schroedinger equation with helicoidal hopping". *Physica D: Nonlinear Phenomena* 328-329 (2016), pp. 9–20.

[41] D. Reitz and A. Rauschenbeutel. "Nanofiber-based double-helix dipole trap for cold neutral atoms". *Optics Communications* 285.23 (2012). Special Issue: Optical micro/nanofibers: Challenges and Opportunities, pp. 4705–4708.

[42] E. H. Lieb. "Two Theorems on the Hubbard model". *Physical Review Letters* 62 (1989), pp. 1201–1204.

[43] A. Mielke. "Exact ground states for the Hubbard model on the Kagome lattice". *Journal of Physics A* 25 (1992), p. 4335.

[44] H. Tasaki. "Ferromagnetism in the Hubbard Models with Degenerate Single-Electron Ground States". *Physical Review Letters* 69 (1992), pp. 1608–1612.

[45] M. Nita, B. Ostahie, and A. Aldea. "Spectral and transport properties of the two-dimensional Lieb lattice". *Physical* 87 (2013), p. 125428.

[46] P. R. Wallace. "The Band Theory of Graphite". *Physical Review* 71 (1947), pp. 622–634.

[47] J. Frohlich and D. Ueltschi. "Hund's Rule and Metallic Ferromagnetism". English. *Journal of Statistical Physics* 118.5-6 (2005), pp. 973–978.

[48] A. Mielke and H. Tasaki. "Ferromagnetism in the Hubbard model". *Communications in Mathematical Physics* 158.2 (1993), pp. 341–371.

[49] H. A. Jahn and E. Teller. "Stability of Polyatomic Molecules in Degenerate Electronic States. I. Orbital Degeneracy". *Proceedings of the Royal Society of London A: Mathematical, Physical and Engineering Sciences* 161.905 (1937), pp. 220–235.

[50] H. Tamura, K. Shiraishi, and H. Takayanagi. "Ferromagnetism in Semiconductor Dot Array". *Jpn. J. Appl. Phys.* 39 (2000), p. L241.

[51] S. Mukherjee et al. "Observation of a Localized Flat-Band State in a Photonic Lieb Lattice". *Phys. Rev. Lett.* 114 (2015), p. 245504.

[52] R. A. Vicencio et al. "Observation of Localized States in Lieb Photonic Lattices". *Phys. Rev. Lett.* 114 (2015), p. 245503.

[53] F. Baboux et al. "Bosonic Condensation and Disorder-Induced Localization in a Flat Band". *Phys. Rev. Lett.* 116 (2016), p. 066402.

[54] N. Masumoto et al. "Exciton-polariton condensates with flat bands in a two-dimensional kagome lattice". *New Journal of Physics* 14.6 (2012), p. 065002.

[55] N. Goldman, D. F. Urban, and D. Bercioux. "Topological phases for fermionic cold atoms on the Lieb lattice". *Phys. Rev. A* 83 (2011), p. 063601.

[56] S. Taie et al. "Coherent driving and freezing of bosonic matter wave in an optical Lieb lattice". *Science Advances* 1.10 (2015).

[57] H. Aoki, M. Ando, and H. Matsumura. "Hofstadter butterflies for flat bands". *Phys. Rev. B* 54.24 (1996), R17296–R17299.

[58] M. Born and V. Fock. "Beweis des Adiabatensatzes". *Zeitschrift fur Physik* 51.3 (1928), pp. 165–180.

[59] T. Kato. "On the Adiabatic Theorem of Quantum Mechanics". *Journal of the Physical Society of Japan* 5.6 (1950), pp. 435–439.

[60] A. A. Lopes and R. G. Dias. "Interacting spinless fermions in a diamond chain". *Phys. Rev. B* 84 (2011), p. 085124.

[61] E. J. Bergholtz and Z. Liu. "Topological flat band models and fractional Chern insulators". *International Journal of Modern Physics B* 27.24 (2013), p. 1330017.

[62] S. A. Parameswaran, R. Roy, and S. L. Sondhi. "Fractional quantum Hall physics in topological flat bands". *Comptes Rendus Physique* 14.9 (2013), pp. 816–839.

[63] E. H. Lieb, M. Loss, and R. J. McCann. "Uniform density theorem for the Hubbard model". *Journal of Mathematica Physics* 34 (1993), pp. 891–898.

[64] H. Wang, S.-L. Yu, and J.-X. Li. "Spin fluctuations and unconventional pairing on the Lieb lattice". *Physics Letters A* 378.45 (2014), pp. 3360–3365.

Chapter 2

Known results on the Hubbard model

In this chapter, we briefly review the mathematical formulation of the Hubbard model and present some known results. Most importantly, we review the tight-binding limit of the Hubbard model, Lieb's theorem and the uniform density theorem, and the Hubbard model on a ring in the limit of strong coupling. For the latter, we present a new way to count how many eigenstates have a given momentum and use that result to study some thermodynamic functions.

2.1 The basics of the Hubbard model

The Hubbard model was independently introduced by John Hubbard, Gutzwiller and Kanamori [1] around the same time in order to model electronic correlations in narrow energy bands. In one dimension (1D), it describes the dynamics of organic conductors, while its two-dimensional (2D) version can be applied to high temperature superconductivity [2]. Hans Bethe [3] found the exact solution of the 1D Hubbard Model (wave functions of Bethe ansatz), while the solution for higher dimensionality is not known [4].

In this model, a solid consists of ions and electrons in a crystalline structure. Due to the high ratio between nuclear and electronic masses, the general form of the Hubbard Hamiltonian assumes the Born-Oppenheimer approximation, i.e., it considers a solid consisting of nuclei forming a static lattice and electrons which can hop between different atoms of the lattice.

The Hubbard Hamiltonian is the simplest model of correlated fermions, and has only two parameters. The first is the tight-binding parameter, the hopping amplitude t, describing the motion of electrons in the lattice (usually determined accurately using density-functional theory). The hopping of electrons is often assumed to occur only between nearest neighbors. In the extreme case $t \to 0$, electrons cannot hop between sites, and the model describes an isolated atomic system. In addition, the number t is assumed to be real, except in the presence of a magnetic field. In the latter case, if the magnetic field $\vec{B}$ is constant in time or varies very slowly, one simply needs to replace the hopping parameter,

$$t \to t_{ij} e^{i\frac{e}{\hbar}\int_i^j \vec{A}\cdot \mathrm{d}\vec{l}}, \tag{2.1}$$

where $\vec{A}$ is the magnetic vector potential ($\vec{B} = \vec{\nabla} \times \vec{A}$). This is called the Peierls substitution, a way to include the effect of a slowly changing magnetic field in a tight-binding model that is extremely convenient and trivial from the computational point of view. Note that, even if

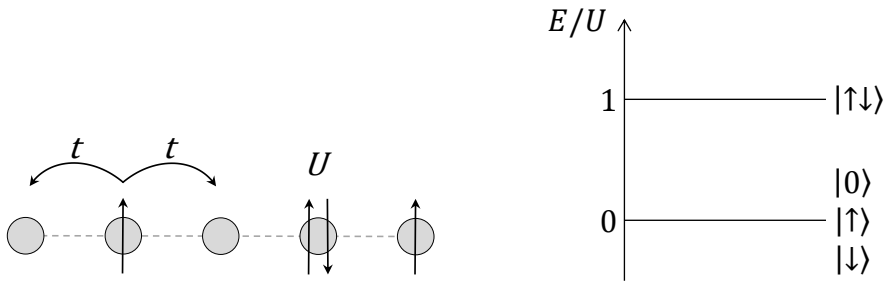

(a) (b)

Figure 2.1: (a) The two terms of the 1D Hubbard Hamiltonian: the kinetic term with amplitude t and on-site electronic interaction U. (b) Energy levels and states of the one-site Hubbard model.

t was constant throughout the lattice before, the introduction of the magnetic field implies that t now depends on the origin (i) and destination (j) sites of the hopping in question. The fact that $\vec{A}$ changes implies the emergence of an electric field, however small, equal to the time-derivative of $\vec{A}$. Nonetheless, if the rate at which the magnetic field changes is slow enough, then the evolution of the quantum state of the system (due to the change of $\vec{B}$) will be the same regardless of the chosen gauge for $\vec{A}$ [1].

The second is an on-site interaction amplitude U, which describes the interaction between electrons. This parameter is a measure of the Coulomb interaction, assumed to be screened and finite only between electrons at the same lattice site, which is the shortest range possible. The parameter U is often harder to estimate, and instead obtained by comparing theoretical predictions with experimental results. Although one cannot directly control the Coulomb interaction between a pair of electrons on the same atom, one can (in practice, equivalently) change the ratio U/t, for example by applying pressure on the solid. Normally, one is interested in a regime in which electrons are strongly correlated, i.e. in which U is larger than t. Fig. 2.1a is an illustration of these two parameters.

Even though the Hubbard model is clearly an oversimplification, it is still able to exhibit a lot of interesting phenomena that can be observed in nature, such as all types of magnetic ordering, metal-insulator transitions, superconductivity, Tomonaga-Luttinger liquids in one dimension, and Pomeranchuk instabilities[5].

The Hamiltonian of the Hubbard Hamiltonian is

$$H = -t \sum_{\langle j,j' \rangle,\sigma} \left(c^{\dagger}_{j,\sigma} c_{j',\sigma} + c^{\dagger}_{j',\sigma} c_{j,\sigma} \right) + U \sum_{j} n_{j\uparrow} n_{j\downarrow}, \tag{2.2}$$

where $\langle j, j' \rangle$ denotes nearest-neighbor pairs of sites, $c^{\dagger}_{j,\sigma}$ and $c_{j,\sigma}$ are the fermion creation and annihilation operators on site j with spin σ and $n_{j,\sigma} = c^{\dagger}_{j,\sigma} c_{j,\sigma}$ is the respective particle number operator. The first term of the Hamiltonian allows electrons to hop between nearest neighbor sites, and the second term simply counts the number of doubly occupied sites.

The Hubbard model displays some important symmetries, such as conservation of particle number and spin (SU(2)-symmetry). In the case of bipartite lattices (lattices which can

[1] In Chapter 6, we show that an evolving localized state of the Lieb lattice remains localized as long as the symmetry of $\vec{A}$ coincides with the point-group symmetry of the lattice.

be divided into two sublattices, A and B, such that all neighbors of A-atoms are B-atoms, and vice-versa), the spectrum of the tight-binding term of the Hamiltonian is symmetric with respect to the zero-energy level. This can be checked by exchanging the sign of the fermionic operators of one of the sublattices, say B, and further performing a particle-hole transformation. The sign exchange of the B operators is the reason for the requirement of the lattice being bipartite. Indeed, in the bipartite case, on every $c^\dagger_{j,\sigma}c_{j',\sigma}$ set of operators in the tight-binding term of the Hamiltonian, exactly one among j and j' belongs to sublattice B, and consequently exchanging the sign of the B operators is equivalent to exchanging the sign of t. The particle-hole transformation is done by replacing $c_j \to c^\dagger_j$ and $c^\dagger_j \to c_j$. After both operations, the tight-binding term is mapped onto itself. If one includes the interaction term when applying these transformations, the Hamiltonian of the bipartite lattice still remains unchanged at half-filling. Furthermore, on bipartite lattices at half-filling, the model has an additional SU(2) symmetry, resulting in an effective SU(2) $\times$ SU(2) = SO(4) symmetry [6]. This symmetry is crucial for some exact results which apply to bipartite lattices at half-filling, such as Lieb's theorem[7] and the uniform density theorem[8].

In the following subsections, we present some rigorous results on the Hubbard model. We begin by addressing the two most limiting cases of the Hubbard model, namely setting $t = 0$ or $U = 0$. The former is equivalent to there being one site only, while for the latter a 1D ring with periodic boundary conditions is studied. Secondly, we describe the Hubbard model with two sites and two electrons, which is useful for introducing the Heisenberg Hamiltonian. Thirdly, we introduce the strong-coupling limit ($U \to \infty$) and study a ring of atoms in this limit. Finally, we present Lieb's theorem and the uniform density theorem, which are used in later chapters of this thesis.

2.1.1 Hubbard model with $t = 0$

The grand canonical partition function is defined as the sum of $e^{-\beta(E-n\mu)}$ over all states,

$$Z = \sum_i e^{-\beta(E_i - N_i\mu)}, \tag{2.3}$$

where i labels the states, β is the inverse temperature, E_i and N_i are the energy and number of particles of state i, respectively, and μ is the chemical potential. We use the partition function to calculate the thermal expectation value of any physical quantity A,

$$\langle A\rangle = \frac{1}{Z}\sum_i A_i e^{-\beta(E_i - N_i\mu)}. \tag{2.4}$$

Most of the thermodynamic variables of a system can be expressed in terms of the partition function or its derivatives. As the temperature, T, goes to zero, $\langle A\rangle$ becomes the expectation value of the ground state. As T goes to infinity, the Boltzmann factors, $e^{-\beta(E_i - N_i\mu)} \to 1$, so that $\langle A\rangle$ becomes the classically-weighted mean of A over all possible states.

For $t = 0$, we are in the atomic limit of the Hubbard model (equivalent to having only one site). The energy values and corresponding states are shown in Fig. 2.1b. Therefore, the partition function in this case is

$$Z = 1 + 2e^{\beta\mu} + e^{-\beta U + 2\beta\mu} \tag{2.5}$$

and the average occupation of the site is

$$\langle N \rangle = \frac{2\left(e^{\beta\mu} + e^{-\beta U + 2\beta\mu}\right)}{1 + 2e^{\beta\mu} + e^{-\beta U + 2\beta\mu}}. \tag{2.6}$$

As shown in Fig. 2.2a, as T goes to 0, if the chemical potential is: i) 0^-, no particles are present; ii) $U/2$, then we have one particle; iii) U^+, the system has two particles, as no more than two particles can occupy the same orbital, reflecting the Pauli exclusion principle.

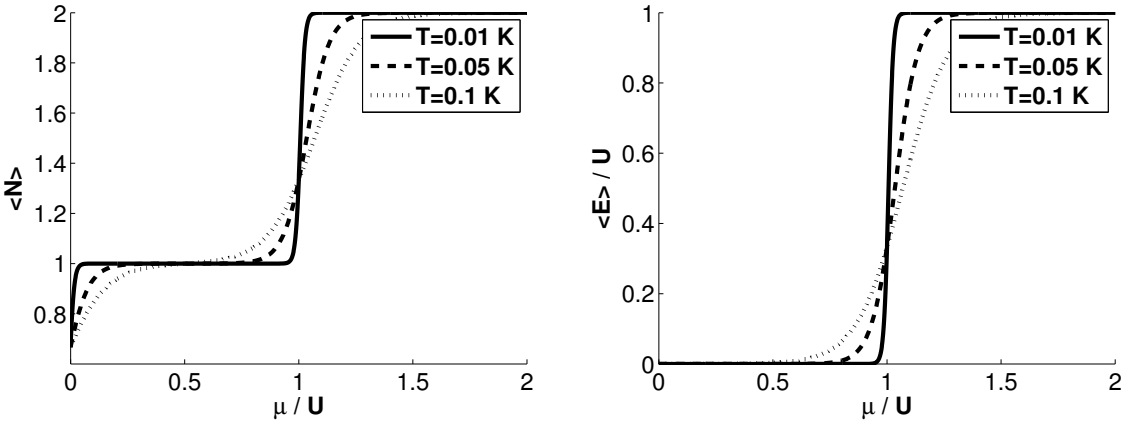

(a) Average occupation number

(b) Average energy

Figure 2.2: Average occupation number (a) and average energy (b) of the 1-site Hubbard model as a function of the chemical potential, for several temperatures.

In addition, we can calculate the average energy,

$$\langle E \rangle = U \frac{e^{-\beta(U-2\mu)}}{1 + 2e^{\beta\mu} + e^{-\beta U + 2\beta\mu}}. \tag{2.7}$$

Plots of $\langle E \rangle$ are shown in Fig. 2.2b as a function of μ for several temperatures. The on-site interaction only plays a role if more than one particle exists. In addition, the energy is zero if there is only a single particle, or no particles at all.

2.1.2 Hubbard model with $U = 0$

For $U = 0$ (the so-called tight-binding approximation), we shall consider a 1D ring with L sites and periodic boundary conditions (see Fig. 2.3). The results of this section can easily be generalized to two or three dimensions. In this case, the Hamiltonian is

$$H = -t \sum_{\langle i,j \rangle, \sigma} c^\dagger_{i,\sigma} c_{j,\sigma}, \tag{2.8}$$

with eigenstates

$$|\Psi_{k,\sigma}\rangle = \frac{1}{\sqrt{L}} \sum_{j=1}^{L} e^{ikj} c^\dagger_{j,\sigma} |0\rangle \tag{2.9}$$

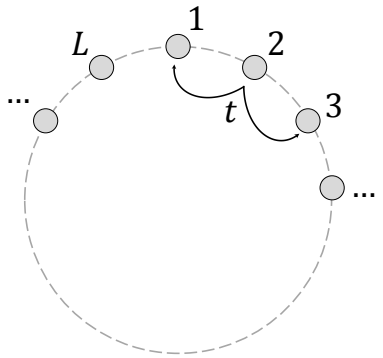

Figure 2.3: A 1D Hubbard ring with L sites, labeled from 1 to L. Within the tight-binding approximation, electrons can only hop to adjacent free sites, and there is no energy cost associated with double occupations.

and eigenvalues

$$\varepsilon_k = -2t \cos k, \tag{2.10}$$

where $k = \frac{2\pi n}{L}$ with $n = 0, 1, \cdots, L-1$, assuming a unitary lattice constant. One usually represents these energies under the more symmetric domain, $k \in [-\pi, \pi]$. In a D-dimensional square lattice, the eigenvalues of the Hamiltonian become

$$E = -2 \sum_{d=1}^{D} t_d \cos k_d, \tag{2.11}$$

where d labels the dimensions and

$$k_d = \frac{2\pi}{L_d} n_d \qquad\qquad n_d = 0, 1, ..., L_d - 1, \tag{2.12}$$

L_d being the number of sites in the d-direction.

In terms of electrical conductance, in a system with $U \gg t$, electrons cannot, at half-filling, hop between atoms and therefore one has an insulating system. On the other hand, if $U \ll t$, there is practically no interaction between the electrons and they are allowed to freely hop along the available sites (keeping in mind the Pauli exclusion principle), so one has a conductor. At intermediate values of U/t, a metal-insulator transition takes place, called the Mott transition. The phenomenon of an insulator becoming a conductor occurs only in single-valent systems and is regarded as a transition from strongly correlated ($U \gg t$) to weakly correlated ($U \ll t$) electrons.

2.1.3 The two-site Hubbard model

The 2-site Hubbard Model with open periodic boundary conditions describes an H_2 molecule. Here, however, we consider the periodic model in order to be consistent with the rest of the work[2]. The general Hubbard Hamiltonian, when applied to two sites, becomes

$$H = -2t \left(c^\dagger_{1,\downarrow} c_{2,\downarrow} + c^\dagger_{1,\uparrow} c_{2,\uparrow} + c^\dagger_{2,\downarrow} c_{1,\downarrow} + c^\dagger_{2,\uparrow} c_{1,\uparrow} \right) + U \left(n_{1\uparrow} n_{1\downarrow} + n_{2\uparrow} n_{2\downarrow} \right). \tag{2.13}$$

[2]In the case of two sites, the difference between periodic and open boundary conditions is purely mathematical. The kinetic term of the Hamiltonian in the case of open boundary conditions would be $-t(\cdots)$ instead of $-2t(\cdots)$.

Assuming each atom to be single-valent, we have two electrons. The possible states of the system are

$$\begin{aligned} |\uparrow,\downarrow\rangle &= c^\dagger_{2,\downarrow} c^\dagger_{1,\uparrow} |0\rangle\,, \\ |\downarrow,\uparrow\rangle &= c^\dagger_{2,\uparrow} c^\dagger_{1,\downarrow} |0\rangle\,, \\ |\uparrow\downarrow,\centerdot\rangle &= c^\dagger_{1,\downarrow} c^\dagger_{1,\uparrow} |0\rangle\,, \\ |\centerdot,\uparrow\downarrow\rangle &= c^\dagger_{2,\downarrow} c^\dagger_{2,\uparrow} |0\rangle\,. \end{aligned} \tag{2.14}$$

The first two states are called covalent, characterized by the sharing of the pair of electrons between the atoms, and the other two states are ionic, with oppositely charged atoms.

Considering periodic boundary conditions, the matrix representation of this Hamiltonian, in the basis of Eq. 2.14, is

$$\begin{array}{c} \begin{array}{cccc} |\uparrow,\downarrow\rangle & |\downarrow,\uparrow\rangle & |\uparrow\downarrow,\centerdot\rangle & |\centerdot,\uparrow\downarrow\rangle \end{array} \\ \begin{pmatrix} 0 & 0 & -2t & -2t \\ 0 & 0 & +2t & +2t \\ -2t & +2t & U & 0 \\ -2t & +2t & 0 & U \end{pmatrix} \end{array} \tag{2.15}$$

For $t = 0$, the Hamiltonian is automatically diagonal and its eigenvalues are 0 and U (the on-site energy for states $|\uparrow\downarrow,\centerdot\rangle$ and $|\centerdot,\uparrow\downarrow\rangle$). For $U = 0$, the eigenvalues are 0, $-4t$ and $+4t$. For all other cases, we get the following eigenvalues and eigenvectors,

$$\begin{aligned} \varepsilon_\pm = \tfrac{1}{2}\left(U \pm \sqrt{64t^2 + U^2}\right); \quad \Psi_\pm &= \frac{1}{\sqrt{2 + \frac{\varepsilon_\pm^2}{2t^2}}} \left(|\uparrow,\downarrow\rangle - |\downarrow,\uparrow\rangle - \tfrac{\varepsilon_\pm}{2t}\left(|\uparrow\downarrow,\cdot\rangle + |\cdot,\uparrow\downarrow\rangle\right)\right) \\ \varepsilon_{\text{cov}} = 0; \quad \Psi_{\text{cov}} &= \tfrac{1}{\sqrt{2}}\left(|\uparrow,\downarrow\rangle + |\downarrow,\uparrow\rangle\right) \\ \varepsilon_{\text{ion}} = U; \quad \Psi_{\text{ion}} &= \tfrac{1}{\sqrt{2}}\left(|\uparrow\downarrow,\cdot\rangle - |\cdot,\uparrow\downarrow\rangle\right), \end{aligned} \tag{2.16}$$

where the superpositions of the two covalent or the two ionic states are denoted Ψ_{cov} and Ψ_{ion}, respectively. Fig. 2.4 shows the behavior of these eigenvalues as U increases.

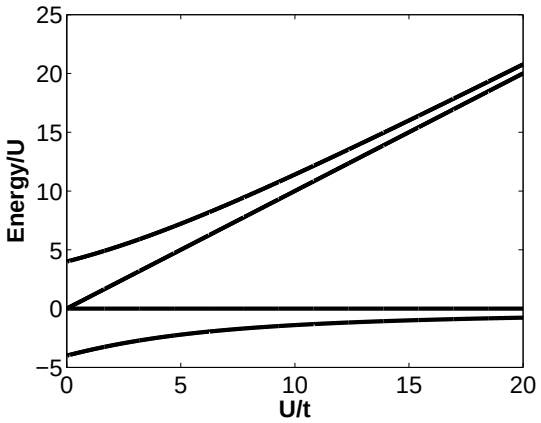

Figure 2.4: Eigenvalues of the 2-site Hubbard Hamiltonian as a function of U/t. From top to bottom, the four eigenvalues are ε_+, ε_{ion}, ε_{cov} and ε_- (see Eq. 2.16). As U goes to infinity, $\varepsilon_+ \to \varepsilon_{\text{ion}}$ and $\varepsilon_- \to \varepsilon_{\text{cov}}$. Up to first order corrections, each pair becomes coincident in this limit, and up to second order, $\varepsilon_- \approx \varepsilon_{\text{cov}} - 16\frac{t^2}{U}$.

In the $U \gg t$ limit,

$$\begin{aligned} \varepsilon_+ &= \tfrac{1}{2}\left(U + \sqrt{64t^2 + U^2}\right) \approx U = \varepsilon_{ion}, \\ \varepsilon_- &= \tfrac{1}{2}\left(U - \sqrt{64t^2 + U^2}\right) \approx -\tfrac{16t^2}{U}. \end{aligned} \tag{2.17}$$

Up to first order, Ψ_+ and Ψ_{ion} become coincident, as well as Ψ_- and Ψ_{cov}. On can write an effective Hamiltonian that correctly describes the second-order energy difference between Ψ_- and Ψ_{cov} (apart from a constant factor, which we will neglect since we are only interested in the energy difference between these two states),

$$H_{eff} = \frac{16t^2}{U}\mathbf{S}_1 \cdot \mathbf{S}_2. \tag{2.18}$$

In the many-site limit, these strong coupling energy differences are escribed by a generalized form of this Hamiltonian,

$$H_{eff} = \frac{16t^2}{U} \sum_{<i,j>} \mathbf{S}_i \cdot \mathbf{S}_j, \tag{2.19}$$

where $\langle i, j \rangle$ denotes summation between nearest neighbors. This is the Heisenberg Hamiltonian [9].

2.2 Lieb's theorem

In one of his papers of 1989 [7], Lieb presents two theorems, each about the attractive ($U < 0$) or repulsive ($U > 0$) Hubbard models. In this work, we are interested in the second theorem, which states the following:

> *Let Λ be the set of all sites of a bipartite lattice, i.e., a lattice with $|\Lambda|$ sites, which can be divided into two disjoint sets (sublattices) A and B, such that the hopping parameter t_{xy} of the Hamiltonian, H, is only finite if x and y are in different sublattices. Furthermore, let U be the positive, site-independent, on-site electronic interaction. Assume that the number of B sites, $|B|$, is greater than the number of A sites, $|A|$, and that the number of electrons equals the number of lattice sites ($N = |\Lambda|$). Under these conditions, the ground state of H has the spin*
>
> $$S_{\text{tot}} = \frac{1}{2}(|B| - |A|). \tag{2.20}$$

As an example, let us apply this theorem to the Lieb lattice (Fig. 1.1a), which is typical in copper oxides [10]. Each unit cell contains one A atom and two B atoms. If the lattice is composed of $L \times L$ unit cells, the A atoms form a square lattice with L^2 sites, and the number of B sites is $2L^2$. Lieb's theorem states that the ground state of the Hubbard model on this lattice, at half-filling, has total spin $\frac{1}{2}(|B| - |A|) = L^2/2$, or in other words, $1/2$ per unit cell, independently of the value of U. As the total spin of the ground state is proportional to the number of sites of the system, we say that the system displays ferromagnetism in a broad sense, or more precisely, ferrimagnetism[3]. In fact, in the Lieb lattice at half-filling, spins at

[3] If, additionally, the total spin of the ground state coincided with the maximum possible value (in the Lieb lattice, this would be $3L^2/2$), it would be called saturated ferromagnetism.

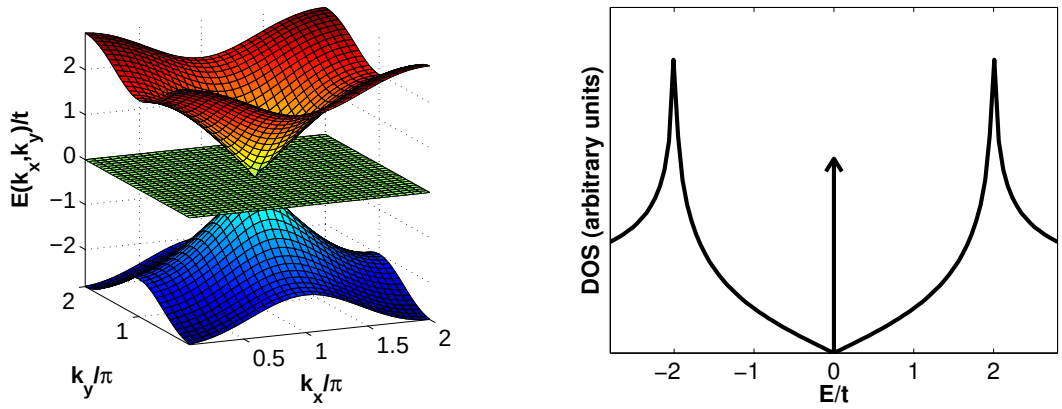

(a) (b)

Figure 2.5: (a) The tight-binding energy spectrum of the Lieb lattice comprises three bands. The two dispersive bands (red and blue) touch the zero-energy flat band at the Dirac point $\mathbf{k} = (\pi, \pi)$. The degeneracy of each band equals the number of unit cells of the lattice. (b) Density of states of the Lieb lattice, normalized to the number of unit cells. Due to the high degeneracy of the flat band, there is a Dirac delta at $E = 0$.

neighboring sites tend to point in opposite directions, but the difference between the number of B sites and A sites causes the system to exhibit finite magnetic moment. This occurs for Hubbard models in any bipartite lattice in which the difference in the number of sites of the two sublattices is proportional to the system size.

Lieb presents a single general proof of the theorem in that it applies for any positive U, be it small or large. In the limits of arbitrarily low U or very high U (compared with t), the theorem is easier to understand. Let us first consider the limit of very weak interactions. In bipartite lattices, the energy spectrum of the single-particle tight-binding Hamiltonian is symmetric with respect to 0 (see the example of the Lieb lattice in Fig. 2.5a). Therefore, at half-filling, all negative energy eigenstates are fully (doubly) occupied and the set of all zero energy eigenstates is half-filled. There is a large degeneracy of this ground state of the lattice, proportional to the degeneracy of the zero-energy level (equal to the number of unit cells). Introducing an arbitrarily low U partially lifts this degeneracy by forcing the eigenstates with zero energy to be filled with one electron each. Applying Hund's rule (higher S leads to lower energy), one concludes that all electrons have the same spin. As the degeneracy of the zero-energy level is $|B| - |A|$, then the total spin is $\frac{1}{2}(|B| - |A|)$.

If, on the other hand, we restrict ourselves to the subspace of states for which each site is occupied by one electron (this is the ground state at half-filling with $U \gg t$), the Hubbard model becomes a Heisenberg model (as we roughly saw in Sec. 2.1.3). Consequently, the total spin of the ground state of the Hubbard model in this limit is the same as that of the ground state of the Heisenberg model in the same lattice, i.e., $\frac{1}{2}(|B| - |A|)$.

In summary, Lieb's theorem states that the ground state of the Hubbard model at half-filling is antiferromagnetic or ferrimagnetic, depending on whether the two sublattices have the same number of sites or not, respectively. Although this is quite general, it applies only to finite lattices. Knowing the total spin of the ground state of a finite lattice does not necessarily determine the same property of the ground state of the corresponding infinite system. In fact,

long-range order has been proven to exist in the ground state of the anisotropic Heisenberg model in two or more dimensions [11], but no proof has been given for the Hubbard model, as the latter is more complex and allows for a broader range of quantum mechanical phenomena.

2.3 Uniform density theorem

The uniform density theorem dates back to 1940 for the $U = 0$ case [12]. It was later generalized to many interacting models, such as the Hubbard model [13, 14]. A simplified proof was later given by Lieb and collaborators [8]. The theorem applies to Hubbard models in bipartite lattices at half-filling, and is a consequence of the particle-hole symmetry [15].

Let $\rho_\sigma(x, y)$ be the one-particle density matrix, whose entries are the expectation values $\langle c^\dagger_{\sigma x} c_{\sigma y}\rangle$ in the ground state at $T = 0$, where $\sigma =\uparrow$ or $\downarrow$, and x and y are sites of the lattice. The theorem states

> *Let Λ be the set of all sites of a bipartite lattice, i.e., a lattice with $|\Lambda|$ sites, which can be divided into two disjoint sets (sublattices) A and B, such that the hopping parameter t_{xy} of the Hamiltonian, H, is only finite if x and y are in different sublattices. If the number of electrons equals the number of lattice sites ($N = |\Lambda|$), the ground state of H has the property*
>
> $$\rho_\sigma(x, y) = \frac{1}{2}\delta_{xy} \tag{2.21}$$
>
> *if x and y are in the same sublattice. If x and y are on different sublattices, nothing simple can be said.*

Note that the theorem does not impose any conditions on the hopping (t), or the interaction (U) parameters, nor does it require translational invariance. This implies, for example, that it also applies in the case of complex t, which occurs upon introduction of an external magnetic field. However, this magnetic field would also affect the spins of electrons, and in turn affect the particle-hole symmetry. In this thesis, we use this theorem to check our mean-field results on the Lieb lattice. For the results to agree with the theorem, the particle density at half-filling must be the same on every site of every sublattice and equal to

$$n_A = n_B = \rho_\uparrow(x, x) + \rho_\downarrow(x, x) = \sum_{\sigma=\uparrow,\downarrow} \langle c^\dagger_{\sigma x} c_{\sigma x}\rangle = 1. \tag{2.22}$$

2.4 Interacting electrons in a ring

In this section, we study the Hubbard model in a mesoscopic ring in the strong-coupling limit ($U \to \infty$). The Hamiltonian can be made translationally invariant through a gauge transformation, so that it becomes easily diagonalizable [16, 17]. The energy eigenvalues of this system are similar to those we obtain by applying a magnetic flux to a ring. Some thermodynamic functions are calculated in the case of an arbitrary number of holes. Some conclusions of this section are relevant and required for the study of the helicoidal Hubbard model in the same limit (see Chapter 4).

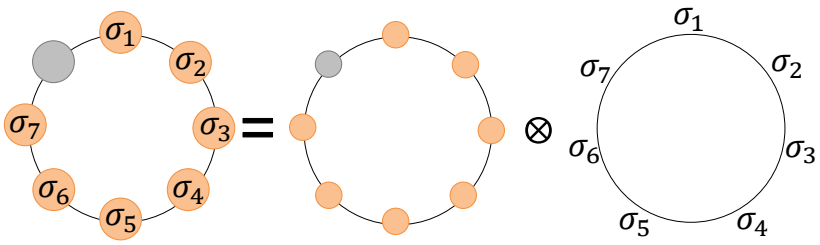

Figure 2.6: The eigenstates of the Hubbard ring in the strong coupling limit can be written as a tensorial product of the eigenstates of a tight-binding model of independent spinless fermions (holes) in the ring with L sites and the eigenstates of an Heisenberg model.

2.4.1 The Hubbard model in a ring

Let $U \to \infty$, so that no states with doubly occupied sites exist, as they are pushed to infinite energy. The Hubbard Hamiltonian (Eq. 2.2) for a ring of L sites, with no doubly occupied sites, becomes [18]

$$H = -t \sum_{i=1}^{L} \left[(1 - n_{i,\bar{\sigma}})\, c^{\dagger}_{i,\sigma} c_{i+1,\sigma}\, (1 - n_{i+1,\bar{\sigma}}) + H.c. \right]. \tag{2.23}$$

The eigenstates can be written as the tensorial product of the eigenstates of a tight-binding model of independent spinless fermions (holes) in a ring with L sites, and the eigenstates of an Heisenberg model (with exchange constant $J = t^2/U$) in a reduced chain [16, 18–21] (see Fig. 2.6). In the case of the Harris-Lange model, the Hamiltonian eigenvalues are determined by the set of the spinless fermions momenta, $\{k\}$, and the spin configuration total momentum, q.

One hole

The states of the lattice can be defined by indicating the position of the hole and the spin configuration of the rest of the ring[16]. For example, the notation

$$|2, \{\sigma_1, \sigma_2, \sigma_3\}\rangle \tag{2.24}$$

represents a ring with 4 sites, occupied by a hole at site 2, and the spins σ_1, σ_2 and σ_3 on the remaining sites (1, 3 and 4). Making the substitution $c^{\dagger}_j = n_j c^{\dagger}_j + (1 - n_j) c^{\dagger}_j$ and dropping the terms associated to double occupancies, the Hamiltonian for such a system becomes

$$H = -t \sum_{j,\sigma} (1 - n_{j,\bar{\sigma}}) c^{\dagger}_{j,\sigma} c_{j+1,\sigma} (1 - n_{j+1,\bar{\sigma}}) + (1 - n_{j+1,\bar{\sigma}}) c^{\dagger}_{j+1,\sigma} c_{j,\sigma} (1 - n_{j,\bar{\sigma}}). \tag{2.25}$$

Considering the hoppings of the particles is equivalent to considering those of the hole. The hoppings of the hole can be described using a simple tight-binding Hamiltonian, but one cannot ignore the spin configuration, because it changes when the hole hops from site L to 1 and vice versa, becoming one of its circular permutations. Let us introduce the circular permutation operator Q, such that

$$Q\, |j, \{\sigma_1, \sigma_2, ..., \sigma_{L-1}\}\rangle = |j, \{\sigma_{L-1}, \sigma_1, ..., \sigma_{L-2}\}\rangle\,, \tag{2.26}$$

i. e., the effect of Q on a state $|j,\{\sigma\}\rangle$ is equivalent to causing the hole to perform a full loop around the ring. The eigenstates of Q are states invariant in a circular permutation,

$$|j,\{\sigma\},q\rangle = \frac{1}{\sqrt{r_\alpha}} \sum_{m=0}^{r_\alpha-1} e^{iqm} Q^m \,|j,\{\sigma\}\rangle\,, \tag{2.27}$$

where

- r_α is the periodicity of the spin configuration, that is, the number of times the hole has to perform a full loop around the ring in order for the spins to return to their original configuration;
- α is the label of each set of spin configurations that are circular permutations of each other. Spin configurations with different α cannot be obtained from each other through a circular permutation;
- q is the momentum of the spin configuration,

$$q = \frac{2\pi}{r_\alpha} n, \tag{2.28}$$

  where $n = 0, 1, ..., r_\alpha - 1$.

Applying Q to one of its eigenstates gives

$$\begin{aligned} Q\,|j,\{\sigma\},q\rangle &= \tfrac{1}{\sqrt{r_\alpha}} e^{-iq} \sum_{m=0}^{r_\alpha-1} e^{iq(m+1)} Q^{m+1}\,|j,\{\sigma\}\rangle \\ &= e^{-iq}\,|j,\{\sigma\},q\rangle\,. \end{aligned} \tag{2.29}$$

In order to express the Hamiltonian in this basis, we need to apply it to all vectors in the basis,

- For $j = 2, 3, ..., L-1$,

$$H\,|j,\{\sigma\},q\rangle = t_\parallel \left(|j-1,\{\sigma\},q\rangle + |j+1,\{\sigma\},q\rangle\right) \tag{2.30}$$

- For $j = 1$,

$$\begin{aligned} H\,|1,\{\sigma\},q\rangle &= t_\parallel \left(|2,\{\sigma\},q\rangle + Q\,|L,\{\sigma\},q\rangle\right) \\ &= t_\parallel \left(|2,\{\sigma\},q\rangle + e^{-iq}\,|L,\{\sigma\},q\rangle\right) \end{aligned} \tag{2.31}$$

- For $j = L$

$$\begin{aligned} H\,|L,\{\sigma\},q\rangle &= t_\parallel \left(|L-1,\{\sigma\},q\rangle + Q^{-1}\,|1,\{\sigma\},q\rangle\right) \\ &= t_\parallel \left(|L-1,\{\sigma\},q\rangle + e^{iq}\,|1,\{\sigma\},q\rangle\right). \end{aligned} \tag{2.32}$$

Note that neither the spin configuration nor its momentum changed after applying the Hamiltonian, so we will drop them from this point. The Hamiltonian in this subspace becomes

$$H = t\left[\Big(|2\rangle + e^{-iq}\,|L\rangle\Big)\langle 1| + \Big(|L-1\rangle + e^{iq}\,|1\rangle\Big)\langle L| + \sum_{j=2}^{L-1}\Big(|j-1\rangle + |j+1\rangle\Big)\langle j|\right]. \tag{2.33}$$

The Hamiltonian can now be made translationally invariant by distributing the phase gain (or loss) among all L sites, instead of being applied only upon the sites at the boundaries, thus becoming

$$H = t\sum_{j=1}^{L}\left(e^{-iq/L}\left|j\right\rangle\left\langle j+1\right| + e^{iq/L}\left|j+1\right\rangle\left\langle j\right|\right). \tag{2.34}$$

This Hamiltonian is equivalent to the usual tight-binding model with an external flux $\phi = \phi_0 q/(2\pi)$ (here, $\phi_0 = h/e$ is the flux quantum), whose eigenvectors are

$$\left|k\right\rangle = \frac{1}{\sqrt{L}}\sum_{j=1}^{L} e^{ikj}\left|j\right\rangle, \tag{2.35}$$

with the corresponding eigenvalues

$$E(k) = 2t\cos\left(k - \frac{q}{L}\right). \tag{2.36}$$

On an infinite system, the ground state occurs at $k - q/L = \pi$, but on a finite system, the momentum q for which the ground state occurs depends on the parity of the number of sites, L. The lowest possible energy is $-2t$ which corresponds to $k - q/L = \pi$, and

$$n = \begin{cases} \frac{L+1}{2}, & \text{for } L \text{ odd}, \\ \frac{L}{2}, & \text{for } L \text{ even}. \end{cases} \tag{2.37}$$

Using these and regarding the definitions of q and k, we can calculate the value of q for the ground state in both situations,

$$q = \begin{cases} \pi, & \text{for } L \text{ odd}, \\ 0, & \text{for } L \text{ even}. \end{cases} \tag{2.38}$$

Let us study the degeneracy of these one-hole ground states. Ground states occur for specific values of k and q, for a given L, as mentioned above. However, degeneracy occurs due to the multiple values of r_α on the ground state (and respective spin configurations).

If L is even, the ground state occurs for $q = 0$, which, according to the definition of q, implies no restrictions upon r_α (the period of each class of spin configurations which are circular permutations of each other). This means that in the case of a ring on the ground state with an even number of sites, the spins may have any configuration, thus indicating a very high degeneracy, increasing as the number of sites L increases.

If L is odd, $q = \pi$ on the ground state. According to the definition of q, this implies that r_α is even. One can only conclude that, for a ring with an odd number of sites, only the spin configurations whose periodicity is even are allowed on the ground state. In particular, the ferromagnetic configuration (all spins aligned in the same direction) is not allowed [16]. These are usually more than half of the possible spin configurations, again indicating high spin degeneracy. This large degeneracy is lifted by the Heisenberg corrections (of t^2/U order), as in the case of the 2-site Hubbard model. Later in this work, it will be shown that this degeneracy is partially lifted on a helix by the transversal hopping term of the Hamiltonian.

N_h holes

Because there is now more than one hole, the states have to be labeled using a set $\{h\} = \{h_1, \cdots, h_{N_h}\}$ of the positions of the holes and a set $\{\sigma\} = \{\sigma_1, \cdots, \sigma_N\}$ of the positions of the spins,

$$|\{h\};\{\sigma\}\rangle = \prod_{j=1}^{N} c^\dagger_{b_j,\sigma_j}|0\rangle, \tag{2.39}$$

where $b_j = j + n_j(\{h\})$ and $n_j(\{h\})$ is the number of holes to the left of site j.

Let us introduce the slave-fermion representation of the fermionic operators [16] in the zero-double-occupancy subspace:

- $S^\dagger_{j,\sigma_j}$, the bosonic creation operator of a spin σ_j on site j;
- $e^\dagger_k$, the fermionic creation operator of a hole on site k,

such that $(1 - n_{j,\bar{\sigma}})c^\dagger_{j,\sigma} = S^\dagger_{j,\sigma}e_j$. Using slave-fermion notation, the state in Eq. 2.39 is represented as

$$|\{h\},\{\sigma\}\rangle = (-1)^{\sum_{j=1}^{N}(b_j-1)} \prod_{j=1}^{N} S^\dagger_{b_j,\sigma_j} \prod_{k=1}^{N_h} e^\dagger_{h_k} |0\rangle_{sh}\,, \tag{2.40}$$

where $|0\rangle_{sh}$ is the vacuum for both spins and holes. The first factor is due to the number of times the operator e_j needs to exchange with the $e^\dagger_{h_k}$ operators present in state $\prod_{k=1}^{N_h} e^\dagger_{h_k}|0\rangle_{sh}$. The Hamiltonian (Eq. 2.25) is represented as

$$H = t\sum_{j=1}^{L}\sum_{\sigma=\downarrow,\uparrow}\left(S^\dagger_{j+1,\sigma}S_{j,\sigma}e^\dagger_j e_{j+1} + S^\dagger_{j,\sigma}S_{j+1,\sigma}e^\dagger_{j+1}e_j\right). \tag{2.41}$$

In order to diagonalize this Hamiltonian, we proceed in a way similar to solving the $N_h = 1$ case. We begin by building states invariant in a circular permutation Q,

$$|\{h\},\{\sigma\},q\rangle = \frac{1}{\sqrt{r_\alpha}}\sum_{m=0}^{r_\alpha-1} e^{iqm}Q^m\,|\{h\},\{\sigma\}\rangle\,, \tag{2.42}$$

where r_α is the periodicity of the spin configuration $\{\sigma\}$ (labeled by α), and

$$q = \frac{2\pi}{r_\alpha}n, \qquad n = 0, \cdots, r_\alpha - 1. \tag{2.43}$$

Again, we need to apply the Hamiltonian to the state $|\{h\},\{\sigma\},q\rangle$ in order to express it in that basis. Let

$$\left|\{h'\}\right\rangle = e^\dagger_{j+1}e_j\,|\{h\}\rangle\,. \tag{2.44}$$

Applying one of the Hamiltonian's j-terms to state $|\{h\},\{\sigma\},q\rangle$ gives

$$\sum_\sigma S^\dagger_{j,\sigma}S_{j+1,\sigma}e^\dagger_{j+1}e_j\,|\{h\},\{\sigma\},q\rangle\,, \tag{2.45}$$

without changing the spin configuration, because a spin is exchanged with a hole, never exchanged with another spin. The Hamiltonian does, however, change the positions of the holes to $\{h'\}$ and moves the spin on site $j+1$ to site j, implying subtracting 1 to one of the b_j, if $j \neq L$. If $j = L$, we need to add $L-1$ to one of the b_j and a phase q:

$$\sum_\sigma S^\dagger_{j,\sigma} S_{j+1,\sigma} e^\dagger_{j+1} e_j \left|\{h\},\{\sigma\},q\right\rangle = \begin{cases} (-1) & \left|\{h'\},\{\sigma\},q\right\rangle \quad \Leftarrow j \neq L \\ (-1)^{L-1} e^{iq} & \left|\{h'\},\{\sigma\},q\right\rangle \quad \Leftarrow j = L \end{cases} \tag{2.46}$$

The application of the Hamiltonian Eq. 2.41 can only induce circular permutations of the spin configuration and therefore does not change the actual cyclic relative positions of the spins. This means we can discard the terms containing spin operators keeping only the hole operators, and write the Hamiltonian as

$$H_q = \sum_{j=1}^{L} t_j \left(e^\dagger_j e_{j+1} + e^\dagger_{j+1} e_j \right), \tag{2.47}$$

where $t_{j\neq L} = -t$ and $t_L = -te^{i(q-\pi L)}$.

We apply a gauge transformation like the one in the previous subsection, thus distributing the phase $q - \pi L$ among all L sites, so that

$$t_j = -te^{i(q-\pi L)/L} = te^{iq/L}, \tag{2.48}$$

and the Hamiltonian becomes translationally invariant,

$$H_q = t \sum_{j=1}^{L} \left(e^{iq/L} e^\dagger_{j+1} e_j + e^{-iq/L} e^\dagger_j e_{j+1} \right), \tag{2.49}$$

reflecting the fact that, because the spin sequence remains unchanged, the system can be regarded as a set of N_h independent spinless fermions on a lattice with L sites. The eigenvalues are

$$E(k_1, \cdots, k_{N_h}) = 2t \sum_{j=1}^{N_h} \cos\left(k_j - \frac{q}{L}\right), \tag{2.50}$$

with

$$k_j = \frac{2\pi}{L} n_j \qquad n_j = 0, \cdots, L-1. \tag{2.51}$$

The eigenvalues depend only on L, N_h and r_α. It is important to note that this implies that all eigenstates with the same spin configuration periodicity are associated to the same eigenvalues, leading to high degeneracy. Part of this degeneracy is lifted when the geometry is changed from a ring to a helix.

2.4.2 Counting the q states

An approach to the problem of counting the number of eigenstates of the $U \to \infty$ Hubbard chain which have a given momentum q has already been made by Mielke [22]. Here, we present a faster method for counting how many spin configurations have a certain periodicity. Note that in this section, we replace the n in the definition of the momentum q of the eigenstates by j.

Let us consider a chain of N spins. The periodicity of that chain may range from 1 to N. Not all values are possible, though, only those that divide N. In order to better understand this concept, we may think of a spin chain with N spins and periodicity n, as a set of N/n equal parts with periodicity n. For example, a chain of length $N = 12$ could be

$$\uparrow\uparrow\downarrow\uparrow\uparrow\downarrow\uparrow\uparrow\downarrow\uparrow\uparrow\downarrow\,. \tag{2.52}$$

Its periodicity is $n = 3$ and it is composed of $12/3 = 4$ parts equal to

$$\uparrow\uparrow\downarrow, \tag{2.53}$$

with periodicity 3. Thus, the problem of calculating the number of possible spin configurations of a chain with N spins and periodicity n is reduced to that of calculating the number of spin configurations of a chain with only n spins and periodicity n.

For example, calculating the number of spin configurations that have periodicity 3 for a chain with 90 spins is equivalent to calculating the ways in which 3 spins can be arranged to form a chain with periodicity 3. Those ways are

$$\begin{array}{lll} \uparrow\downarrow\downarrow, & \downarrow\uparrow\downarrow, & \downarrow\downarrow\uparrow, \\ \downarrow\uparrow\uparrow, & \uparrow\downarrow\uparrow, & \uparrow\uparrow\downarrow, \end{array} \tag{2.54}$$

where $\uparrow\uparrow\uparrow$ and $\downarrow\downarrow\downarrow$ are not included because their periodicity is 1. In the general case, the number of spin configurations with periodicity n is 0 if n does not divide N, and

$$P(n) = 2^n - \sum_d P(d), \tag{2.55}$$

if n divides N. The letter d stands for all divisors of n, except for n itself. A plot of this function for the first 20 values of n is shown in Fig. 2.7. Note the logarithmic scale of the vertical axis, which was used to show that this function (dots) quickly approaches $P(n) \approx 2^n$ (full line).

To sum up, the possible periodicities of a chain of N spins are the divisors, n, of N. For each of these divisors, the number of spin configurations which lead to that periodicity is given by $P(n)$. In the specific case of N prime, spin configurations can only have periodicity 1 or N. The ones with periodicity 1 are $\uparrow\uparrow\uparrow\cdots\uparrow\uparrow$ and $\downarrow\downarrow\downarrow\cdots\downarrow\downarrow$; all the remaining $2^N - 2$ configurations have periodicity N.

Now that we know how many configurations exist for each periodicity, it becomes easier to calculate the number of eigenstates for each momentum q. The definition of q is, again,

$$q = \frac{2\pi}{r_\alpha} j \qquad\qquad j = 0, 1, \cdots, r_\alpha - 1. \tag{2.56}$$

Let us assume, for instance, that we have $N = 6$ spins and we want to know how many eigenstates have the momentum $q = \frac{2\pi}{6} \cdot 4$. The immediate answer would be "the number of eigenstates with momentum $2\pi/6 \cdot 4$ is the number of configurations with periodicity 6, divided by 6" (we need to divide by 6 because each eigenstate is the superposition of 6 configurations that are circular permutations of each other, implying that there are less eigenstates than configurations), i. e., the answer would be $P(6)/6$. However, since we have $q = \frac{2\pi}{6} \cdot 4 = \frac{2\pi}{3} \cdot 2$, there are $P(3)/3$ eigenstates made up of configurations with periodicity 3 which can also have

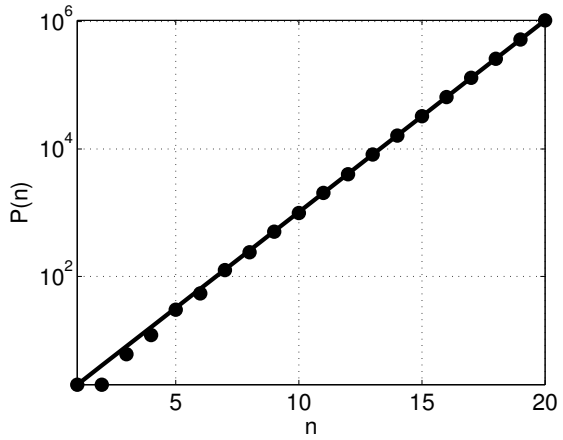

Figure 2.7: Plot of the $P(n)$ function for $n \in [1, 20]$ (dots). For each n, $P(n)$ gives the number of spin configurations which have period n. The line is the function 2^n and was added here for comparison.

this momentum value. Therefore, in the general case, if the number of spins is N, the number of eigenstates with momentum $q = \frac{2\pi}{N} \cdot j$ is

$$N_s(N, q) = \sum_g \frac{P(N/g)}{N/g}, \tag{2.57}$$

where the summation is taken over the common divisors of N and j. As we approach the thermodynamic limit, $N_s(N, q) \approx \frac{2^N}{N}$.

2.4.3 Thermodynamics

Using the results from the previous subsection, we can calculate thermodynamic functions of the Hubbard chain in the strong-coupling limit. We begin by defining the partition function, Z, as

$$Z = \sum_r e^{-E_r/(k_B T)}, \tag{2.58}$$

where r labels all possible states of the system.

We know that no more than one hole can occupy each k state. This implies that each of the N_h holes can have any value of k as long as no other hole has it. Therefore, the number of eigenstates the holes can occupy is obtained by counting the number of combinations of N_h values that can be extracted from the list of L possible values of k, that is, $\binom{L}{N_h}$.

For the $N = L - N_h$ spins, we know from the previous subsection that the number of states with spin momentum q is given by the function $N_s(N, q)$.

The partition function can be numerically calculated for fixed L and N_h using the expression

$$Z = \sum_{\{k\}} \sum_q N_s(N, q) e^{-E(\{k\})/(k_B T)}, \tag{2.59}$$

where

- the first summation is taken over all the different combinations of N_h values of k;

- the second summation is taken over $q = 2\pi/N \cdot j$ with $j = 0, \cdots, N-1$ (the counting of the spin periodicities that are divisors of N is included in $N_s(N, q)$);
- the energy eigenvalues are $E(\{k\}) = 2t_{\parallel} \sum_{i=1}^{N_h} \cos\left(k_i - \frac{q}{L}\right)$.

The partition function can be used to calculate the thermodynamic energy,

$$\langle E \rangle = -\frac{\partial \ln Z}{\partial \beta}, \tag{2.60}$$

the heat capacity,

$$C_v = \frac{\partial \langle E \rangle}{\partial T}, \tag{2.61}$$

and the entropy of the system,

$$S = \frac{\partial}{\partial T} \left(k_B T \ln Z\right), \tag{2.62}$$

as a function of $k_B T$.

Energy

Fig. 2.8a shows a few plots of the energy as a function of $k_B T$, each corresponding to $N_h = 1, \cdots, 5$, and fixed $L = 10$. It can be seen that, as the number of holes increases, the energy decreases. Additionally, we see that for high T, the energy goes to 0, which is explained by the fact that holes and particles have the same probability of occupying a state. There are as many positive eigenvalues as there are negative ones, thus their average is zero.

Heat capacity

Fig. 2.8b contains plots of the heat capacity as a function of $k_B T$, for $L = 10$ and different values of N_h, ranging from 1 to 5. Both on the C_v and $\langle E \rangle$ plots, particle-hole symmetry is present (the Hamiltonian in Eq. 2.49 also has particle-hole symmetry), so that the functions $C_v(T)$ or $\langle E \rangle(T)$ for have the same expression for N_h and $L - N_h$.

Entropy

The entropy (Fig. 2.9) is the thermodynamic function whose analysis is the most interesting one. The symmetry present in the previous two functions is valid no more. In fact, as S is a measure of the number of available states, it changes when a spin is replaced by a (spinless) hole.

For $T \to \infty$, all states are equally probable, and we can calculate the entropy analytically in this limit. The number of states accessible to the N_h holes is $\binom{L}{N_h}$ and the number of states accessible to the spins is 2^N, therefore

$$S(T \to \infty)/k_B = S_\infty/k_B = \ln\left(\frac{L!}{N_h! N!} 2^N\right). \tag{2.63}$$

Another effect that can be seen from the plots is the fact that, for low T, more holes mean lower entropy. The holes occupy the k states which lead to lowest energies. However, for high T, the system with the lowest N_h is no longer the one with the highest entropy. This occurs

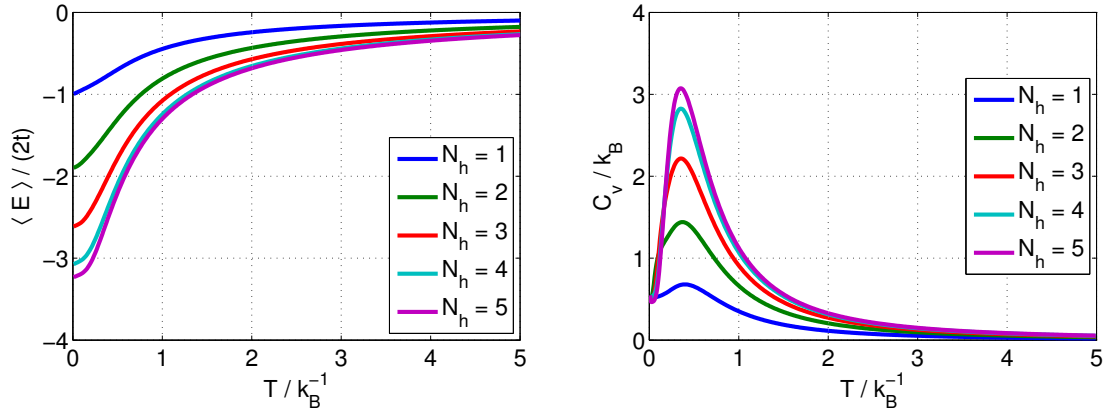

(a) (b)

Figure 2.8: (a) Average energy, $\langle E \rangle$, and (b) heat capacity, C_v, of the strong-coupling Hubbard chain with $L = 10$. The plots for N_h and for $L - N_h$ are identical, due to particle-hole symmetry of the Hamiltonian (Eq. 2.49).

because S_∞ has a maximum with respect to N_h, which can be calculated analytically, using Stirling's approximation $\ln N! \approx N \ln N - N$, allowing the approximation of

$$\frac{dS_\infty(N_h)}{dN_h} = k_B \frac{d}{dN_h} \ln\left(\frac{L!}{N_h!(L-N_h)!} 2^{L-N_h}\right), \tag{2.64}$$

to

$$\frac{1}{k_B}\frac{dS_\infty(N_h)}{dN_h} \approx -\ln 2 + \frac{d}{dN_h}\left(-N_h \ln N_h + N_h - (L-N_h)\ln(L-N_h) + (L-N_h)\right). \tag{2.65}$$

The equation $\frac{dS_\infty(N_h)}{dN_h} = 0$ has only one solution, $N_h = L/3$. This is the solution for continuous N_h. For our discrete case, the maximum will occur for $L/3$ rounded to the nearest integer. For $L = 10$ (Fig. 2.9), that integer is 3, providing the reason why the plot of S for $N_h = 3$ has the highest value when $T \to \infty$.

Let us now study what happens to the entropy when we only allow ferromagnetic states (the only states with periodicity $r_\alpha = 1$). The lattice now has N_h holes and $L - N_h$ equal spins, which implies particle-hole symmetry is present once again, because the spin chain is only allowed two states ($\uparrow\uparrow\uparrow\cdots$ and $\downarrow\downarrow\downarrow\cdots$), independently of the number of spins. Fig. 2.10 shows the entropy for lattices with $L = 9$ (left) and $L = 10$ (right) sites. In the $T \to \infty$ limit, the entropy goes to

$$\begin{aligned} S_\infty &= k_B \ln(\text{number of spin states} \times \text{number of hole states}) \\ &= k_B \ln\left[2 \times \binom{L}{N_h}\right] \\ &= k_B \ln\left[2 \times \frac{L!}{N_h!(L-N_h)!}\right] \end{aligned} \tag{2.66}$$

independently of the parity of L and N_h.

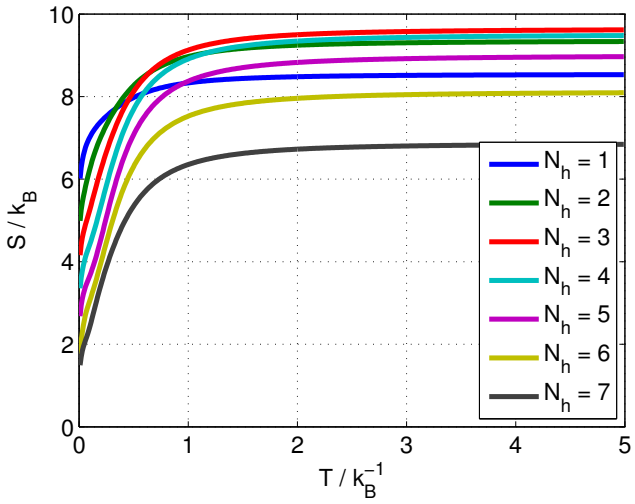

Figure 2.9: Entropy, S, of the strong-coupling Hubbard chain in the $t_\perp = 0$ limit, with $L = 10$. For high T, the maximum entropy occurs for $N_h = L/3$ rounded to the nearest integer which, in this case, is 3.

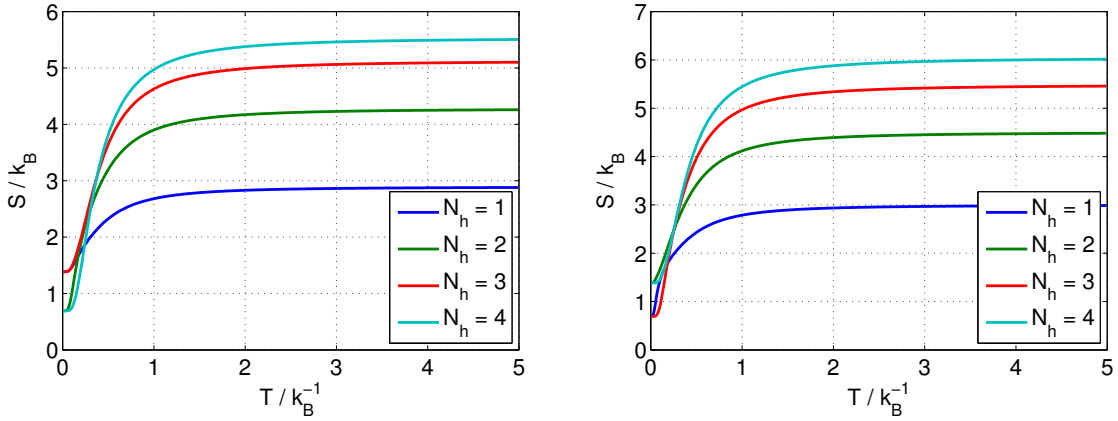

(a) (b)

Figure 2.10: Entropy of the ferromagnetic strong-coupling Hubbard chain in the $t_\perp = 0$ limit, for (a) $L = 9$ (odd) and (b) $L = 10$ (even). In this limit, the entropy of the model shares the particle-hole symmetry with the average energy and the heat capacity, because only two states are allowed to the spin chain, independently of its length.

However, in the $T \to 0$ limit, the spins will still have only 2 allowed states, while the holes may have a single or a doubly-degenerate ground k state. Recalling the definition of the momentum of the holes, $k = \frac{2\pi}{L} n$, with $n = 0, \cdots, L-1$, we conclude that the ground state $k = \pi$ is only allowed for L even. If the number of holes is odd, one of them will occupy the bottom of the band, and the rest will fill it in pairs, symmetrically, meaning the ground state of the holes is unique. If the number of holes is even, one hole will remain after symmetrically filing up the states; this hole can either occupy either one of the two lowest free states in the band, leading to a doubly-degenerate global ground state. In contrast, for an odd L, holes can no longer occupy the $k = \pi$ state. Consequently, there are two band states with the lowest energy. Contrarily to what happens for L even, an even number of holes can only occupy one global ground state, while an odd number of holes has two possibilities for its global ground state.

These results for the ferromagnetic configuration are summarized in the following table (where S is in units of k_B),

		$S(T=0)$	$S(T \to \infty)$
L even	N_h even	$\ln 4$	$\ln(2 \times \binom{L}{N_h})$
	N_h odd	$\ln 2$	$\ln(2 \times \binom{L}{N_h})$
L odd	N_h even	$\ln 2$	$\ln(2 \times \binom{L}{N_h})$
	N_h odd	$\ln 4$	$\ln(2 \times \binom{L}{N_h})$

For example, the entropy of the ferromagnetic strong-coupling Hubbard chain with an even number of sites (L) and an odd number of holes (N_h) at $T = 0$ is $\ln 2$.

References

[1] F. H. L. Essler et al. *The One-Dimensional Hubbard Model*. Cambridge Press, 2005.

[2] V. Celebonovic. "The Hubbard model: basic notions and selected applications". *arXiv:1002.2794 [cond-mat.mtrl-sci]* (2010).

[3] H. Bethe. "Zur Theorie der Metalle". *Zeitschrift für Physik* 71 (1931), pp. 205–226.

[4] E. Lieb. "The Hubbard Model: Some Rigorous Results and Open Problems". *arXiv:cond-mat/9311033v2* (1993).

[5] A. Mielke. "The Hubbard Model and its Properties". *Modeling and Simulation* 5 (2015), pp. 1–26.

[6] C. N. Yang and S. Zhang. "SO_4 symmetry in a Hubbard model". *Modern Physics Letters B* 04.11 (1990), pp. 759–766.

[7] E. H. Lieb. "Two Theorems on the Hubbard model". *Physical Review Letters* 62 (1989), pp. 1201–1204.

[8] E. H. Lieb, M. Loss, and R. J. McCann. "Uniform density theorem for the Hubbard model". *Journal of Mathematica Physics* 34 (1993), pp. 891–898.

[9] P. W. Anderson. "New Approach to the Theory of Superexchange Interactions". *Phys. Rev.* 115 (1959), pp. 2–13.

[10] H. Tasaki. "The Hubbard model - an introduction and selected rigorous results". *J. Phys.: Condens. Matter* 10.20 (1998), p. 4353.

[11] T. Kennedy. "Long range order in the anisotropic quantum ferromagnetic Heisenberg model". *Communications in Mathematical Physics* 100.3 (1985), pp. 447–462.

[12] C. A. Coulson and G. S. Rushbrooke. "Note on the method of molecular orbitals". *Mathematical Proceedings of the Cambridge Philosophical Society* 36 (1940), pp. 193–200.

[13] A. D. McLachlan. "The pairing of electronic states in alternant hydrocarbons". *Molecular Physics, vol. 2, Issue 3, p.271-284* (1959).

[14] A. McLachlan. "Electrons and holes in alternant hydrocarbons". *Molecular Physics, vol. 4, Issue 1, p.49-56* (1961).

[15] D. Baeriswyl et al. *The Hubbard model : its physics and mathematical physics*. Springer US, 1995.

[16] R. G. Dias and J. M. B. Lopes dos Santos. "Simple representation of the eigenstates of the $U \to \infty$ one-dimensional Hubbard model". *Journal de Physique I* 2 (1992), pp. 1889–1897.

[17] A. J. Schofield, J. M. Wheatley, and T. Xiang. "Diamagnetic susceptibility of the $\infty - UHubbardmodel$". *Phys. Rev. B* 44.15 (1991), pp. 8349–8352.

[18] N. M. R. Peres et al. "Finite-temperature transport in finite-size Hubbard rings in the strong-coupling limit". *Phys. Rev. B* 61.8 (2000), pp. 5169–5183.

[19] M. Ogata and H. Shiba. "Bethe-ansatz wave function, momentum distribution, and spin correlation in the one-dimensional strongly correlated Hubbard model". *Phys. Rev. B* 41 (1990), pp. 2326–2338.

[20] F. Gebhard et al. "Exact results for the optical absorption of strongly correlated electrons in a half-filled Peierls-distorted chain". *Phil. Mag. B* 75 (1997), pp. 13–46.

[21] R. G. Dias and J. D. Gouveia. "Origami rules for the construction of localized eigenstates of the Hubbard model in decorated lattices". *Scientific Reports, 16852* (2015).

[22] A. Mielke. "The one-dimensional Hubbard model for large or infinite U". *Journal of Statistical Physics* 62.3 (1991), pp. 509–528.

Chapter 3

Spiral ferrimagnetic phases in the two-dimensional Hubbard model

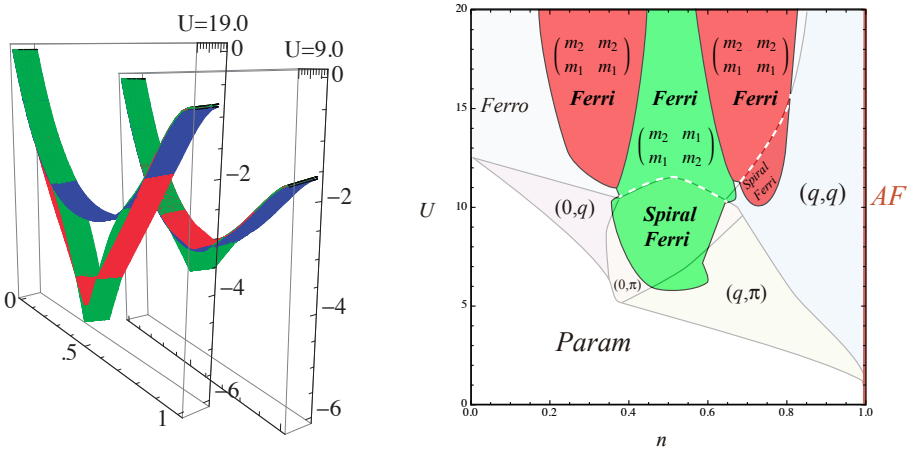

Adapted from:
J. D. Gouveia and R. G. Dias, Spiral ferrimagnetic phases in the two-dimensional Hubbard model. Solid State Communications, Volume 185, May 2014, Pages 21-24
DOI: 10.1016/j.ssc.2014.01.004

Abstract

We address the possibility of spiral ferrimagnetic phases in the mean-field phase diagram of the two-dimensional (2D) Hubbard model. For intermediate values of the interaction U ($6 \lesssim U/t \lesssim 11$) and doping n, a spiral ferrimagnetic phase is the most stable phase in the (n, U) phase diagram. Higher values of U lead to a non-spiral ferrimagnetic phase. If phase separation is allowed and the chemical potential μ replaces the doping n as the independent variable, the (μ, U) phase diagram displays, in a considerable region, a spiral (for $6 \lesssim U/t \lesssim 11$) and non-spiral (for higher values of U) ferrimagnetic phase with fixed particle density, $n = 0.5$, reflecting the opening of an energy gap in the mean-field quasi-particle bands.

3.1 Introduction

The 2D Hubbard model remains the most important open theoretical problem in the field of the strongly correlated electronic systems, despite all efforts fuelled by the advent of the high-T_c superconductivity.[1, 2] At half-filling, the spin dynamics of the 2D Hubbard model is described by the Heisenberg antiferromagnetic exchange term.[3] Away from half-filling, the movement of holes through the spin background generates additional spin mixing. The competition between the Heisenberg exchange and the spin configuration mixing generated by hole hopping in the 2D Hubbard model is still far from understood.[4–6] In particular, there is no consensus regarding the ground state magnetic phase diagram of the 2D Hubbard model and different authors obtain different mean-field (MF) phase diagrams depending on the magnetic phases allowed.[7] Traditionally, one considered ferromagnetism, antiferromagnetism and paramagnetism phases.[8–12] The complexity of the MF phase diagram was increased with the introduction of spiral phases[13], which appear between the "usual" magnetic phases in the diagram. This complexity was further increased by the consideration of spatial phase separation.[14–16]

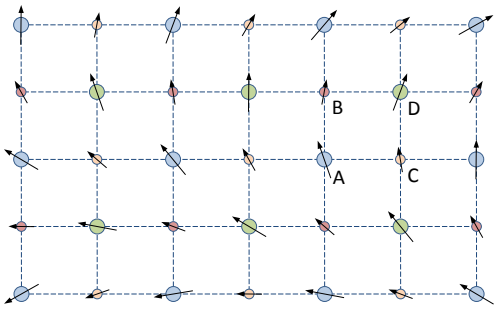

Figure 3.1: The 2D lattice and its four sublattices A, B, C and D. We consider two situations: (i) $m_A = m_D = m_1$ and $m_B = m_C = m_2$; (ii) $m_A = m_C = m_1$ and $m_B = m_D = m_2$.

In this paper, we extend the results above mentioned, by introducing the possibility of a spiral ferrimagnetic phase, that is, a ferrimagnetic phase such that the orientation of magnetic moments changes along the lattice (see Fig. 3.1). More precisely, we study the 2D Hubbard model using the Hartree-Fock approximation in a square lattice decomposing the lattice in four square sublattices (A, B, C and D as in Fig. 3.1) and allowing different amplitudes for magnetizations of the spiral phases in the sublattices. Note that, even under the MF approximation, when four sublattices are considered, it is not possible to obtain the analytical form of the spectra of the 2D Hubbard model. Our MF approach to the 2D Hubbard model follows that of Dzierzawa and Singh.[17, 18]

3.2 Calculations

Introducing a different creation operator in each sublattice, $A^\dagger$, $B^\dagger$, $C^\dagger$ and $D^\dagger$, the tight-binding term of the Hubbard Hamiltonian, is

$$\begin{aligned} H_t = & \sum_{x,y} A^\dagger_{x,y}B_{x,y} + A^\dagger_{x,y}C_{x,y} \\ & + B^\dagger_{x,y}D_{x,y} + C^\dagger_{x,y}D_{x,y} \\ & + A^\dagger_{x,y}B_{x,y-1} + A^\dagger_{x,y}C_{x-1,y} \\ & + B^\dagger_{x,y}D_{x-1,y} + C^\dagger_{x,y}D_{x,y-1} + H.c., \end{aligned} \tag{3.1}$$

where we set the hopping constant equal to 1.

We consider for now only the sublattice A (we add the other sublattice terms later on). The interaction term of the Hubbard Hamiltonian is, as usual, $H_U = U\sum_r A^\dagger_{r\uparrow}A_{r\uparrow}A^\dagger_{r\downarrow}A_{r\downarrow}$. We assume that the magnetic moments align in the x-y plane, so that $\langle S_z\rangle = 0$ and the Hartree term becomes $\frac{U}{4}\sum\langle n\rangle^2$, where $\langle n\rangle$ is the density of electrons on each sublattice (here assumed to be the same on all of them).

The Fock term includes averages like $\langle A^\dagger_\uparrow A_\downarrow\rangle = \langle S^+_A\rangle = \langle S_{Ax} + iS_{Ay}\rangle$, whose values depend on the magnetic phase. Let us assume the average spin in the sublattice A is

$$\langle \vec{S}_{\vec{r}_A}\rangle = \frac{m_A}{2}[\cos(\vec{q}\cdot\vec{r}_A), \sin(\vec{q}\cdot\vec{r}_A), 0]. \tag{3.2}$$

The vector $\vec{q} = (q_x, q_y)$ defines the magnetic phase of the system. In $\vec{k}$-space we have

$$\langle S^+_{A\vec{k}}\rangle = \frac{1}{\sqrt{L}}\sum_{\vec{k}'}\langle A^\dagger_{\vec{k}',\uparrow}A_{\vec{k}'-\vec{k},\downarrow}\rangle = \frac{m_A\sqrt{L_{u.c.}}}{2}\delta_{\vec{k},-\vec{q}}, \tag{3.3}$$

where $L_{u.c.}$ is the number of unit cells, which gives

$$\langle A^\dagger_{\vec{k},\uparrow}A_{\vec{k}+\vec{q},\downarrow}\rangle = \frac{m_A}{2}, \tag{3.4}$$

while all the other mean values in the summation of Eq. 3.3 vanish. The Fock term in Fourier space is

$$-\frac{mU}{2}\sum_{\vec{k}}\left(A^\dagger_{\vec{k}+\vec{q},\downarrow}A_{\vec{k},\uparrow} + A^\dagger_{\vec{k},\uparrow}A_{\vec{k}+\vec{q},\downarrow}\right) + \frac{UL_{u.c.}}{4}m_A^2. \tag{3.5}$$

Adding the tight-binding, Hartree and Fock terms, the Hamiltonian H_{MF} reads, in the $\{A_{\vec{k}}, B_{\vec{k}}, C_{\vec{k}}, D_{\vec{k}}, A_{\vec{k}+\vec{q}}, B_{\vec{k}+\vec{q}}, C_{\vec{k}+\vec{q}}, D_{\vec{k}+\vec{q}}\}$ basis,

$$\begin{pmatrix} H_t(\vec{k}) & H_m \\ H_m^\dagger & H_t(\vec{k}+2\vec{q}) \end{pmatrix}, \tag{3.6}$$

plus the diagonal term

$$\frac{UL_{u.c.}}{4}(m_A^2 + m_B^2 + m_C^2 + m_D^2) + \frac{UL\langle n\rangle^2}{2}. \tag{3.7}$$

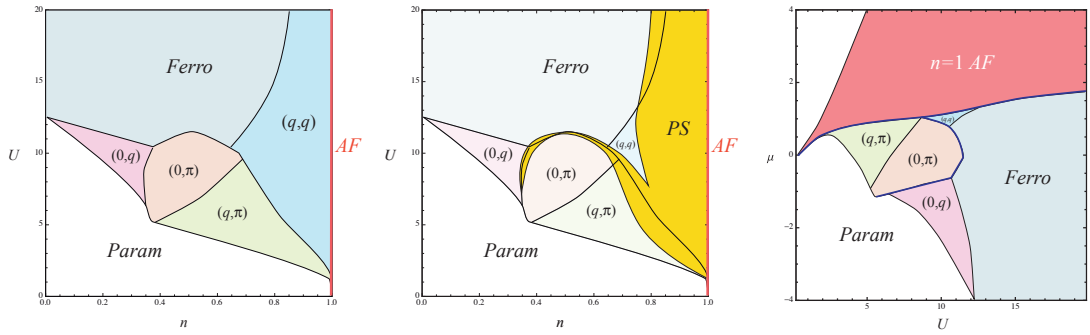

(a) (n, U) phase diagram (b) (n, U) phase diagram with phase separation (c) (U, μ) phase diagram with phase separation

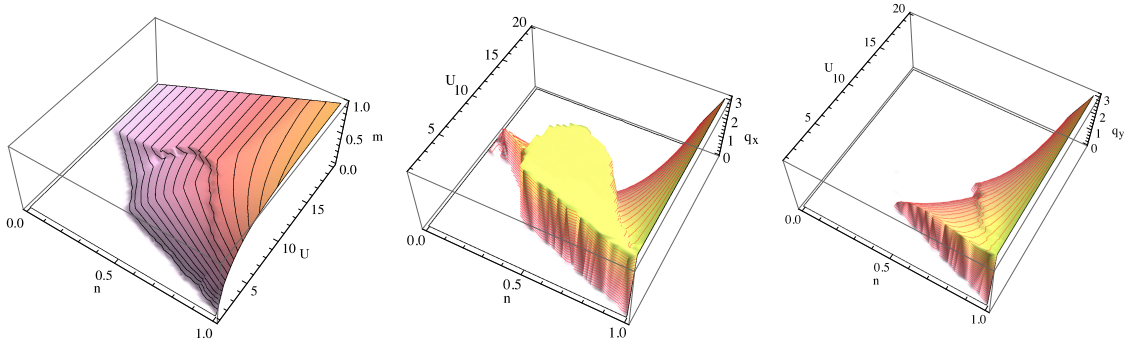

(d) $m(n, U)$ (e) $q_x(n, U)$ (f) $q_y(n, U)$

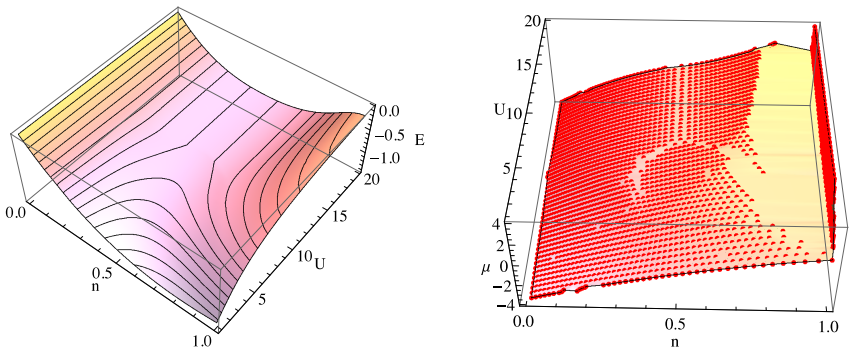

(g) $E(n, U)$ (h) $\mu(n, U)$

Figure 3.2: (a) Mean-field phase diagram for the usual 2D Hubbard model: The system displays antiferromagnetism (AF), ferromagnetism (F), paramagnetism (P) or spiral phases ($q \neq 0, \pi$). The antiferromagnetic state $\vec{q} = (\pi, \pi)$ only occurs for $n = 1$ (half-filling). (b) (n, U) and (c) (U, μ) mean-field phase diagrams for the 2D Hubbard model, allowing for phase separation (yellow region). (d) m, (e) q_x, (f) q_y, (g) E_{MF} and (h) μ as functions of the doping n and Coulomb interaction U, for the 100×100 2D Hubbard model.

Here, $H_t(\vec{k})$ is the tight-binding term (Eq. 3.1) of the Hamiltonian in $\vec{k}$-space,

$$\begin{pmatrix} 0 & 1+e^{ik_y} & 1+e^{ik_x} & 0 \\ 1+e^{-ik_y} & 0 & 0 & 1+e^{ik_x} \\ 1+e^{-ik_x} & 0 & 0 & 1+e^{ik_y} \\ 0 & 1+e^{-ik_x} & 1+e^{-ik_y} & 0 \end{pmatrix}, \tag{3.8}$$

H_m is the diagonal matrix, $H_m = \mathrm{diag}(\Delta_A, \Delta_B, \Delta_C, \Delta_D)$ with

$$\begin{aligned} \Delta_A &= -\frac{Um_A}{2}, & \Delta_B &= -\frac{Um_B}{2}e^{iq_y}, \\ \Delta_C &= -\frac{Um_C}{2}e^{iq_x}, & \Delta_D &= -\frac{Um_D}{2}e^{iq_x+iq_y}. \end{aligned} \tag{3.9}$$

3.3 Results and discussion

By setting $m_A = m_B = m_C = m_D = m$, we recover the MF magnetic phase diagram of the usual 2D Hubbard model, consistent with the ones obtained by several authors[13, 15, 17] for zero temperature, as presented in Fig. 3.2a. In order to obtain such a diagram, one minimizes either the MF energy E_{MF} using the electronic density n as an independent variable, or the thermodynamic potential Ω_{MF} using the chemical potential μ, with respect to the site magnetization amplitude m and the order parameter $\vec{q} = (q_x, q_y)$. These parameters define the magnetic phase of the system.

A solution with $m = 0$ is paramagnetic and is usually $\vec{q}$-degenerate, while solutions for $m \neq 0$ are in general unique. In the latter case, the wave vector $\vec{q}$ specifies the type of magnetic ordering. For instance, $\vec{q} = (0, 0)$ for the ferromagnetic phase, $\vec{q} = (\pi, \pi)$ for the antiferromagnetic phase and all other choices for spiral phases. In the example shown in Fig. 3.1, we have $q_x = \pi/18$ and $q_y = \pi/6$. Additionally, in the same example, the magnetization amplitudes (denoted by the size of the arrows) are $m_A = m_D = m_1$ and $m_B = m_C = m_2 < m_1$. Comparing, for each pair (n, U) or (U, μ), the data obtained for m (Fig. 3.2d), q_x (Fig. 3.2e) and q_y (Fig. 3.2f), the MF magnetic phase diagram displayed in Fig. 3.2a ensues. For some values of μ, there is more than one pair $(\vec{q}, m)$ which minimizes the thermodynamic potential. In those cases, a first-order phase transition in the order parameters occurs. When using n as a basic variable (and posteriorly calculating $\mu = \partial E/\partial n \approx \Delta E/\Delta n$ using the data in Fig. 3.2g), n seems to be multiply defined for some values of μ, which implies instability (e. g. of the spiral phase for $U = 15$). The use of μ as a basic variable solves this ambiguity and leads to plateaus in the chemical potential $\mu(n, U)$ in the regions where phase separation (PS) occurs (see Fig. 3.2h). In each PS region of the diagram, two spatially separated phases occur: the ones immediately to the left and to the right of the PS region in question (see Fig. 3.2b). The two phases have different electronic densities, such that the electronic density of the whole system amounts to n. In Fig. 3.2c, we show the same phase diagram as in Fig. 3.2a, but using μ as the independent variable. The colors of corresponding regions are the same for easier reading. The thick solid line indicates a discontinuity in n.

In this work, the magnetic phase diagram for the Hubbard 2D model comprising four sublattices is obtained by finding the magnetization amplitudes (m_A, m_B, m_C, m_D) and the vector $\vec{q}$ which minimize the energy. We consider two situations: (i) $m_A = m_D = m_1$ and $m_B = m_C = m_2$; (ii) $m_A = m_C = m_1$ and $m_B = m_D = m_2$.

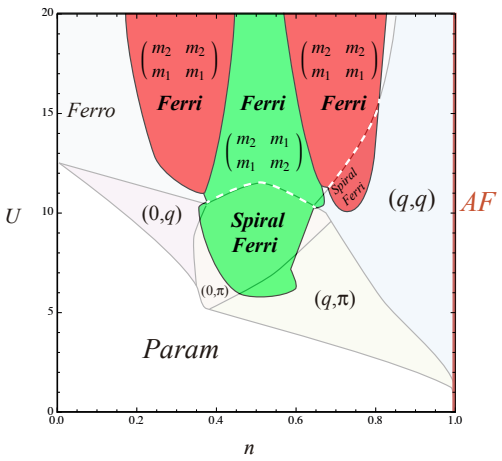

(a) (n, U) phase diagram

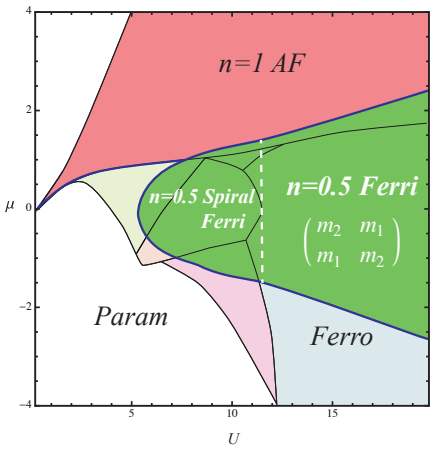

(b) (U, μ) phase diagram with phase separation

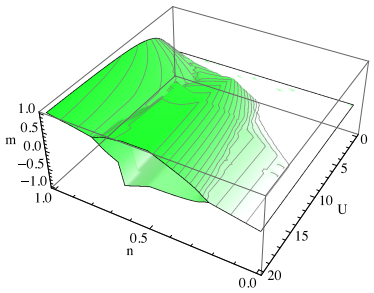

(c) m_1, m_2 (i)

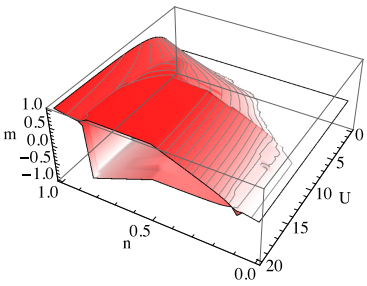

(d) m_1, m_2 (ii)

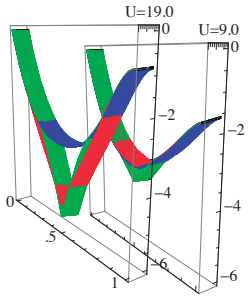

(e) $E(n, U)$

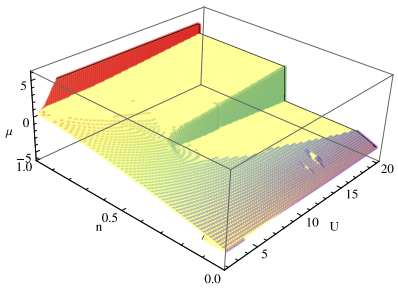

(f) $\mu(n, U)$

Figure 3.3: Top figures: (a) Mean-field phase diagram for the 2D Hubbard model with sublattices with independent magnetization amplitudes. In the central (green) region of the phase diagram, configuration (i) is the one that minimizes the MF energy, while configuration (ii) is the most stable in the red regions. (b) (U, μ) mean-field phase diagram with phase separation occurring on the borders of the green and red regions (thick solid lines). This phase diagram displays spiral and non-spiral ferrimagnetic phases (green regions) with fixed particle density, $n = 0.5$, reflecting the opening of an energy gap in the MF quasi-particle bands. Bottom figures: $m_1(n, U)$ and $m_2(n, U)$ for the MF 2D Hubbard model with two sublattices in (c) configuration (i) and (d) configuration (ii). (e) Ground state MF energy for usual 2D (blue), case (i) (green) and case (ii) (red) for $U = 9$ and $U = 19$. (f) μ as a function of the doping n and Coulomb interaction U. All figures represent numerical results obtained for the 100×100 2D Hubbard model with two sublattices with different magnetization amplitudes.

The ground state magnetization amplitude of the usual 2D Hubbard model is proportional to n for each value of U in the ferromagnetic phase (see Fig. 3.2d). When a spiral ferrimagnetic phase is allowed, it was found that, near zero filling ($n = 0$) and half-filling ($n = 1$), the ground state magnetization remains the same as in the usual 2D case (see Figs. 3.3c and 3.3d). This means that in these regions, the ground state magnetization is still constant throughout the whole lattice. However, as one moves to intermediate n, one finds that m_1 and m_2 become distinct, as shown in Figs. 3.3c and 3.3d for cases (i) and (ii) respectively, where m_1 and m_2 are displayed as a function of n and U. These figures show two sheets reflecting the separation of the magnetization amplitudes. The colors green for case (i) and red for (ii) are used on all plots of Fig. 3.3. For intermediate filling, the system is able to lower its energy by adopting different magnetization amplitudes on sublattices 1 and 2 in both cases (i) and (ii). This is shown in Fig. 3.3e for $U = 19$ and $U = 9$. Depending on the region of the phase diagram one analyses, configuration (i) or (ii) may have the lowest energy, as shown in Fig. 3.3a. In this figure, we added another layer on top of the usual 2D MF magnetic phase diagram, showing which of the two-sublattice configurations considered has the lowest energy in the ferrimagnetic region: green for case (i) and red for case (ii). Furthermore, the energy was minimized with respect to q_x and q_y, while using the new magnetization values, but it was found that only very small changes in $\vec{q}$ occur, i.e., despite the changes in magnetization amplitudes, the magnetic phases in the diagram remain the same. For this reason, the magnetic phases are shown as being the same as those of the usual 2D model.

The mean-field energy dispersion relation of the usual 2D Hubbard model displays two bands. Electrons occupy the lowest band until half-filling ($n = 1$) and then proceed to occupying the higher band. As can be seen in Fig. 3.2h, the fermionic density increases with the chemical potential until the phase separation region is reached. In this region, the chemical potential is constant despite any increase in the number of particles, up to half-filling. At this point, any increase in n induces a jump in the value of μ, equal to the energy separation between the two energy bands (called the energy gap). As the plot in Fig. 3.2h only goes up to half-filling, we see μ increasing smoothly until it reaches the phase separation region, followed by a plateau and a jump at $n = 1$. In both cases studied in this work, with the lattice divided into two sublattices, the energy bands open a gap at quarter filling ($n = 0.5$), as shown in Fig. 3.3f. Another gap appears at three quarter filling ($n = 0.75$), but only the phases with $n \leq 1$ are shown in Fig. 3.3b. The plot in Fig. 3.3b is again the same as Fig. 3.3a, but using μ as the basic variable. In this diagram, the green region corresponds to $n = 0.5$, therefore only configuration (i) for the spiral and non spiral ferrimagnetic phases is present in the phase diagram. The dashed line separates the ferrimagnetic region from the spiral ferrimagnetic one and the thick solid lines denote again discontinuities in n.

3.4 Conclusion

Having addressed the possibility of a spiral ferrimagnetic phase in the mean-field phase diagram of the 2D Hubbard model, we conclude that, for intermediate values of the interaction U and doping n, the spiral ferrimagnetic phase is the most stable phase in the (n, U) phase diagram. Higher values of U lead to non-spiral ferrimagnetic phases. We emphasize the case of intermediate n and higher U, for which the ground state does not appear to be purely ferromagnetic, contrasting with results by other authors.[15] Additionally, allowing phase separation and replacing n by μ as the independent variable, the (μ, U) phase diagram displays,

in a considerable region, spiral (for intermediate values of U) and non-spiral (for higher values of U) ferrimagnetic phases with fixed particle density, $n = 0.5$, reflecting the opening of an energy gap in the mean-field quasi-particle bands. We further note that generalizing the ferrimagnetic phase to cases where more than two different magnetization amplitudes are allowed should lead to even more stable ferrimagnetic phases in certain regions of the phase diagram. Preliminary results with three different amplitudes are consistent with this conjecture. All these results provide strong evidence on the stability of the spiral ferrimagnetic phase in the mean field magnetic phase diagram of the 2D Hubbard model.

References

[1] J. G. Bednorz and K. A. Müller. "Possible high T_c superconductivity in the Ba-La-Cu-O system". *Zeitschrift fur Physik B Condensed Matter* 64 (1986), pp. 189–193.

[2] M. A. Kastner et al. "Magnetic, transport, and optical properties of monolayer copper oxides". *Rev. Mod. Phys.* 70 (1998), pp. 897–928.

[3] R. G. Dias and J. M. B. Lopes dos Santos. "Simple representation of the eigenstates of the $U \to \infty$ one-dimensional Hubbard model". *Journal de Physique I* 2 (1992), pp. 1889–1897.

[4] F. Gebhard et al. "Exact results for the optical absorption of strongly correlated electrons in a half-filled Peierls-distorted chain". *Phil. Mag. B* 75 (1997), pp. 13–46.

[5] M. Ogata and H. Shiba. "Bethe-ansatz wave function, momentum distribution, and spin correlation in the one-dimensional strongly correlated Hubbard model". *Phys. Rev. B* 41 (1990), pp. 2326–2338.

[6] Y. Nagaoka. "Ground state of correlated electrons in a narrow almost half-filled s band". *Solid State Communications* 3 (1965), pp. 409–412.

[7] M. P. Marder. *Condensed Matter Physics*. John Wiley and Sons, 2000.

[8] D. R. Penn. "Stability Theory of the Magnetic Phases for a Simple Model of the Transition Metals". *Phys. Rev.* 142 (1966), pp. 350–365.

[9] J. Dorantes-Dávila, J. L. Morán-López, and M. Avignon. "Ground-state solutions of the Hubbard model". *Phys. Rev. B* 27 (1983), pp. 575–577.

[10] E. Kaxiras and E. Manousakis. "Ground state of the strong-coupling Hubbard Hamiltonian: A numerical diagonalization study". *Phys. Rev. B* 37 (1988), pp. 656–659.

[11] S. N. Coppersmith and C. C. Yu. "Phase diagram of the Hubbard model: A variational wave-function approach". *Phys. Rev. B* 39 (1989), pp. 11464–11474.

[12] A. Richter, G. Röpke, and F. Goedsche. "Functional Integral Approach for the Hubbard Model with Arbitrary Electron Density". *Physica Status Solidi B Basic Research* 88 (1978), pp. 189–198.

[13] S. Sarker et al. "Spiral states in the square-lattice Hubbard model". *Phys. Rev. B* 43 (1991), pp. 8775–8778.

[14] E. Langmann and M. Wallin. "Mean Field Magnetic Phase Diagrams for the Two Dimensional $t - t' - U$ Hubbard Model". *Journal of Statistical Physics* 127 (2007), pp. 825–840.

[15] P. A. Igoshev et al. "Incommensurate magnetic order and phase separation in the two-dimensional Hubbard model with nearest- and next-nearest-neighbor hopping". *Phys. Rev. B* 81 (2010), p. 094407.

[16] W. Schumacher. "On incommensurate phases in the magnetic phase diagram of the hubbard model". *physica status solidi (b)* 119.1 (1983), pp. 235–238.

[17] M. Dzierzawa. "Hartree-Fock theory of spiral magnetic order in the 2-d Hubbard model". *Z. Phys. B* 86 (1992), pp. 49–52.

[18] A. Singh, Z. Tesanovic, and H. H. Kim. "Instability of the spiral state of the doped Hubbard model". *Pramana - J. Phys.* 38 (1992), pp. 211–217.

Chapter 4

Quantum spin queues in the strong-coupling helicoidal Hubbard model

In this chapter, we study the Hubbard model in a helicoidal lattice as a variation of the square lattice. While previous studies of this geometry consider single-particle Hamiltonians, here we work in the strong-coupling limit, propose an effective Hamiltonian to describe the spin dynamics in this limit, and solve it in some cases.

4.1 Introduction

An exact solution of the Hubbard model for any value of U is known in the one-dimensional case, given by the Bethe Ansatz method [1]. By this method, it was confirmed that there are no phase transitions in the 1D Hubbard model with short-range correlations, in agreement with the Mermin-Wagner theorem [2].

The Hubbard model in a helicoidal lattice was first studied in the form of a 1D chain of atoms in which both first- and third-nearest neighbor hoppings were considered [3] and later generalized to a helix with an arbitrary number of atoms per loop [4]. Approximate solutions were obtained in order to recover some of the properties of the 2D Hubbard model. A third study [5] includes arbitrary long-range hopping terms but considers no interactions. More recently, the helicoidal geometry was studied using the discrete nonlinear Schroedinger equation, rather than the Hubbard model [6]. This study was partly motivated by the recently-proposed experimental implementation of helix-shaped trapping potentials for cold atoms [7]. The helicoidal geometry has also attracted interest in the context of DNA modeling (see for instance Ref. [8] and references therein).

A helix is a space curve with parametric equations

$$\begin{aligned} x &= r\,\cos(t) \\ y &= r\,\sin(t) \\ z &= b\,t \end{aligned} \quad , \tag{4.1}$$

with $0 \leq t \leq 2\pi N_{\text{loop}}$, where N_{loop} is the number of helix loops, r is the radius of the helix and b controls the vertical (along the z direction) separation between loops (equal to $2\pi b$). In this work, we consider L atoms, equidistantly placed along a helicoidal curve, with Δ atoms per

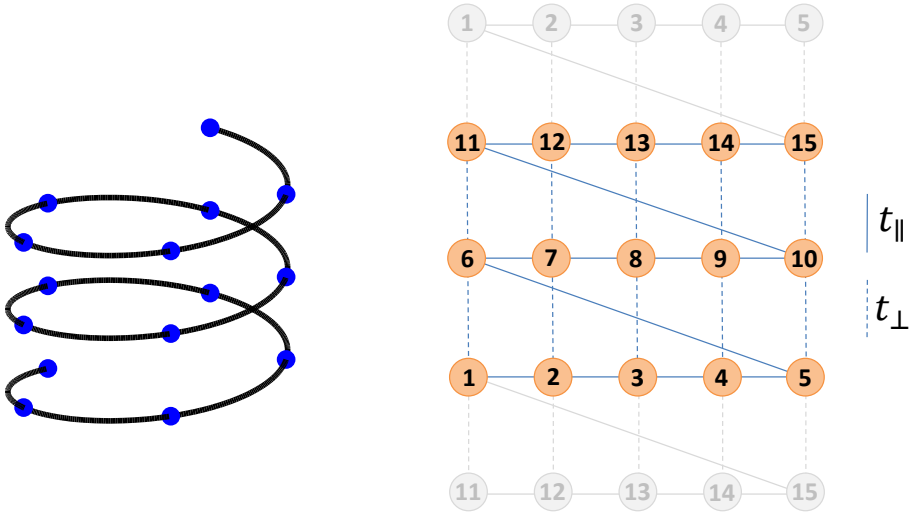

Figure 4.1: On the left, a helix with 15 sites ($L = 15$) and 3 loops of arc length 5 ($\Delta = 5$). We assume periodic boundary conditions at the two ends of the helix (i.e., a toroidal helix). On the right, the one-dimensional labeling of sites used in this work, applied to the case of a helix with 15 sites and 5 atoms per helix loop, and including the periodic boundary. Our tight-binding Hamiltonian of the helicoidal lattice assumes a toroidal helix geometry and allows two types of electron hop: along the helix (with hopping parameter $t_\parallel$) and perpendicularly to the helix arc ($t_\perp$). In the traditional periodic square lattice tight-binding model, successive applications of $t_\parallel$ to state $|1\rangle$ (an empty lattice, except for an electron on site 1) would give all states between $|1\rangle$ and $|5\rangle$. In contrast, in the helicoidal lattice, the $t_\parallel$ term of the Hamiltonian generates the full set of helix sites (from $|1\rangle$ to $|15\rangle$, in this example). Using the notation of this manuscript, the helix shown here has $L = 15$ and $\Delta = 5$.

---

helix loop, so that the parameter t becomes discretized, $t = \frac{2\pi}{\Delta} j$, and each value of $j = 1, \cdots, L$ corresponds to the index of an atom. The euclidean distance between any two atoms, with indexes j_1 and j_2 depends only on the difference between their indexes, $|j_1 - j_2|$. The distance, d, between nearest neighbors ($|j_1 - j_2| = 1$) is given by

$$d^2 = 4r^2 \sin^2(\pi/\Delta) + \left(\frac{2\pi b}{\Delta}\right)^2. \tag{4.2}$$

Therefore, for the distance between nearest neighbors to be the same as the vertical separation between helix loops, the following relation between r and b must be satisfied,

$$r^2 \sin^2(\pi/\Delta) = \left(\frac{\pi b}{\Delta}\right)^2 (\Delta^2 - 1). \tag{4.3}$$

The helicoidal Hubbard model can be regarded both as a special case of a square lattice (because we allow electrons to hop in two orthogonal directions) and as a special case of a linear chain of atoms (because we naturally generate all possible positions of a particle using only one parameter). An example of site labeling for a helix of length $L = 15$ is shown in Fig. 4.1. If this situation was of toroidal (periodic square lattice) geometry, mixing in the spin configurations would take place due to hoppings (i) at the left/right boundaries of the

lattice, (ii) at the top/bottom boundaries of the lattice, and (iii) between sites whose label differs by 5 units. In contrast, on a helicoidal lattice, spin configurations are only mixed when a particle/hole hops between sites 15 and 1 (as if this lattice was a ring with 15 sites), or between corresponding sites in different helix loops.

4.2 Hubbard model

We consider finite hopping parameters along the helix ($t_{\parallel}$) and perpendicularly to the helix arc ($t_{\perp}$). In the thermodynamic limit, the helicoidal Hubbard model is equivalent to the usual Hubbard model in a square lattice, the difference lying in the boundary conditions (see Fig. 4.1). The advantage of the helicoidal lattice over the usual 2D square lattice is that a single translation operator (along the helix path) generates the full set of helix sites. In addition, the tight-binding Hamiltonian of the helix with $t_{\perp} = 0$ is considerably less degenerate than that of a square lattice with, for example, $t_y = 0$. Furthermore, the eigenstates of the helicoidal tight-binding model with $t_{\perp} = 0$ *remain eigenstates* when $t_{\perp} \neq 0$.

The Hubbard Hamiltonian for a system of arbitrary geometry with L sites is given by

$$\hat{H} = -\sum_{i,j} t_{ij} c^{\dagger}_{i,\sigma} c_{j,\sigma} + U \sum_{i} \hat{n}_{i,\uparrow} \hat{n}_{i,\downarrow}, \tag{4.4}$$

where the creation (annihilation) operator of an electron at site i with spin σ is denoted by $c^{\dagger}_{i\sigma}$ ($c_{i\sigma}$) and $\hat{n}_{i\sigma}$ is the number operator $\hat{n}_{i\sigma} = c^{\dagger}_{i\sigma} c_{i\sigma}$. The dimensionality of the Hubbard model and its geometry is determined by the relative position dependence of the hopping integral t_{ij}. In the particular case of the helicoidal tight-binding model considered here, we adopt a one-dimensional indexation of sites (see Fig. 4.1), and we assume t_{ij} is non-zero for hoppings between nearest-neighbors along the helix ($t_{i,i+1} = t_{\parallel}$), and across the helix ($t_{i,i+\Delta} = t_{\perp}$), from site i to site $i + \Delta$. The helicoidal lattice is assumed to have a total of L sites and periodic boundary conditions as shown in Fig. 4.1. The distance between sites along the helix is considered unitary so that the total arc length of the helix is equal to the number of sites.

In the rest of this chapter, we work in the limit $U \gg t_{\parallel} \gg t_{\perp} \gg t_{\parallel}^2/U$. The reason to consider $t_{\parallel} \gg t_{\perp}$ is that we assume the distance between sites is in principle smaller for adjacent ones (along the helix) than for sites in different helix steps.

4.3 Tight-binding limit ($U = 0$)

In the atomic limit ($t_{ij} = 0$), the eigenvalues of any Hubbard model are given by $E_{N_d} = N_d.U$ and all states with the same number of doubly occupied sites, N_d, are degenerate.

On the other hand, for $U = 0$, the helicoidal Hubbard model becomes a tight-binding model of independent electrons. For $t_{\perp}$=0, one has the energy dispersion relation of a 1D chain, $\epsilon_k = -2t_{\parallel} \cos(k)$ with $k = (2\pi/L) \cdot n$ and $n = 1, \cdots, L$. Since for $t_{\perp} \neq 0$ the tight-binding Hamiltonian is invariant under translation along the helix, the eigenstates are again k-states, with eigenvalues given by

$$E_k = -2t_{\parallel} \cos(k) - 2t_{\perp} \cos(k\Delta). \tag{4.5}$$

This dispersion relation is illustrated in Fig. 4.2 for several lattice sizes and relative values of $t_{\parallel} = 1$ and $t_{\perp}$. The lattice size is 10×10 atoms for the first three plots, and 20×20 for the

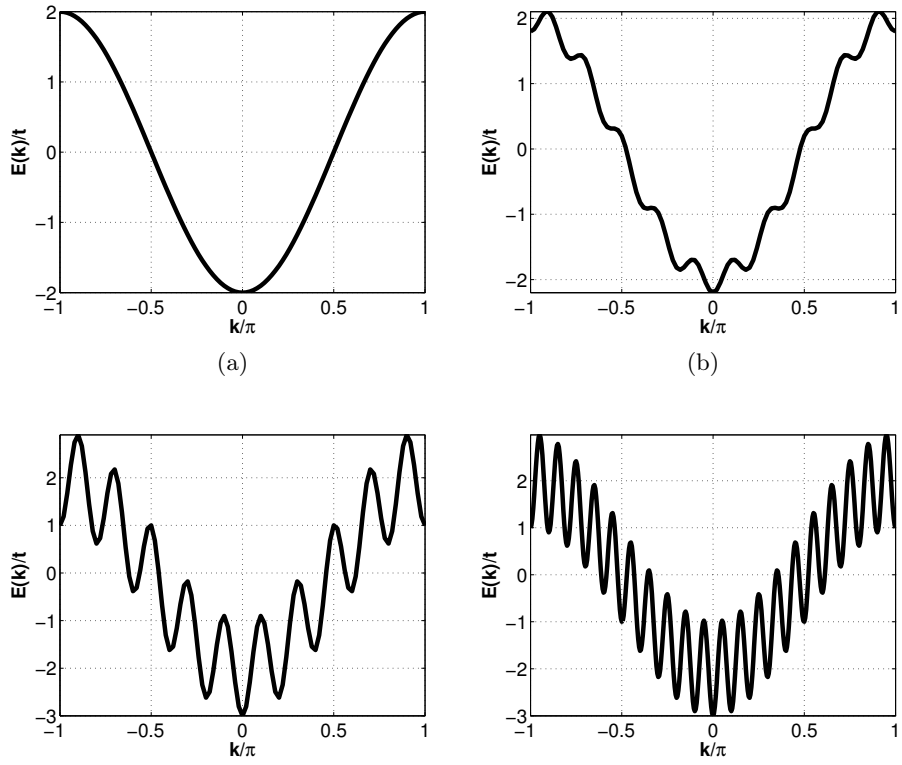

Figure 4.2: Illustrations of the tight-binding dispersion relation of the helicoidal model, given by Eq. 4.5. The changes in the shape of the plots are due to tweaking the size of the lattice, as well as the relative values of the longitudinal and transversal hoppings ($t_{\parallel}$ and $t_{\perp}$). In the first plot (a), the dispersion relation was reduced to that of the 1D TB model, by setting $t_{\parallel} = 1$ and $t_{\perp} = 0$. In the other three plots, finite transversal hopping parameters were considered, namely $t_{\perp} = 0.1$ (b) and $t_{\perp} = 0.5$ (c and d). The size of the lattice was kept at 10×10 atoms on all plots except the last one, for which the size is 20×20.

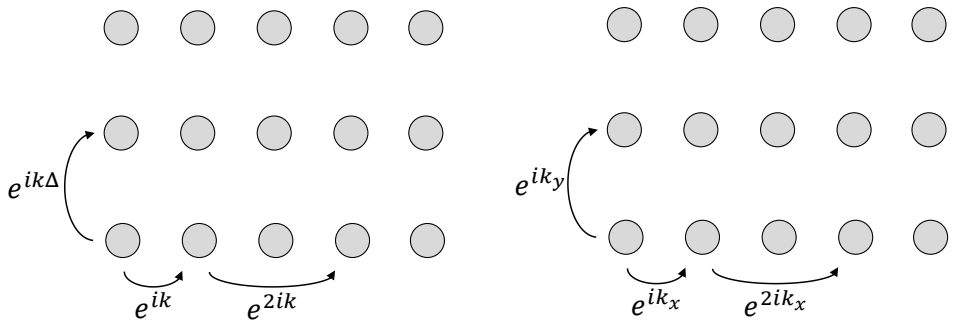

Figure 4.3: A hop along the x-direction induces a phase e^{ik} on a helix (left) or e^{ik_x} on a square lattice (right). A hop along the y-direction induces a phase $e^{ik\Delta}$ on a helix or e^{ik_y} on a 2D model. On a helix, hopping $\Delta = L_x$ times in the x-direction induces a phase $e^{ik\Delta} = e^{ik_x\Delta} = e^{ik_xL_x} = e^{ik_y}$, when a twisted boundary condition is imposed upon the square lattice model.

fourth one. The plot in Fig. 4.2a corresponds to the limit $t_\perp = 0$ and coincides with that of the dispersion relation of the usual TB model of a 1D periodic chain of atoms. Note that in this limit ($t_\perp = 0$), changing the size of the lattice has no effect on the plot. As a matter of fact, because the lattice is finite, one should see dots rather than a continuous line, but the point here is that those dots fall on the same line (the line obtained for an infinite-sized chain) regardless of the chosen lattice size. The other plots in Fig. 4.2 consider transversal hopping with amplitude $t_\perp = 0.1$ (Fig 4.2b) and $t_\perp = 0.5$ (Figs. 4.2c and 4.2d). One concludes that the presence of the transversal ($t_\perp$) hopping term of the Hamiltonian leads to the appearance of the higher-mode oscillations that can be seen in the plots in Figs. 4.2b-4.2d, whose frequency can be controlled by changing the lattice size. One important consequence of this is that the band acquires a larger number of maxima and minima as the lattice size increases, and the extrema of the band may be shifted to values of k other than 0 and $\pm\pi$. This effect becomes more substantial if one considers longer-range hoppings [5].

As $t_\perp$ increases from 0 to values of the same order of $t_{||}$, the set of eigenvalues of the helix tight-binding Hamiltonian approaches that of the square lattice, in the thermodynamic limit. In fact, the density of states of the tight-binding model on a helix and on a square lattice become the same in the thermodynamic limit, so long as the size of both lattices is the same (if the dimensions of the square lattice are L_x and L_y, then the dimensions of the helix could be $L_x = \Delta$ and $L_y = L/\Delta$).

In Eq. 4.5, only one momentum variable, k, was used to describe a behavior that is equivalent to the square lattice tight-binding one in the thermodynamic limit,

$$E_{k_x,k_y} = -2t_{\parallel}\cos(k_x) - 2t_\perp\cos(k_y), \tag{4.6}$$

with

$$\begin{array}{ll} k_x = \frac{2\pi}{L_x}n_x & n_x = 1, \cdots, L_x \\ k_y = \frac{2\pi}{L_y}n_y & n_y = 1, \cdots, L_y. \end{array} \tag{4.7}$$

The relation between the helicoidal lattice wave number and the square lattice wave vector can be found by imposing the twisted boundary condition, $e^{ik_xL_x} = e^{ik_y}$ (this can be read as "hopping L_x times in the x direction of the helix is equivalent to hopping once in the y

direction"). This condition is equivalent to

$$\begin{aligned} k_x = \tfrac{2\pi}{L_x} n_x &= \tfrac{k_y}{L_x} + \tfrac{2\pi}{L_x} n' \\ &= \tfrac{k_y}{Lx} + k'_x. \end{aligned} \tag{4.8}$$

The equivalence between the two models requires $L_x = \Delta$ and $L_y = L/\Delta$. We can therefore write the dispersion relation for the square lattice with twisted boundary conditions,

$$E'_{k_x,k_y} = -2t_{\parallel} \cos\left(\frac{k_y}{\Delta} + k'_x\right) - 2t_{\perp} \cos(k_y), \tag{4.9}$$

and, comparing Eqs. 4.9 and 4.5,

$$k = \frac{k_y}{\Delta} + k'_x \Leftrightarrow k\Delta = k_y + 2\pi n', \tag{4.10}$$

or, in terms of n,

$$n = \left(\frac{L}{\Delta}\right) \cdot n_x + n_y \Rightarrow \begin{cases} n_x = \text{int}\,\left(\frac{n}{L/\Delta}\right), \\ n_y = \text{mod}\,(n, L/\Delta), \end{cases} \tag{4.11}$$

From Eq. 4.9, two relations between k and (k'_x, k_y) can be extracted, but they are equivalent. From the previous expressions, the usual points of the two-dimensional Brillouin zone can be obtained: $k = \pi \Rightarrow (k_x, k_y) = (\pi, 0)$, $k = \pi/\Delta \Rightarrow (k_x, k_y) = (0, \pi)$, and $k = \pi + \pi/\Delta \Rightarrow (k_x, k_y) = (\pi, \pi)$.

In the following table, we illustrate the correspondence between the wave vector of the square lattice tight-binding model and the wave number of the helicoidal tight-binding model, for $L_x = 2$ and $L_y = 3$ (and consequently $L = 6$).

n	n_x	n_y	k	k_x	k_y
0	0	0	0	0	0
1	0	1	$\frac{\pi}{3}$	0	$\frac{2\pi}{3}$
2	0	2	$\frac{2\pi}{3}$	0	$\frac{4\pi}{3}$
3	1	0	π	π	0
4	1	1	$\frac{4\pi}{3}$	π	$\frac{2\pi}{3}$
5	1	2	$\frac{5\pi}{3}$	π	$\frac{4\pi}{3}$

. (4.12)

For the remainder of this chapter, we take the strong-coupling limit ($U \to \infty$), so that all states with double occupancies are pushed to infinite energy and are therefore not allowed. In the absence of transversal hopping ($t_{\perp} = 0$), a helix with L sites is mathematically equivalent to a ring with the same number of sites, and therefore its analysis is the same as that of a ring, replacing the hopping parameter of the latter by $t_{\parallel}$.

4.4 Strong-coupling limit ($U \to \infty$)

In the absence of the $t_{\perp}$ term of the Hamiltonian, the solution of the helicoidal Hubbard model in the strong-coupling limit reduces to that of the Hubbard chain. The eigenstates are characterized by the momenta of the holes, $\{k\}$, and the momentum of the spin configuration, q. The eigenvalues are

$$\epsilon(\{k\}, q) = 2t_{\parallel} \sum_{j=1}^{N_h} \cos\left(k_j - \frac{q}{L}\right), \tag{4.13}$$

with

$$k_j = \frac{2\pi}{L} n_j \qquad\qquad n_j = 0, \cdots, L-1. \tag{4.14}$$

The existence of translation invariance in the original chain as well as in the spinless chain and the squeezed spin chain allows a considerable simplification of the transverse hopping term $t_\perp$. The introduction of the $t_\perp$ hopping term lifts the degeneracy of the eigenvalues $\epsilon(\{k\}, q)$ of the Harris-Lange model given by Eq. 2.50. The energy correction of order $t_\perp$ requires the diagonalization of the $t_\perp$ hopping term within each $(\{k\}, q)$ subspace.

4.4.1 Momentum

The total momentum of a state $|\{k\}; q\rangle$ can be obtained from the phase acquired by the system under a translation of one site and is given by

$$P = \sum_{i=1}^{N_h} k_i + \frac{q}{L} N + \delta \tag{4.15}$$

where $\delta = \pi \bmod (L-1, 2)$. This expression can be partially confirmed since the total momentum has to be a multiple of $2\pi/L$ due to the invariance of the problem in a translation of L. In terms of the two-dimensional momentum vectors (k_x, k_y), this expression becomes

$$P = \sum_{i=1}^{N_h} k_{xi} + \frac{1}{\Delta} \sum_{i=1}^{N_h} k_{yi} + \frac{q}{L} N + \delta \tag{4.16}$$

The $1/\Delta$ factor reflects the fact that hoppings in the y direction occur only in one of Δ sites. The x and y components of P are

$$P_x = \sum_{i=1}^{N_h} k_{xi} + k_{x0}, \tag{4.17}$$

$$P_y = \sum_{i=1}^{N_h} k_{yi} + k_{y0}, \tag{4.18}$$

where

$$k_{x0} + \frac{k_{y0}}{\Delta} = \frac{q}{L} N + \delta \tag{4.19}$$

so that $P = P_x + P_y/\Delta$. Note that $\frac{q}{L} N + \delta$ is a multiple of $2\pi/L$.

4.4.2 Hamiltonian

Using the slave-fermion representation, the $t_\perp$ hopping term becomes, in the subspace $(\{h\}, q)$,

$$\hat{H}_\perp(\{h\}, q) = t_\perp \sum_{\substack{i=1 \\ \sigma}}^{L} e^{-i(\frac{q}{L} - \pi)\Delta} S^\dagger_{i+\Delta,\sigma} S_{i,\sigma} e^\dagger_i e_{i+\Delta} + \text{H.c.} \tag{4.20}$$

where the gauge transformation, Eq. 2.48, was taken into account. This term corresponds to a jump of the electron in site i to site $i + \Delta$, which in turn implies a jump of a spin in site i' of the squeezed spin chain to a site $i' + \Delta'$ where Δ' depends on the number of holes between sites

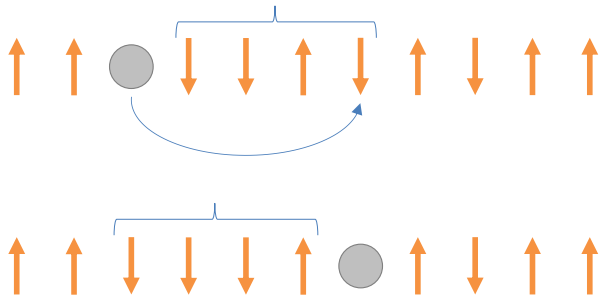

Figure 4.4: Illustration of the effect of a hole (circle) hopping upon the spin configuration (arrows). When a hole hops due to $t_\perp$ (top), it induces a circular permutation of all spins between the initial and final hole sites (bottom). Thus, to each hole hop in the "real" lattice corresponds to a cyclic permutation of spins in the squeezed spin chain.

i and $i+\Delta$ (see Fig 4.4). If no holes are present between sites i and $i+\Delta$, then $\Delta' = \Delta - 1$. If n_h holes are present, then $\Delta' = \Delta - 1 - n_h$. In this jump, the spin previously at site $i'+\Delta'$ is pushed back one site to site $i'+\Delta'-1$ and as well, all the spins between site i' and $i'+\Delta'$ are pushed back one site in what resembles a spin queue model. So we can write

$$e_i^\dagger e_{i+\Delta} S_{i+\Delta,\sigma}^\dagger S_{i,\sigma} = e_i^\dagger e_{i+\Delta} \sum_{n_h=0}^{\Delta-1} P_{i,i+\Delta}(n_h) Q_{i',i'+\Delta'} \tag{4.21}$$

where $P_{i,i+\Delta}(n_h)$ is a projection operator in the subspace of states with n_h holes between sites i and $i+\Delta$ and $Q_{i',i'+\Delta'}$ is the permutation operator between site i' and site $i'+\Delta'$. The operator $P_{i,i+\Delta}(n_h)$ can be written as

$$P_{i,i+\Delta}(n_h) = \sum_{\{b\}} \left[\prod_{j=1}^{n_h} n_{i+b_1} \prod_{j=n_h+1}^{\Delta-1} (1 - n_{i+b_j}) \right], \tag{4.22}$$

where the sum is over all non-equivalent permutations $\{b\}$ of the set $\{1, \ldots, \Delta - 1\}$ and $n_b = e_b^\dagger e_b$. The operator $Q_{i',i'+\Delta'}$ can be written as

$$Q_{i',i'+\Delta'} = \prod_{j=i'}^{i'+\Delta'} \left(2\mathbf{S}_j \cdot \mathbf{S}_{j+1} + \frac{1}{2} \right) \tag{4.23}$$

Using the factorized form and the translation invariance in the spinless chain and in the squeezed spin chain, one can rewrite the Hamiltonian in the $(\{k\}, q)$ subspace as

$$\hat{H}_\perp(\{k\}, q) = \sum_{\substack{i=1 \\ \sigma}}^{L} t_\perp e^{-i(\frac{q}{L} - \pi)\Delta} e_i^\dagger e_{i+\Delta} \sum_{n_h=0}^{\Delta-1} P_{i,i+\Delta}(n_h) \sum_{i'=1}^{N_s} \frac{1}{N} Q_{i',i'+\Delta'} + \text{H.c.} \tag{4.24}$$

and a matrix element of the Hamiltonian in this subspace is given by

$$\langle\{k\};\{\sigma'\},q|\hat{H}_{\perp}|\{k\};\{\sigma\},q\rangle = \sum_{n_h=0}^{\Delta-1}\Bigg[\langle\{k\}|\sum_{\substack{i=1\\ \sigma}}^{L} t_{\perp}e^{-i(\frac{q}{L}-\pi)\Delta}e_i^{\dagger}e_{i+\Delta}P_{i,i+\Delta}(n_h)|\{k\}\rangle \times\langle\{\sigma'\},q|\sum_{i'=1}^{N}\frac{1}{N}Q_{i',i'+\Delta'}|\{\sigma\},q\rangle\Bigg] + \text{H.c.} \quad (4.25)$$

Spin mixing occurs due to the last term in the previous equation and in order to find the eigenvalues of the Hamiltonian, one must diagonalize this term in the q subspace of the squeezed spin chain.

The non-Hermitian operator

$$H_{\text{QSQM}}(\Delta') = \frac{1}{N}\sum_{i'=1}^{N} Q_{i',i'+\Delta'} \quad (4.26)$$

is what we designate by quantum spin queue model (QSQM). The non-Hermiticity of H_{QSQM} reflects the fact that all hole hops are in the same direction for each term in Eq. 4.24. In fact, in order to study the Hamiltonian in Eq. 4.24 using the "particle⊗hole" factorization, one must consider hops in only one direction, find the (complex) eigenvalues of the spin and hole Hamiltonians separately, multiply them, and only then add the result to its complex conjugate (to account for hoppings in both directions). In the QSQM model, particles (spin-up or spin-down) hop a fixed number of sites pushing back the particles between the initial and the final sites. This implies a cyclic permutation of the spin configuration between the initial and final sites, as shown in Fig. 4.4. Note that this operator is not Hermitian but is invariant under translation in the squeezed spin chain. Its eigenvalues will be a sum of phases $\frac{1}{N}\sum_{i=1}^{N} e^{\phi_i}$ in close analogy with the phases obtained in a tight-binding model where hops are allowed in only one direction.

4.4.3 One hole

Let us now study the particular case of a single hole in the strong-coupling helicoidal Hubbard model with an arbitrary number of inverted spins. The case of a single hole has been studied in detail by Nagaoka and others in the strong-coupling Hubbard model in a square lattice [9, 10]. Nagaoka showed that in the $U \to \infty$ limit, the ground state of this model is ferromagnetic. Are the excitations in this case consistent with the behavior of a ferromagnetic system? This is the question we answer in the case of the helicoidal Hubbard model.

Due to the presence of a single hole in the helicoidal lattice, the Hamiltonian is considerably simpler. It can be written as a tensorial product of the tight-binding Hamiltonian of one spinless fermion (the hole) in the helix with L sites and the QSQM Hamiltonian in Eq. 4.26, with $\Delta' = \Delta - 1$. The hole term in Eq. 4.25 can therefore be easily diagonalized and the eigenvalues are

$$t_{\perp}e^{i\Delta(k_h+\pi-q/L)}, \quad (4.27)$$

with $k_h = (2\pi/L)\cdot n_h$ and $n_h = 1,\cdots,L$ and $q = (2\pi/r_\alpha)n_s$ with $n_s = 1,\cdots,r_\alpha$, where r_α is the period of the spin configuration.

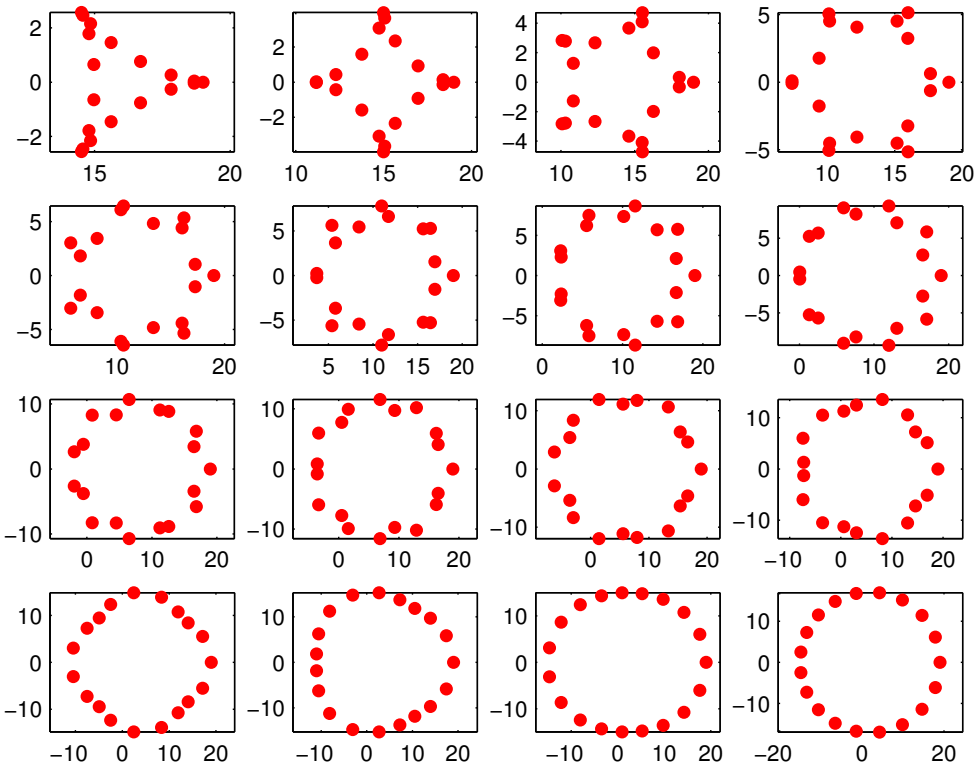

Figure 4.5: Representation, on the complex plane, of the eigenvalues of the QSQM Hamiltonian for a spin queue with $N = 19$ spins, one of which is inverted, given by Eq. 4.28. The first plot is for $\Delta = 3$ and the eigenvalues roughly form a triangle in the complex plane, the second plot is for $\Delta = 4$ (square), and so on, up to $\Delta = 18$.

Considering the subspace of states of the squeezed spin chain with one hole and one up spin (and $N-1$ down spins), a closed form for the eigenvalues is possible to obtain. Due to translation invariance of $H_{\mathrm{QSQM}}(\Delta')$, the states $|\{\uparrow,\downarrow,\cdots,\downarrow\},q\rangle$ constitute an eigenbasis of $H_{\mathrm{QSQM}}(\Delta')$ and the respective eigenvalues in the complex plane are

$$e^{-iq(\Delta-1)} + (\Delta-1)e^{iq} + N - \Delta, \tag{4.28}$$

where $q = 2\pi n/N$ because, with only one inverted spin, the period of the spin configuration is necessarily the number of spins, N. Due to the real term $N-\Delta$, the eigenvalues of one inverted spin are of that order, and since the sum of the other two terms is of order Δ, the phases of the eigenvalues are, at most, of the order of the arctangent of $\Delta/(N-\Delta)$. As N and Δ become larger, these eigenvalues lie on a circumference of center $N-\Delta$ and radius Δ. Several plots of the relation in Eq. 4.28 are shown in Fig. 4.5, for fixed $N = 19$ spins, and Δ ranging from 3 to 18.

Note that the eigenvalues in Eq. 4.28 are for hoppings in one direction only. In order to obtain the eigenvalues of the $t_\perp$ term of the Hamiltonian with hoppings in both positive

and negative directions, one simply needs to multiply the eigenvalues in Eq. 4.27 by those in Eq. 4.28, and add the result to its complex conjugate, yielding

$$2t_\perp \Big\{ (N-\Delta)\cos\Big[\Delta(k_h+\pi-q/L)\Big] + (\Delta-1)\cos\Big[\Delta(k_h+\pi-q/L)+q\Big] + \cos\Big[\Delta(k_h+\pi-q/L)-q(\Delta-1)\Big]\Big\}. \quad (4.29)$$

In the $U \gg t_\parallel \gg t_\perp \gg t_\parallel^2/U$ limit, in the subspace without double occupancies and one inverted spin, this result is the first-order energy correction, due to $t_\perp$, to the eigenvalues in Eq. 4.13. This correction remains the same under a $\Delta \to L - \Delta$ transformation if L is even, and changes its sign if L is odd.

By setting $q = 0$, we recover the list of eigenvalues in Eq. 4.5 because if L is even we can drop the extra π in the gauge transformation in Eq. 2.48. Note that $q = 0$ does not necessarily correspond to a ferromagnetic configuration, but includes the ferromagnetic configurations. Indeed, if one works with hole states with that, for a given number of up and down spins, the spin configuration is a uniform linear combination of all possible permutations of the set of spins, then the spin configuration has momentum $q = 0$, and therefore one can apply circular permutations to the spin configuration without modifying it. Such a spin configuration in the background corresponds to a saturated ferromagnet state (see Chapter 5 for more details).

One of the results of Section 2.4 is that, for a Hubbard ring in the strong-coupling limit with one hole, the ground state occurs for spin momentum $q = 0$ if L is even, and $q = \pi$ if L is odd. This result is also true for a helix with $t_\perp = 0$. However, if we fix $k = \pi$ (the ground state value of k for an infinite system), the $t_\perp$ correction (Eq. 4.29) has a maximum for $q = 0$ and a minimum near $q = \pi$. Note that the eigenstate corresponding to the eigenvalue with the largest real part in any plot in Figs. 4.5-4.8 (i.e. the rightmost dot) is a uniform linear combination of all the permutations of the set of spins, with momentum $q = 0$. The conclusion is that the $t_\perp$ term does not favor a ferromagnetic ground state.

In order to generalize to an arbitrary number of inverted spins, let us consider the QSQM Hamiltonian (Eq. 4.26) with $\Delta' = \Delta - 1$. For each number of inverted spins, N_{inv}, the number of (possibly degenerate) eigenvalues of this Hamiltonian equals the number of possible spin configurations and is given by

$$\binom{N}{N_{\text{inv}}} = \frac{N!}{N_{\text{inv}}!(N-N_{\text{inv}})!}. \quad (4.30)$$

The QSQM can be solved numerically and in the complex plane the eigenvalues roughly form a polygon with Δ sides, as shown in Fig. 4.6, where the blue dots represent the eigenvalues for two inverted spins, and red circles were drawn around the eigenvalues for one inverted spin. The polygon becomes more sharply defined as the number of spins increases. As the number of inverted spins increases, the number of eigenvalues of H_{QSQM} increases as well. It is important to remark that the eigenvalues of H_{QSQM} for a certain N_{inv} are also eigenvalues for any higher number of inverted spins, up to $N_{\text{inv}} = N/2$, rounded down. Consequently, the widest variety of eigenvalues is obtained in the case where one considers the maximum number of inverted spins, and if one finds the eigenvalues of the QSQM Hamiltonian in the this case, one will also have found the eigenvalues for any other number of inverted spins. This is shown in Fig. 4.8, where the transversal hopping range $\Delta = 5$ and a total of $N = 9$ spins was considered, the red dots are the eigenvalues of the QSQM for one inverted spin, and as more inverted spins are

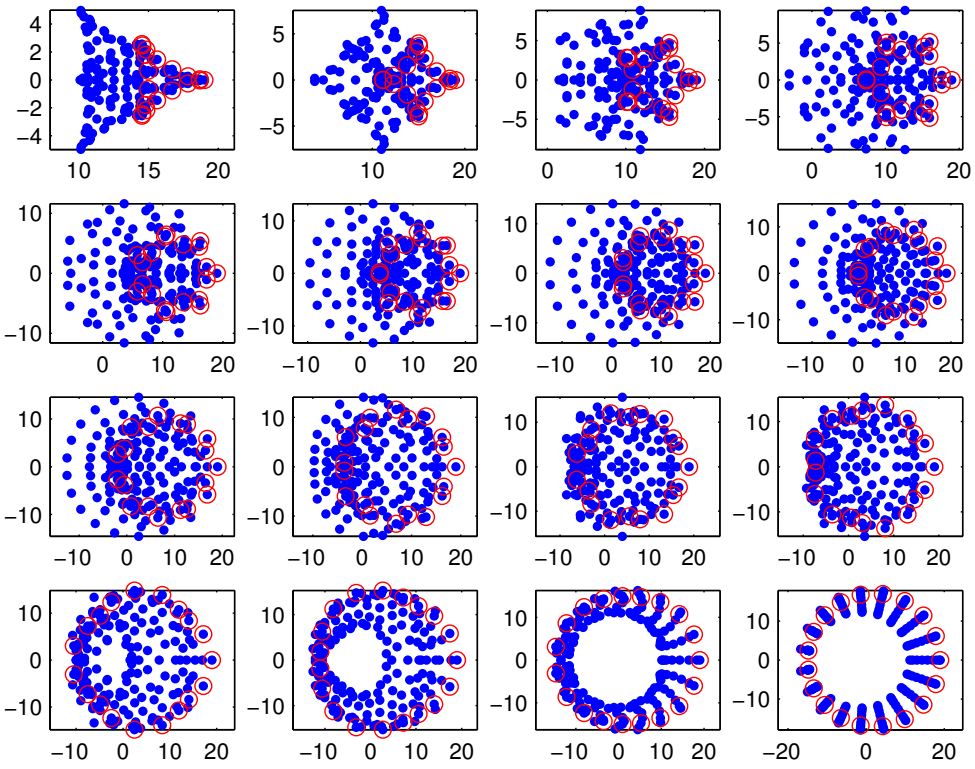

Figure 4.6: Representation, on the complex plane, of the eigenvalues of the QSQM Hamiltonian for a spin queue with $N = 19$ spins, two of which are inverted (blue). The red circles are the eigenvalues for one inverted spin, obtained numerically, and coinciding with those given by the exact result in Eq. 4.28. The eigenvalues for one inverted spin are included among the eigenvalues for two inverted spins. The first plot is for $\Delta = 3$ and the eigenvalues roughly form a triangle in the complex plane, the second plot is for $\Delta = 4$ (square), and so on, up to $\Delta = 18$. The last plot is represented in more detail in Fig. 4.7.

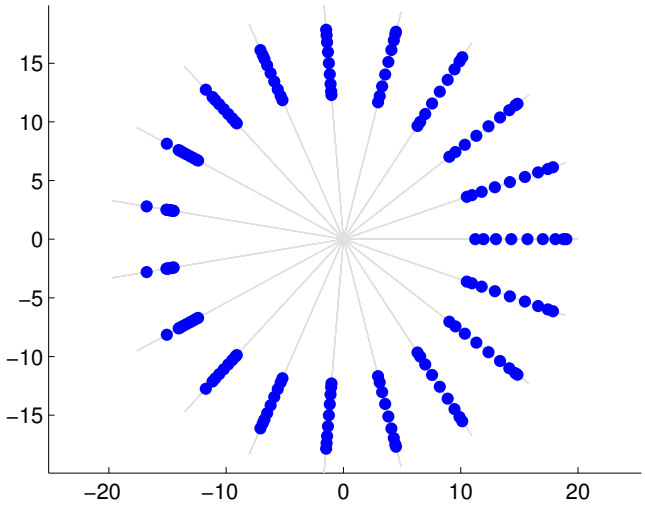

Figure 4.7: Representation, on the complex plane, of the eigenvalues of the QSQM Hamiltonian for a spin queue with $N = 19$ spins, two inverted, and $\Delta = N - 1 = 18$. The orange dots represent the eigenvalues and the grey lines are simply to show that the eigenvalues have well-defined complex phases of the form $(2\pi/N)n$, with $n = 1, \cdots, N$.

considered, more eigenvalues are added to the list, up to four inverted spins, in which case all the plotted eigenvalues occur.

For the specific case $\Delta = N - 1$, with any number of spins, the eigenvalues are uniformly distributed in terms of complex phase, and their phases are of the form $(2\pi/N)n$, with $n = 1, \cdots, N$. In terms of absolute value, the eigenvalues lie between two circumferences (Fig. 4.7). Depending on N_{inv}, the radius and center of these circumferences varies differently with N. For instance, for $N_{\text{inv}} = 2$, the radius of the external circumference is $N - 2.1005$ and the radius of the internal circumference is $N - 7.3134$. The center of each circumference approaches 0.5 and -0.85, respectively, as we approach the thermodynamic limit ($N \to \infty$). For $N_{\text{inv}} = 3$, the radius of the external circumference is $N - 2.3444$ and the radius of the internal circumference is $N - 10.5248$, while the center of each circumference approaches 0.5 and 0.46, as $N \to \infty$.

In conclusion, we introduced the quantum spin queue model (QSQM) to describe the spin dynamics of the Hubbard model on a helix in the strong-coupling limit. This new model is still complex and further studies are required, especially in the case of more than one hole. Nevertheless, the new spin dynamics displayed by this model allows for a better understanding of the 2D Hubbard model with $U = \infty$.

References

[1] E. H. Lieb and F. Y. Wu. "Absence of Mott Transition in an Exact Solution of the Short-Range, One-Band Model in One Dimension". *Phys. Rev. Lett.* 20.25 (1968), pp. 1445–1448.

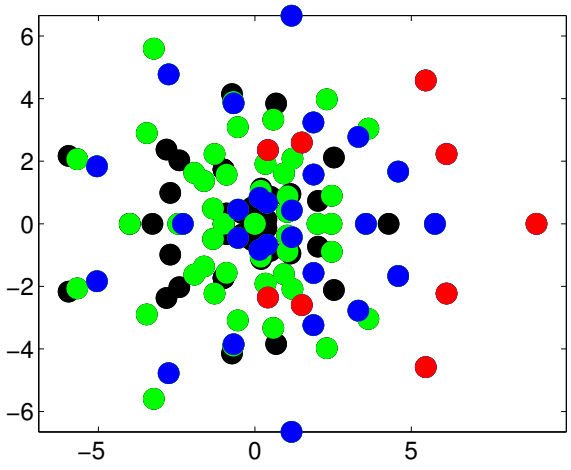

Figure 4.8: Representation, on the complex plane, of the eigenvalues of the QSQM Hamiltonian for a spin queue with $N = 9$ spins and transversal hopping range $\Delta = 5$. The red dots are the eigenvalues for one inverted spin. With two inverted spins, the degeneracy is partially lifted and the blue eigenvalues are added. For three inverted spins, the green eigenvalues are added. Finally, with four inverted spins, all the plotted eigenvalues are possible.

[2] N. D. Mermin and H. Wagner. "Absence of Ferromagnetism or Antiferromagnetism in One- or Two-Dimensional Isotropic Heisenberg Models". *Physical Review Letters* 17.22 (1966), pp. 1133–1136.

[3] W. Wang and S. Xiong. "Possible first order phase transition in the one-dimensional helical Hubbard model". *Physics Letters A* 156.7 (1991), pp. 415–418.

[4] S.-J. Xiong. "Bethe ansatz study of 1+1 dimensional Hubbard model". *ZEITSCHRIFT FUR PHYSIK B CONDENSED MATTER* Volume 89, Number 1 (1992), pp. 29–34.

[5] J. Stockhofe and P. Schmelcher. "Bloch dynamics in lattices with long-range hopping". *Phys. Rev. A* 91 (2015), p. 023606.

[6] J. Stockhofe and P. Schmelcher. "Modulational instability and localized breather modes in the discrete nonlinear Schroedinger equation with helicoidal hopping". *Physica D: Nonlinear Phenomena* 328-329 (2016), pp. 9–20.

[7] D. Reitz and A. Rauschenbeutel. "Nanofiber-based double-helix dipole trap for cold neutral atoms". *Optics Communications* 285.23 (2012). Special Issue: Optical micro/nanofibers: Challenges and Opportunities, pp. 4705–4708.

[8] S. Zdravkovic. "Helicoidal Peyrard-Bishop model of DNA dynamics". *Journal of Nonlinear Mathematical Physica* 18:sup2 (2013), pp. 436–484.

[9] Y. Nagaoka. "Ground state of correlated electrons in a narrow almost half-filled s band". *Solid State Communications* 3 (1965), pp. 409–412.

[10] Y. Nagaoka. "Ferromagnetism in a Narrow, Almost Half-Filled s Band". *Physical Review* 147 (1966), pp. 392–405.

Chapter 5

Origami rules for the construction of localized eigenstates of the Hubbard model in decorated lattices

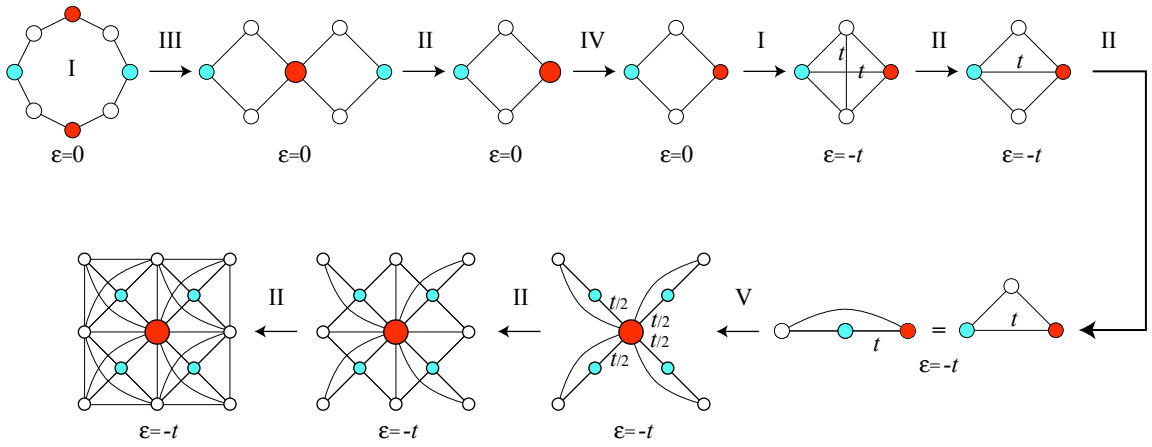

Adapted from:
R. G. Dias and J. D. Gouveia, Origami rules for the construction of localized eigenstates of the Hubbard model in decorated lattices. Scientific Reports 5, Article number: 16852 (2015)
DOI: 10.1038/srep16852

Abstract

We present a method of construction of exact localized many-body eigenstates of the Hubbard model in decorated lattices, both for $U = 0$ and $U \to \infty$. These states are localized in what concerns both hole and particle movement. The starting point of the method is the construction of a plaquette or a set of plaquettes with a higher symmetry than that of the whole lattice. Using a simple set of rules, the tight-binding localized state in such a plaquette can be divided, folded and unfolded to new plaquette geometries. This set of rules is also valid for the construction of a localized state for one hole in the $U \to \infty$ limit of the same plaquette, assuming a spin configuration which is a uniform linear combination of all possible permutations of the set of spins in the plaquette.

5.1 Introduction

The field of itinerant geometrically frustrated electronic systems has attracted considerable interest in the last two decades [1–26]. Much of this interest was related with the study of flat-band ferromagnetism in these systems [15–20]. Flat-band ferromagnetism occurs in decorated lattices of the Mielke's and Tasaki's classes, which display degenerate localized ground states with overlapping probability densities [21–26]. The emerging ferromagnetism can be interpreted as resulting from a generalized Hund's rule [27]. In the case of the lattices which fall into the Lieb's class, the flat bands intercalate itinerant bands [28] and mean-field studies of the Hubbard Hamiltonian in the Lieb lattice indicate that for large U, ferromagnetism is expected except near half-filling where a ferrimagnetic phase appears [29, 30].

These localized states are one-particle eigenstates of the tight-binding Hamiltonians for the decorated lattices and little is known about the many-body eigenstates of an interacting system of fermions in decorated lattices [31] (assuming Hubbard-like interactions), besides the appearance of a ferromagnetic ground state in decorated lattices of the Mielke's and Tasaki's classes [8, 22]. In particular, the interacting ground state of the Hubbard model is not known in the case of lattices of the Lieb's class. Approximate analytic results can be obtained in principle in the weak coupling limit, for example applying a recently proposed procedure that detangles the localized states from the dispersive states [32–34], and introducing the Hubbard interaction as a perturbation of the tight-binding detangled lattice.

In this manuscript, we present a method of construction of exact localized many-body eigenstates of the Hubbard model in decorated lattices of arbitrary dimensions, for $U = 0$ and $U \to \infty$. These states are localized in what concerns hole and particle movement. This method relies in simple arguments which lead to a set of quantum "origami" rules: i) if one plaquette or a set of plaquettes has a higher symmetry than that of the whole lattice, one can find energy eigenstates that have zero probability density at the sites that connect the plaquette or the set of plaquettes to the rest of the lattice (this argument is enough to justify the existence of localized states in the case of two-dimensional decorated lattices of the Lieb's class); ii) given such a localized state in the symmetric plaquette, one can fold the plaquette, either at the probability density nodes or at other equivalent sites (adjusting the probability density at those sites and the hopping constants that involve those sites), therefore lowering the symmetry of the plaquette; iii) the energy of the localized state can be lowered by adding hopping terms between sites with the same localized state phase (if the hopping constant is negative) or hopping terms between sites with opposite phases (if the hopping constant is positive). Hopping terms between nodes of the localized state may also be added, but do not change the energy of the localized state. The hopping terms added must preserve the symmetry of the localized state. These two arguments justify localized states in decorated lattices of the Mielke's and Tasaki's classes. Furthermore, the spin degree of freedom of the $U = 0$ Hubbard Hamiltonian may be interpreted as a sublattice index and localized states can also be created using these origami rules involving the two (up and down spin) sublattices. Such localized states arise for instance as edge states in 1D tight-binding descriptions of topological insulators [35–37].

The remaining part of this paper is organized in the following way. First, we review the construction of one-particle localized eigenstates of the tight-binding decorated lattices of the Lieb's class. We then generalize this construction to more complex lattices using a symmetry argument and introducing the set of origami rules. Next, we show how to extend these rules to the case of the $U \to \infty$ limit of the Hubbard model. Finally we conclude.

The Hubbard Hamiltonian in a decorated lattice can be written as

$$H = \sum_{\langle ij\rangle,\sigma} t_{ij} c^{\dagger}_{i\sigma} c_{j\sigma} + U \sum_{i} n_{i\uparrow} n_{i\downarrow}, \tag{5.1}$$

where the creation (annihilation) of an electron at site i with spin σ is denoted by $c^{\dagger}_{i\sigma}$ ($c_{i\sigma}$) with $n_{i\sigma}$ being the number operator $n_{i\sigma} = c^{\dagger}_{i\sigma} c_{i\sigma}$ and $n_i = n_{i\uparrow} + n_{i\downarrow}$. The sum over $\langle ij\rangle$ is the sum over all pairs of sites with a finite hopping probability between them and this a different sum for each decorated lattice. The hopping constants are assumed to be equal, $t_{ij} = t$, unless stated otherwise. When $t = 0$, all states with the same number N_d of doubly occupied sites are degenerate. In this paper, we assume $N_d = 0$. The Hubbard model in the limit $U \to \infty$ is also designated as Harris-Lange model [38]. In this limit, using the identity $c_{i\sigma} = c_{i\sigma}[(1-n_{i\sigma})+n_{i\sigma}]$, the Hubbard model can be rewritten as

$$\hat{H} = \sum_{\langle ij\rangle,\sigma} t_{ij}(1-n_{i\bar{\sigma}}) c^{\dagger}_{i\sigma} c_{j\sigma} (1-n_{j\bar{\sigma}}) \tag{5.2}$$

with $\bar{\sigma} = -\sigma$. An important point about the strong coupling limit is that the Hamiltonian eigenfunctions, in the case of a Hubbard ring, can be written as a tensorial product of the eigenfunctions of a tight-binding model of independent spinless fermions (holes) in the ring with L sites and the eigenfunctions of an Heisenberg model (with exchange constant $J = t^2/U$) in a reduced chain [39–42].

5.2 Origami rules for tight-binding Hamiltonians

Let us first discuss the $U = 0$ case of the Hubbard model in decorated lattices. Flat bands in the one-particle tight-binding energy dispersion of geometrically frustrated lattices reflect the existence of degenerate localized eigenstates which are translated versions of the same state $|\psi_{\rm loc}\rangle$. The probability density associated with one of these localized states is non-zero only in a small lattice region. In the particular case of decorated lattices of the Lieb's class, the localized states can be viewed as one-dimensional standing waves in tight-binding rings, associated with paths in the 2D lattice which include one or two plaquettes [43]. For zero flux, all one-particle energy levels of a tight-binding ring (with even number of sites) are doubly degenerate (except for $k = 0$ and $k = \pi$) and the respective eigenstates have opposite momenta. Adding or subtracting the states of opposite momenta, one obtains a standing wave with a number of nodes that depends on k. If these nodes coincide with the sites at the vertices of a plaquette of a decorated lattice, the electron becomes trapped inside the plaquette. Therefore, flat band eigenstates of decorated lattices of the Lieb's class are constructed from standing waves such that the nodes coincide with sites at the vertices. Note that these localized states overlap in real space, that is, they constitute a basis of the subspace of localized states but not an orthogonal basis.

The previous argument for lattices for the Lieb's class can be generalized to decorated lattices of the Mielke's and Tasaki's classes and other decorated lattices using a symmetry argument. First, let us discuss the case of the Lieb lattice (see Fig. 5.1). The tight-binding Hamiltonian of one plaquette of the Lieb lattice has the symmetry of a ring of 8 sites, that is, the plaquette Hamiltonian is invariant in a $2\pi/8$ rotation of the set of site indices (or equivalently in a circular permutation of the set of site indices). We emphasize that this

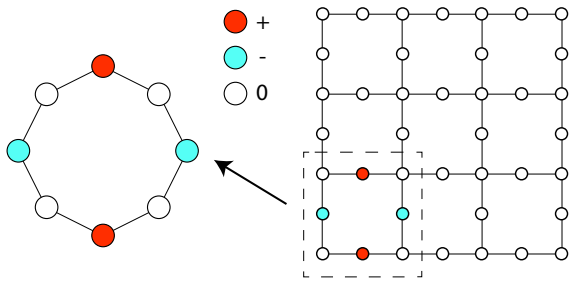

Figure 5.1: The symmetry of the tight-binding Hamiltonian for the Lieb plaquette is the same as that of the tight-binding ring and larger than that of the Lieb lattice. The distance between adjacent sites is assumed to be $a = 1$. All hopping constants are equal.

rotation should not be confused with a $2\pi/8$ rotation in real space (the plaquette is not invariant in such a rotation). However, the rotation of $2\pi/4$ in the set of sites indices can be interpreted as a $2\pi/4$ rotation in real space. In the ring of 8 sites, one has outer sites (that are connected to the rest of the lattice) and inner sites (with connections only to sites of the plaquette). In the case of Fig. 5.1, the inner sites are indicated by the filled circles and the outer sites are given by the empty circles. The generator of this rotation symmetry is the equivalent of the angular momentum in the ring (note that in a 2D lattice, the direction of the angular momentum is always perpendicular to the lattice and therefore equal to $m\hbar$, where m can be interpreted as the m in the ring momentum $k = m \cdot 2\pi/N$) and one can construct an eigenbasis of the Hamiltonian which is simultaneously an eigenbasis of the angular momentum. The time reversal symmetry of the Hamiltonian implies that each eigenstate of the plaquette tight-binding Hamiltonian is degenerate with the respective state obtained in a time reversal and these states have opposite angular momenta (this is equivalent to stating that ring eigenstates with momenta k and $-k$ are degenerate). These two states can be added or subtracted, generating the equivalent of the standing waves in the ring, that is, states with zero probability density at certain sites of the cluster. If the angular momentum is $\hbar N/4$, where N is the number of sites of the ring, one has zero probability density at the inner sites or at the outer sites of the Lieb plaquette (nodes are separated by $\lambda/2 = 2$). The latter will be a localized eigenstate not only of the Lieb plaquette but also of the tight-binding Hamiltonian of the full lattice. Note that this description is valid for any plaquettes which have the same rotation symmetry as the ring. For example, one could add additional sites at the center of the Lieb plaquette and the rotation symmetry would remain, as shown in Fig. 5.2 (in all Figures, the relative size of the circles that represent lattice sites corresponds to the relative value of the wavefunction amplitudes on the sites).

Thus, our first rule is that localized states can be constructed if a plaquette (or a set of adjacent plaquettes) has a larger symmetry than the lattice, so that the Hamiltonian has two degenerate eigenstates (which are simultaneously eigenstates of the generators of the symmetry of the lattice) which have the same wavefunction values at the outer sites of the plaquette (see Fig. 5.3a). This rule is enough to explain the existence of localized states in lattices of the Lieb's class. More complex lattices with localized states can be constructed by adding sites or hopping bonds that do not lower the symmetry of the plaquette. These additional hoppings can be divided into two sets: i) the set of hoppings from or to sites with probability density nodes (these hoppings do not modify the energy of the localized state); ii) the set of hoppings

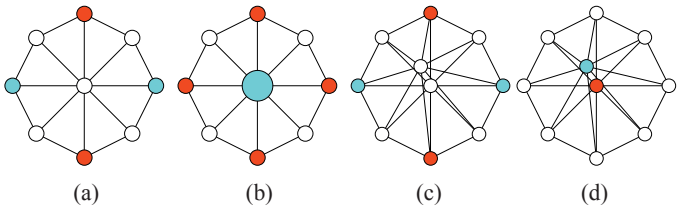

Figure 5.2: In these simple variations that retain the symmetry of the Lieb plaquette, two localized states exist corresponding to two possible choices of angular momentum. The size of the circles that represent lattice sites indicates the relative value of the wavefunction amplitudes. There is an analogy of these states with atomic orbitals.

between sites with finite density probability (these hoppings lower or raise the energy of the localized state).

A second rule for the construction of lattices with localized states is the following. The existence of sites where a localized state has probability density nodes does not affect the energy of the state and these sites can be dropped, duplicated (as well as the respective hopping bonds), or simply added (introducing appropriate hoppings with neighboring sites) and the localized state remains an eigenstate of the modified tight-binding model associated with the new plaquette geometry (see Fig. 5.3b). Furthermore, if one can draw an axis through the plaquette that crosses only nodes, then dropping these nodes one divides the localized state into two eigenstates of the tight-binding Hamiltonians associated with the parts of the plaquette. Bonds between nodes can also be dropped, added or duplicated. This rule justifies the localized states in the lattice of Fig. 5.4a. In fact, sites A and B in Fig. 5.4a can be seen as a duplication of the equivalent site of the ring of Fig. 5.1, with the addition of a hopping bond between the duplicated nodes.

The third rule consists of the following: localized states can be folded (adjusting the amplitude at the crossing and the respective hoppings) along an axis that crosses the plaquette through sites that have the same wavefunction values (see Fig. 5.3c); if the folding is along an axis that crosses nodes, no adjustment of hopping constants or wavefunctions amplitudes is needed.

The fourth rule is that the amplitude at a given site of a localized state with zero energy can be renormalized without changing the energy of the state, if the hopping constants to that site are renormalized as well (see Fig. 5.3d).

The fifth rule describes the unfolding of a plaquette around a given site (see Fig. 5.3e). Multiple rotated copies of the original plaquette can be added around a site, provided that the amplitude of the wavefunction on this site is adjusted, as well as the hopping constants around this site.

This set of rules justifies the existence of localized states in the Mielke and Tasaki lattices of Fig. 5.4. In Fig. 5.5, we exemplify the application of this set of rules starting from the localized state of the Lieb plaquette and ending at the localized state of the Tasaki lattice.

We emphasize that these rules can be applied to construct localized states in systems of arbitrary dimension, from 0D (a molecule) to 3D crystals, since the tight-binding bonds of Fig. 5.3 may not be coplanar and the unfolding axis can have an arbitrary direction. Furthermore, the spin degree of freedom of a tight-binding model may be interpreted as a sublattice index, and spin flipping terms can be interpreted as hopping terms between such

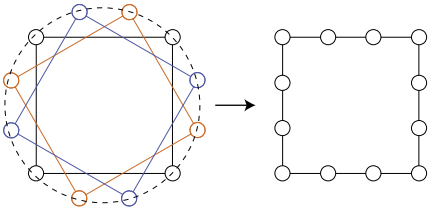

(a) Rule I: symmetry.

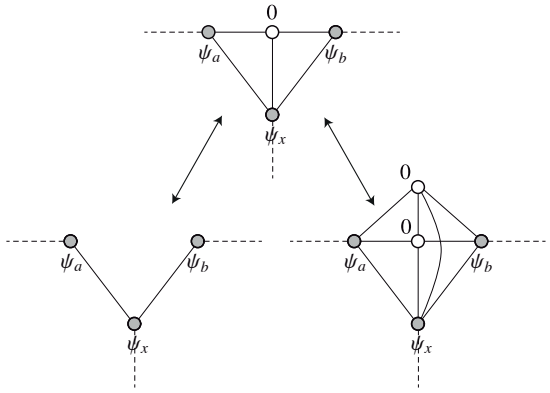

(b) Rule II: add/remove nodes.

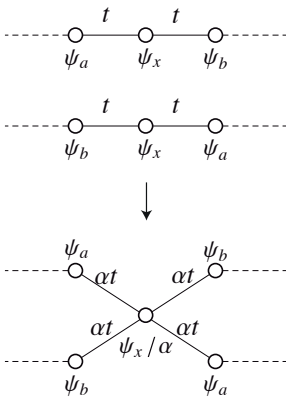

(c) Rule III: folding ($\alpha = 1/\sqrt{2}$).

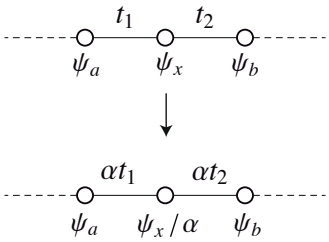

(d) Rule IV: renormalization (E = 0).

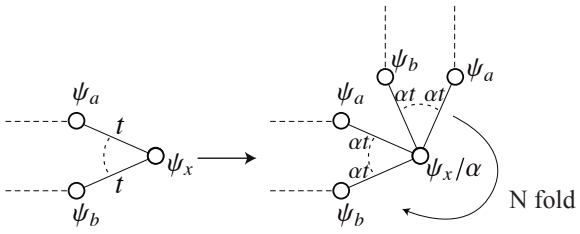

(e) Rule V: unfolding ($\alpha = 1/\sqrt{N}$).

Figure 5.3: Set of origami rules for the construction of localized states in decorated lattices. The values of α can be obtained from simple tight-binding calculations, imposing the condition that the state is still an eigenstate after applying the rule.

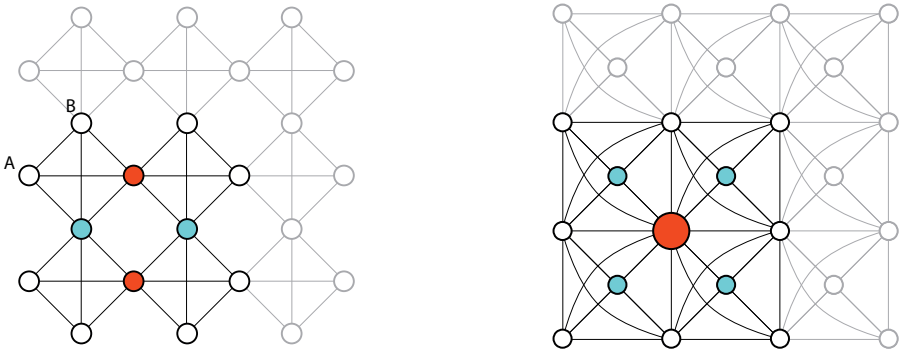

Figure 5.4: Localized states in the (a) Mielke lattice and (b) Tasaki lattice. All hopping constants are the same ($t_{ij} = t$), except those associated with curvy lines ($t_{ij} = t/2$). Note that the tight-binding Hamiltonian for the Mielke plaquette is symmetric in the exchange of sites A and B, but the full tight-binding Hamiltonian is not. This implies the Hamiltonian eigenfunctions must have the same amplitude value (or opposite values) at sites A and B. In the case of the localized states, the value must be the same and the sites A and B are effectively one site.

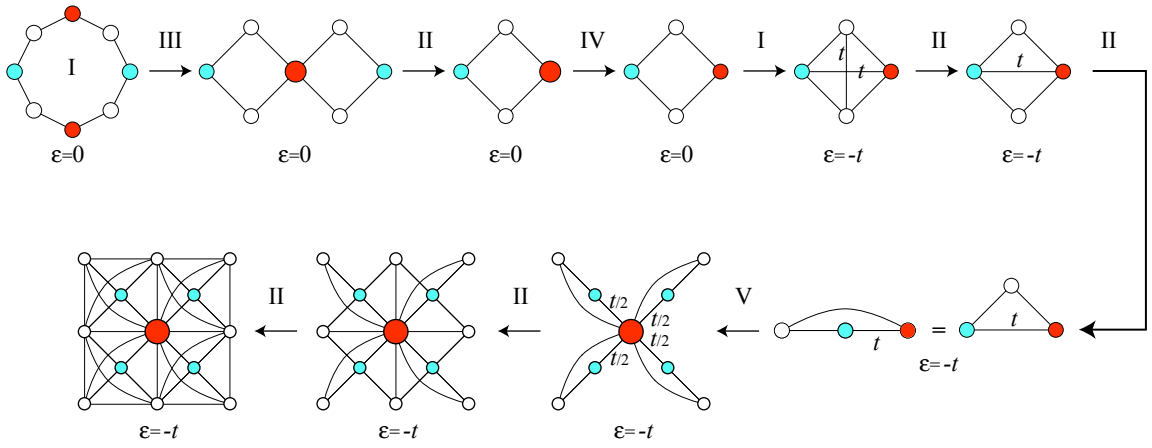

Figure 5.5: Application of the rules presented in the text, starting from the localized state in the Lieb plaquette and ending at the localized state in the Tasaki lattice. Note that the energy of the localized state in the Tasaki lattice is determined by the central hoppings between sites with finite probability density.

sublattices. Localized states can also be created using the above origami rules involving the two (up and down spin) sublattices and examples of such localized states are the edge states in 1D models of topological insulators with spin flipping terms (see for example section 3.3. of Ref. [35]).

Another context where this set of rules applies is that of one-magnon localized states in frustrated quantum Heisenberg antiferromagnets. In these systems, these states generate peculiar behavior such as magnetization plateaus around the saturation field [15, 44].

5.3 Origami rules in the $U \to \infty$ limit of the Hubbard model

Let us now discuss how much of this method can be applied in the $U \to \infty$ limit of the Hubbard model. We start by considering the Lieb lattice and then we generalize our conclusions to more complex decorated lattices. As discussed previously, the Lieb plaquette is a 8-site tight-binding ring. The eigenfunctions of the Hubbard ring in the strong coupling limit have been obtained by several authors [39–42]. Here, we present a simple derivation of the one-hole case when no doubly occupied sites are present. Our approach follows closely the method and notation used by Dias and Peres [41, 42].

Let us consider a state of the $U \to \infty$ Hubbard ring with N sites and a single hole at site i, given by

$$|i, \{\sigma\}\rangle = \prod_{j=1}^{N-1} c^{\dagger}_{b_j \sigma_j} |0\rangle \tag{5.3}$$

where $\{\sigma\} = \{\sigma_1, \ldots, \sigma_{N-1}\}$ is the set of particle spins in the lattice and $b_j = j$ if $j < i$ and $b_j = j + 1$ if $j \geq i$. Now we introduce an operator $\hat{Q}$ such that

$$\hat{Q}|i, \sigma_1, \ldots, \sigma_{N-1}\rangle = |i, \sigma_{N-1}, \sigma_1, \ldots, \sigma_{N-2}\rangle \tag{5.4}$$

that is, it does a circular permutation of the spin configuration. When the Hamiltonian given by Eq. 5.2 acts on such a state it simply exchanges the empty site with a spin with amplitude t without changing the spin sequence $\{\sigma\}$, except when the hole is at sites 1 and L. If the hole hops from site 1 to site N, a new spin sequence is obtained which is the circular permutation of the previous one, $\{\sigma'\} = \hat{Q}\{\sigma\}$. Therefore the hole motion mixes the spin configurations with those spin configurations which are circular permutations of the initial one.

Given a configuration of spins $\{\sigma\}$, the eigenstates of the Hamiltonian will be found in the subspace spanned by $\hat{Q}^n\{\sigma\}$, $n = 0, \cdots, r_\alpha - 1$, where r_α is the period of the spin configuration. The α index labels the different (not obtainable from any other by cyclic permutations) spin configurations with period r_α. Let us build states invariant in a circular permutation

$$|i; \alpha, q_s\rangle = \frac{1}{\sqrt{r_\alpha}} \sum_{m=0}^{r_\alpha - 1} e^{i q_s m} \hat{Q}^m |i, \sigma_1, \ldots, \sigma_{N-1}\rangle, \tag{5.5}$$

where $q_s = n_s\,(2\pi/r_\alpha)$ with $n_s = 0, \cdots, r_\alpha - 1$, that is, a state such that

$$\hat{Q}|i; \alpha, q_s\rangle = e^{-i q_s} |i; \alpha, q_s\rangle. \tag{5.6}$$

Since the hoppings across the boundary do a cyclic permutation, the Hamiltonian in the subspace of states $|i; \alpha, q_s\rangle$ becomes

$$H = -t \sum_{i \neq N} |i+1\rangle\langle i| - t \sum_{i \neq 1} |i-1\rangle\langle i| - t(-1)^{N-2} \left(e^{-i q_s} |1\rangle\langle N| + H.c. \right)$$

where we have simplified the notation by dropping the spin configuration index α and the spin momentum q_s. This is a simple tight-binding model of one spinless fermion (hole) with twisted boundary conditions and the respective eigenstates are Bloch states for the movement of the hole. A gauge transformation $|n\rangle \to |n\rangle e^{i(q_s/N-\pi)n}$ makes the previous model translation invariant and one has

$$E(k) = 2t\cos\left(k - \frac{q_s}{N}\right), \tag{5.7}$$

with $k = (2\pi/N)n$, $n = 0, \ldots, N-1$.

In the case of this paper, the one-hole solution in the $U \to \infty$ limit of the Hubbard ring is sufficient, but note that this solution can be generalised to the case of N_h holes in the Hubbard ring (in the $t^2/U \ll 1$ limit) with the Hubbard ring eigenfunctions being written as a tensor product of the eigenfunctions of a tight-binding model of independent spinless fermions (holes) in the ring with L sites and the eigenfunctions of an Heisenberg model (with exchange constant $J = t^2/U$) in a reduced chain [39–42].

So in the case of one hole, the energy dispersion given by Eq. 5.7 is that of one spinless fermion in a tight-binding ring threaded by a fictitious magnetic flux, $\phi = q_s$, generated by the spin configurations in the reduced Heisenberg chain (where q_s is the spin momentum of the chain). Therefore, if the spin momentum is zero (note that non-zero spin momentum destroys the time reversal symmetry of the tight-binding model of spinless fermions), one can construct a standing wave for one hole moving in the Hubbard ring with arbitrary spin configuration as in the case of one particle in a tight-binding ring shown in Fig. 5.1. Since the Lieb plaquette is a ring with 8 sites, this standing wave for one hole can be created in this plaquette with nodes of the hole probability density at the outer sites as shown in Fig. 5.6 (this standing wave is obtained combining the degenerate states with $k = \pi/2$ and $k = -\pi/2$). Since the hole is trapped in a plaquette (indicated by the dashed square in Fig. 5.6), the spin configuration in the rest of the lattice is arbitrary, in the limit of the Harris-Lange model. We emphasize that the spin momentum mentioned above is that of the spin configuration in the Lieb plaquette (a ring of 8 sites) and not that of the spin configuration of the total lattice (we designate the set of sites of the Lieb lattice as Λ). More precisely, the localized hole state in the Lieb lattice will be the antisymmetric tensor product of the hole state in the Lieb plaquette and the state of the spins in the rest of the lattice (see Fig. 5.6). As usual, writing the full state using creation operators assures the proper antisymmetrization of the hole localized state in the Lieb lattice and if the hole is localized in a Lieb plaquette that we label as i_p, this state has the form:

$$|i_p; \{k = \pm\pi/2, +; \alpha, q_s = 0\}; \{\sigma\}_{\Lambda'}\rangle = \hat{\Psi}_{i_p} \prod_{j\in\Lambda'} c^\dagger_{j\sigma_j}|0\rangle \tag{5.8}$$

with

$$\hat{\Psi}_{i_p} = \underbrace{\left[\sum_{l=1}^{N}\left(\frac{e^{i\frac{\pi}{2}l} + e^{-i\frac{\pi}{2}l}}{\sqrt{2N}}\right)e^{i\pi l}\frac{1}{\sqrt{r_\alpha}}\sum_{m=0}^{r_\alpha-1}\hat{Q}^m_{i_p}\prod_{j=1}^{N-1}c^\dagger_{b_j\sigma_j}\right]}_{\text{hole localized state in the Lieb plaquette } i_p}, \tag{5.9}$$

and where $N = 8$ is the number of sites in the Lieb plaquette (which are labelled clockwise from 1 to N, starting at an outer site), Λ' is the set of sites of the Lieb lattice, excluding those of the plaquette where the hole is trapped (see dashed square in Fig. 5.6), i_p labels the plaquette in the Lieb lattice where the localized hole is, $\{\sigma\}_{\Lambda'}$ is the spin configuration at the sites in Λ', l indicates the position of the hole in the Lieb plaquette i_p and with $b_j = j$

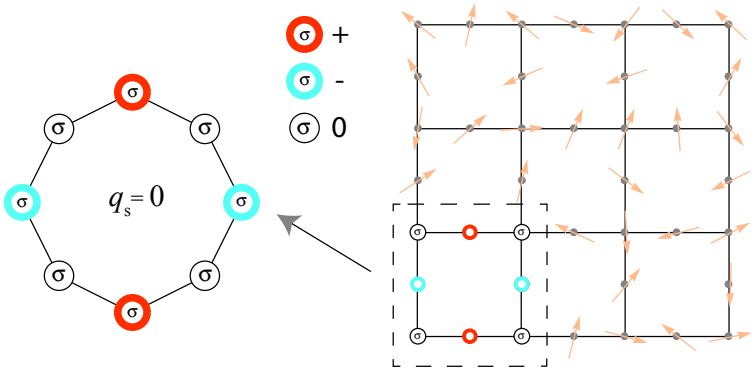

Figure 5.6: One hole can be trapped in a plaquette of the half-filled interacting Lieb lattice, in the $U \to \infty$ limit of the Hubbard model, if the spin momentum of the spin configuration in that plaquette is zero. Since the hole probability density is zero at the outer sites of the plaquette, this plaquette effectively decouples from the rest of the lattice, where the spin configuration is arbitrary. The red and blue sites indicate finite amplitude of the hole wavefunction (positive and negative, respectively).

---

if $j < l$ and $b_j = j + 1$ if $j \geq l$. The operator $\hat{Q}_{i_p}$ does a circular permutation of the spin configuration in a single Lieb plaquette (labelled i_p). The standing wave is created summing the degenerate states (in the Lieb plaquette) with $k = \pi/2$ and $k = -\pi/2$ and this is indicated by $\{k = \pm\pi/2, +\}$ in Eq. 5.8.

This construction can be generalized to an arbitrary number of localized holes, each one of them in a different plaquette, as long as the plaquettes are not contiguous (plaquettes which do not have common sites),

$$|\{i_p\}; \{k = \pm\pi/2, +; \alpha, q_s = 0\}; \{\sigma\}_{\Lambda'}\rangle = \prod_{i_p} \hat{\Psi}_{i_p} \prod_{j \in \Lambda'} c^{\dagger}_{j\sigma_j} |0\rangle \tag{5.10}$$

with Λ' being the set of sites of the Lieb lattice remaining after dropping the sites associated with the plaquettes $\{i_p\}$. The sites in each of these plaquettes are labelled using two indices, (i_p, l) with $l = 1, \cdots, N$, so that the hole localized states in each of these plaquettes have still the form given by Eq. 5.9 with $b_j \to (i_p, b_j)$.

Does this apply to more complex plaquettes that share the rotation symmetry of the Lieb plaquette? Taking the example shown in Fig. 5.2a, one sees that in the non-interacting case, a localized state is present where the particle is confined to a 1D path. This leads one to suggest that an equivalent localized state can be constructed for the hole moving in the spin background, if we impose a $q_s = 0$ spin momentum for the spins configuration in the 1D path (note that we are using the same definition of spin momentum as above, since the 1D path in Fig. 5.2a correspond to that of the Lieb plaquette). However one should note that in Fig. 5.2a, despite the electron probability density being finite only in the outer ring, when the electron is at the outer ring, it still hops to the center site, but summing over all the hopping possibilities from the sites at the outer ring to the center site, the result will be zero (destructive interference). In the case of the hole moving in the spin background, the hops of the hole from sites at the outer ring to the center site mix the spins at the outer ring and at the center. In order for one to have destructive interference at the center, the spin configuration must be a uniform linear

combination of all possible permutations of the set of spins (given the number of up spins and down spins). The reason is the following: when an electron in the localized state of Fig. 5.2a hops from a site of the outer ring to the center site, it interferes destructively with the contributions of hoppings from the other sites of the outer ring. In the case of the hole, one has the different spin backgrounds and the hops of the hole from the outer ring to the center should not apparently interfere destructively. However, if one works with hole states such that, for a given number of up and down spins in the plaquette, the spin configuration is a uniform linear combination of all possible permutations of the set of spins, then: i) the spin configuration in the outer ring has $q_s = 0$ spin momentum, that is, one can apply circular permutations to the spin configuration in the outer ring but this will not modify the spin configuration; ii) a hole jump from a site A or B of the outer ring to the central site will generate the same final state, independently of the initial site being A or B. Therefore, we have the same localized state for one hole in the $U \to \infty$ limit of the Hubbard model as for one electron when $U = 0$. Or better, the spin configuration in the background will be equivalent to a saturated ferromagnetic configuration in what concerns the movement of the hole, since the spin configuration will not change and will not generate additional phase factors. This state can be expressed as $(S^-_{\rm plaq})^n \, |\psi_{\rm FM}\rangle$, where $S^-_{\rm plaq}$ is the spin-lowering operator defined within the plaquette, n is the number of down spins and $|\psi_{\rm FM}\rangle$ is the plaquette ferromagnetic state with one hole, which can be written as $\sum_j \psi_j c_{j,\uparrow} \prod_{i=1}^{N} c^\dagger_{i,\uparrow} \, |0\rangle$, where ψ_j is the hole wavefunction amplitude. Note that this argument is also valid if the localized state occupies several plaquettes.

Let us explain in more detail the last argument using the example of the Mielke lattice in Fig. 5.7a. The localized hole will have finite probability in the same compact set of plaquettes as the compact localized state of the tight-binding limit (see Fig. 5.4a). If we number the sites in this compact set of plaquettes as shown in Fig. 5.7b, one can use a mathematical formalism similar to the one used above in the case of the interacting Lieb lattice. When one has a hole at site 6 and the hole hops to site 9, this hopping induces a modification of the spin configuration from $\{\sigma\} = \{\sigma_1, \ldots, \sigma_{11}\}$ to $\{\sigma'\} = \{\sigma_1, \sigma_2, \sigma_3, \sigma_4, \sigma_5, \sigma_8, \sigma_6, \sigma_7, \sigma_9, \sigma_{10}, \sigma_{11}\}$ (see Fig. 5.7b). Let us introduce the operator $\hat{P}_{\rm all}$ that sums over all different permutations $\{\sigma'\}$ of the spin configuration $\{\sigma\}$ (note that a permutation of two up-spins does not lead to a different spin configuration),

$$\hat{P}_{\rm all}|i, \{\sigma\}\rangle = \frac{1}{\sqrt{N_{\{\sigma\}}}} \sum_{\{\sigma'\}} |i, \{\sigma'\}\rangle, \tag{5.11}$$

where $N_{\{\sigma\}}$ is the number of different permutations of the spin configuration $\{\sigma\}$. The construction of a state involving the sum over spin permutations resembles the construction of the ground state in the Brandt-Giesekus model[45, 46], although in this model only a particular filling is considered. Starting from the state $\hat{P}_{\rm all}|6, \{\sigma\}\rangle$, the hopping of the hole from site 6 to site 9 leads to $\hat{P}_{\rm all}|9, \{\sigma\}\rangle$, that is, the spin configuration does not change (note that $\{\sigma'\}$ is a permutation of $\{\sigma\}$, so the sum of all permutations of $\{\sigma'\}$ is equal to the sum of all permutations of $\{\sigma\}$). Another way to state this is the following: any operation of transposition of two spins commutes with $\hat{P}_{\rm all}$, and therefore any permutation of the spin configuration $\{\sigma\}$ commutes with $\hat{P}_{\rm all}$. Therefore, if $\hat{P}_{\{\sigma\}\to\{\sigma'\}}$ is the permutation of $\{\sigma\}$ into $\{\sigma'\}$, then $\hat{P}_{\{\sigma\}\to\{\sigma'\}}\hat{P}_{\rm all} = \hat{P}_{\rm all}\hat{P}_{\{\sigma\}\to\{\sigma'\}} = \hat{P}_{\rm all}$. Note that an extra minus sign could appear if the hopping of the hole involves an odd number of exchanges of creation operators, but this extra sign is the same as in the case of the same hopping of the hole in a saturated ferromagnetic background (assuming the same numbering of sites). Since it is obvious that we can create a hole localized state in a decorated lattice with a saturated ferromagnetic background (one

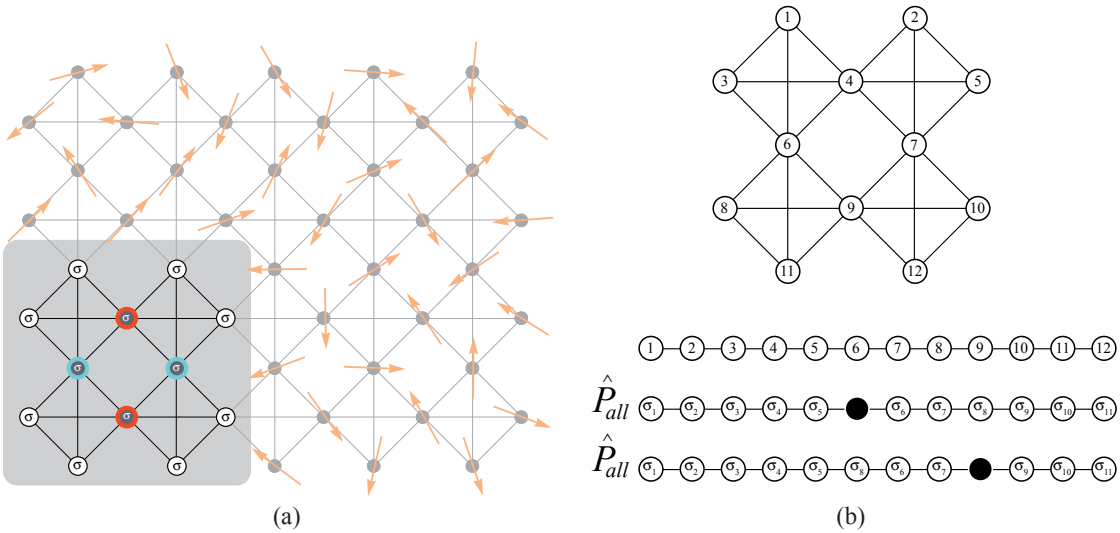

Figure 5.7: (a) The construction of a localized state for one hole in the $U \to \infty$ limit in an arbitrary decorated lattice is possible (if one-particle localized states exist), assuming a spin configuration which is a uniform linear combination of all possible permutations of the set of spins in the plaquette or set of plaquettes associated with the compact one-particle localized states (gray region). (b) Top: Numbering of sites in the set of plaquettes where the hole localized state has finite probability density; bottom: spin configuration using a chain representation of the set of plaquettes, in the case of one hole at site 6 and one hole at site 9, after a $6 \to 9$ hopping.

can do a particle-hole transformation and the hole localized state becomes a particle localized state), this implies that a hole localized state can be created in the set of plaquettes shown in the gray region of Fig. 5.7a. The spin configuration in the rest of the lattice is arbitrary.

This construction of a localized state is valid for any decorated lattice where a localized state of one tight-binding electron exists. In the case of the states given by Eq. 10, the localized holes occupy plaquettes with no common sites (which limits the maximum number of localized holes to a fourth of the number of plaquettes, in the case of the Lieb lattice). Note however that in the case of the plaquette with ferromagnetic background (or equivalently plaquette states with a spin configuration which is a uniform linear combination of all possible permutations of the plaquette set of spins), the maximum number of localized holes is higher since the ferromagnetic configuration can be shared by plaquettes that have common outer sites (sites with nodes of the hole wavefunction) but no common inner sites (in the Lieb lattice, this would lead to a maximum of localized holes equal to half the number of plaquettes). This has been confirmed numerically, diagonalizing exactly the Harris-Lange model in a set of few plaquettes for several choices of decorated lattices.

Note that besides the localized state degeneracy associated with the choice of the lattice plaquette where the localized state sits, there is a huge degeneracy associated with the possible choices of number of up spins (or down spins) in the plaquette and in the rest of the lattice. This degeneracy is lifted by the Heisenberg corrections of order t^2/U, as in the Hubbard ring [39–42].

Another important remark is that while the one-electron localized states of the Mielke and

Tasaki lattices are the ground states of the respective tight-binding Hamiltonians, in the case of the $U \to \infty$ Hubbard model, the one-hole localized state is not the ground state, for the choice of relative hopping constants of Fig. 5.4. However, since the exact form of the hole probability density is known as well as the hole wavefunction phase (as in the case of the one-electron localized state), it is possible to tune the geometry, hopping constants and interactions in order to lower the energy of the hole localized state relatively to the other states, so that the energy of the localized state approaches the energy of the ground state.

5.4 Conclusion

In conclusion, we have presented a simple set of rules for the construction of localized states of the Hubbard model in nearly arbitrary decorated geometries, in the tight-binding limit ($U = 0$), and in the strong-coupling limit ($U \to \infty$). The first step in this method is the choice of a plaquette or a set of plaquettes with a higher symmetry than that of the whole lattice. In this plaquette, one has a localized state of the tight-binding Hamiltonian of the full lattice (this state has probability density nodes at the sites shared between the plaquette and the rest of the lattice). Using a simple set of rules, the tight-binding localized state in such plaquette can be divided, folded or unfolded to new plaquette geometries. We have shown that this set of rules can also be applied in the $U \to \infty$ limit of the Hubbard model, for the construction of localized states of one hole in the plaquette, assuming a spin configuration which is a uniform linear combination of all possible permutations of the set of spins in the plaquette. Note that in every other plaquette, one may place a localized hole, so localized hole states exist for hole doping between zero and a value of the order of $1/N_{\mathrm{loc}}$ (the value depends on the lattice geometry), where N_{loc} is the number of atomic sites of the set of plaquettes where one hole is localized.

This paper presents a unifying picture of construction of localized states, in tight-binding systems of arbitrary dimension (from 0D to 3D), arbitrary geometry (including Mielke's and Tasaki's 2D geometries), without and with interactions ($U = 0$ or $U = \infty$, extending in the latter case the filling intervals where localized states are known to occur). The existence of localized states due to spin flipping terms in tight-binding descriptions of topological models, or the existence of one-magnon localized states in frustrated Heisenberg antiferromagnets, are two other contexts included in this unifying picture.

References

[1] R. R. Montenegro-Filho and M. D. Coutinho-Filho. "Doped AB_2 Hubbard chain: Spiral, Nagaoka and resonating-valence-bond states, phase separation, and Luttinger-liquid behavior". *Phys. Rev. B* 74.12 (2006), p. 125117.

[2] H. Tasaki. "The Hubbard model - an introduction and selected rigorous results". *J. Phys.: Condens. Matter* 10.20 (1998), p. 4353.

[3] O. Derzhko and J. Richter. "Structural instability of two- and three-dimensional pyrochlore spin lattices in high magnetic fields". *Phys. Rev. B* 72.9 (2005), p. 094437.

[4] O. Derzhko et al. "Low-temperature properties of the Hubbard model on highly frustrated one-dimensional lattices". *Phys. Rev. B* 81.1 (2010), p. 014421.

[5] Y. F. Duan and K. L. Yao. "Theoretical model of an organic ferrimagnetic state for a bipartite lozenge chain". *Phys. Rev. B* 63.13 (2001), p. 134434.

[6] J. Richter, O. Derzhko, and J. Schulenburg. "Magnetic-Field Induced Spin-Peierls Instability in Strongly Frustrated Quantum Spin Lattices". *Phys. Rev. Lett.* 93.10 (2004), p. 107206.

[7] J. Schulenburg et al. "Macroscopic Magnetization Jumps due to Independent Magnons in Frustrated Quantum Spin Lattices". *Phys. Rev. Lett.* 88.16 (2002), p. 167207.

[8] A. Mielke. "Exact ground states for the Hubbard model on the Kagome lattice". *Journal of Physics A* 25 (1992), p. 4335.

[9] O. Derzhko and J. Richter. "Finite low-temperature entropy of some strongly frustrated quantum spin lattices in the vicinity of the saturation field". *Phys. Rev. B* 70.10 (2004), p. 104415.

[10] J. Richter et al. "Exact eigenstates and macroscopic magnetization jumps in strongly frustrated spin lattices". *J. Phys.: Condens. Matter* 16.11 (2004), S779.

[11] R. R. Montenegro-Filho and M. D. Coutinho-Filho. "Magnetic and nonmagnetic phases in doped AB_2 t-J Hubbard chains". *Phys. Rev. B* 90 (2014), p. 115123.

[12] Z. Gulácsi, A. Kampf, and D. Vollhardt. "Exact Many-Electron Ground States on the Diamond Hubbard Chain". *Phys. Rev. Lett.* 99.2 (2007), p. 026404.

[13] A. A. Lopes, B. A. Z. António, and R. G. Dias. "Conductance through geometrically frustrated itinerant electronic systems". *Phys. Rev. B* 89 (2014), p. 235418.

[14] O. Rojas, S. M. de Souza, and N. S. Ananikian. "Geometrical frustration of an extended Hubbard diamond chain in the quasiatomic limit". *Phys. Rev. E* 85 (2012), p. 061123.

[15] O. Derzhko, J. Richter, and M. Maksymenko. "Strongly correlated flat-band systems: The route from Heisenberg spins to Hubbard electrons". *International Journal of Modern Physics B* 29.12 (2015), p. 1530007.

[16] D. Leykam et al. "Flat band states: Disorder and nonlinearity". *Phys. Rev. B* 88 (2013), p. 224203.

[17] H. Tamura et al. "Flat-band ferromagnetism in quantum dot superlattices". *Phys. Rev. B* 65.8 (2002), p. 085324.

[18] A. Mielke. "Ferromagnetism in Single-Band Hubbard Models with a Partially Flat Band". *Phys. Rev. Lett.* 82.21 (1999), pp. 4312–4315.

[19] C. Wu et al. "Flat Bands and Wigner Crystallization in the Honeycomb Optical Lattice". *Phys. Rev. Lett.* 99.7 (2007), p. 070401.

[20] A. Mielke and H. Tasaki. "Ferromagnetism in the Hubbard model". *Communications in Mathematical Physics* 158.2 (1993), pp. 341–371.

[21] A. Tanaka and H. Tasaki. "Metallic Ferromagnetism in the Hubbard Model: A Rigorous Example". *Phys. Rev. Lett.* 98.11 (2007), p. 116402.

[22] H. Tasaki. "Ferromagnetism in the Hubbard Models with Degenerate Single-Electron Ground States". *Physical Review Letters* 69 (1992), pp. 1608–1612.

[23] H. Tasaki. "Stability of Ferromagnetism in the Hubbard Model". *Phys. Rev. Lett.* 73.8 (1994), pp. 1158–1161.

[24] H. Tasaki. "From Nagaoka's Ferromagnetism to Flat-Band Ferromagnetism and Beyond". *Prog. Theor. Phys.* 99.4 (1998), pp. 489–548.

[25] H. Tasaki. "Ferromagnetism in Hubbard Models". *Phys. Rev. Lett.* 75.25 (1995), pp. 4678–4681.

[26] A. Mielke. "Ferromagnetism in the Hubbard model on line graphs and further considerations". *J. Phys. A-Math. Gen.* 24.14 (1991), p. 3311.

[27] J. Frohlich and D. Ueltschi. "Hund's Rule and Metallic Ferromagnetism". English. *Journal of Statistical Physics* 118.5-6 (2005), pp. 973–978.

[28] M. Nita, B. Ostahie, and A. Aldea. "Spectral and transport properties of the two-dimensional Lieb lattice". *Physical* 87 (2013), p. 125428.

[29] J. Gouveia and R. Dias. "Magnetic phase diagram of the Hubbard model in the Lieb lattice". *Journal of Magnetism and Magnetic Materials* 382 (2015), pp. 312–317.

[30] E. H. Lieb. "Two Theorems on the Hubbard model". *Physical Review Letters* 62 (1989), pp. 1201–1204.

[31] J. L. Movilla and J. Planelles. "Quantum level engineering for Aharonov-Bohm caging in the presence of electron-electron interactions". *Phys. Rev. B* 84 (2011), p. 195110.

[32] J. D. Bodyfelt et al. "Flatbands under Correlated Perturbations". *Phys. Rev. Lett.* 113 (2014), p. 236403.

[33] S. Flach et al. "Detangling flat bands into Fano lattices". *EPL (Europhysics Letters)* 105.3 (2014), p. 30001.

[34] C. Danieli, J. D. Bodyfelt, and S. Flach. "Flatband Engineering of Mobility Edges". *ArXiv e-prints* arXiv:1502.06690 [cond-mat.str-el] (2015).

[35] S. Shen. *Topological Insulators: Dirac Equation in Condensed Matters*. Springer Series in Solid-State Sciences. Springer, 2013.

[36] X.-L. Qi and S.-C. Zhang. "Topological insulators and superconductors". *Rev. Mod. Phys.* 83 (2011), pp. 1057–1110.

[37] M. Z. Hasan and C. L. Kane. "*Colloquium* : Topological insulators". *Rev. Mod. Phys.* 82 (2010), pp. 3045–3067.

[38] A. B. Harris and R. V. Lange. "Single-Particle Excitations in Narrow Energy Bands". *Phys. Rev.* 157 (1967), pp. 295–314.

[39] M. Ogata and H. Shiba. "Bethe-ansatz wave function, momentum distribution, and spin correlation in the one-dimensional strongly correlated Hubbard model". *Phys. Rev. B* 41 (1990), pp. 2326–2338.

[40] F. Gebhard et al. "Exact results for the optical absorption of strongly correlated electrons in a half-filled Peierls-distorted chain". *Phil. Mag. B* 75 (1997), pp. 13–46.

[41] R. G. Dias and J. M. B. Lopes dos Santos. "Simple representation of the eigenstates of the $U \to \infty$ one-dimensional Hubbard model". *Journal de Physique I* 2 (1992), pp. 1889–1897.

[42] N. M. R. Peres et al. "Finite-temperature transport in finite-size Hubbard rings in the strong-coupling limit". *Phys. Rev. B* 61.8 (2000), pp. 5169–5183.

[43] A. A. Lopes and R. G. Dias. "Interacting spinless fermions in a diamond chain". *Phys. Rev. B* 84 (2011), p. 085124.

[44] C. Lacroix, P. Mendels, and F. Mila. *Introduction to Frustrated Magnetism: Materials, Experiments, Theory*. Springer Series in Solid-State Sciences. Springer, 2011.

[45] U. Brandt and A. Giesekus. "Hubbard and Anderson models on perovskitelike lattices: Exactly solvable cases". *Phys. Rev. Lett.* 68 (1992), pp. 2648–2651.

[46] H. Tasaki. "Exact resonating-valence-bond ground state and possibility of superconductivity in repulsive Hubbard models". *Phys. Rev. Lett.* 70 (1993), pp. 3303–3306.

Chapter 6

Time evolution of localized states in Lieb lattices

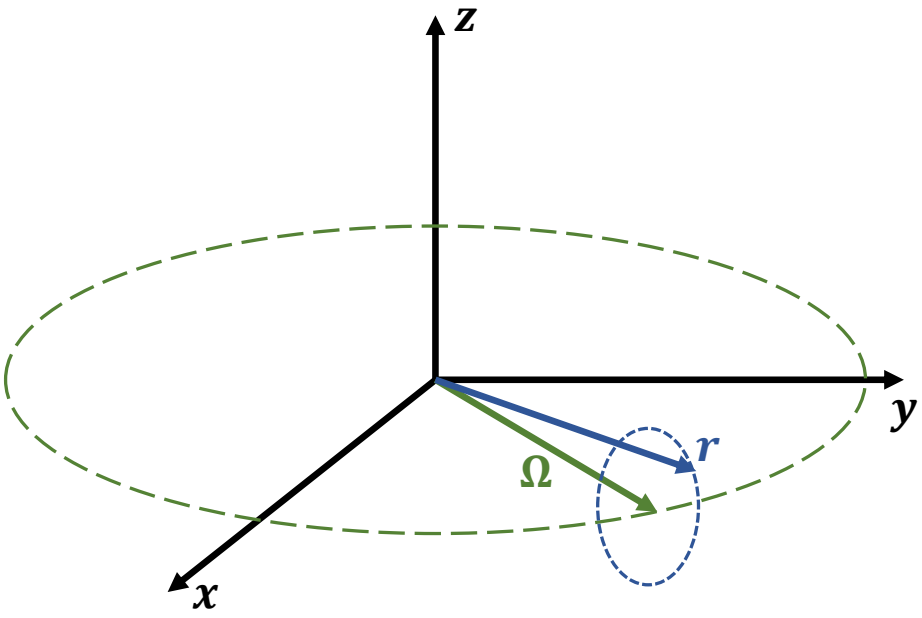

Submitted to Physical Review B and available at:
J. D. Gouveia, I. A. Maceira and R. G. Dias, *Time evolution of localized states in Lieb lattices.* arXiv:1607.04326 [quant-ph] (2016).

Abstract

We study the slow time evolution of localized states of the open-boundary Lieb lattice when a magnetic flux is applied perpendicularly to the lattice and increased linearly in time. In this system, Dirac cones periodically disappear, reappear and touch the flat band as the flux increases. We show that the slow time evolution of a localized state in this system is analogous to that of a zero-energy state in a three-level system whose energy levels intersect periodically and that this evolution can be mapped into a classical precession motion with a precession axis that rotates as times evolves. Beginning with a localized state of the Lieb lattice, as the magnetic flux is increased linearly and slowly, the evolving state precesses around a state with a small itinerant component and the amplitude of its localized component oscillates around a constant value (below but close to 1), except at multiples of the flux quantum where it may vary sharply. This behavior reflects the existence of an electric field (generated by the time-dependent magnetic field) which breaks the C_4 symmetry of the constant flux Hamiltonian.

6.1 Introduction

In flat-band systems, there is a high energy degeneracy associated with the existence of localized states (i.e. electrons trapped in a small region of a lattice due to destructive wave function interference). Recent interest in this area has arisen[1, 2] due to experimental realizations of flat-band systems using arrays of optical waveguides[3, 4], exciton-polarization condensates[5, 6], and cold atoms in optical lattices[7]. Known lattices with flat bands include the Lieb[8], Mielke[9] and Tasaki[10] lattices and there are methods of generating lattices of nearly arbitrary geometry which have these localized states when the hopping constants obey certain relations[11, 12].

These systems can be separated in two classes in what concerns the behavior of their flat band in the presence of an external magnetic field. In particular, the Mielke and Tasaki lattices do not display flat bands for finite magnetic flux. In contrast, lattices of the Lieb's class are flat-band robust in that they retain a flat band when a magnetic field is applied perpendicularly to the lattice. However, the introduction of magnetic flux requires that localized states occupy at least two plaquettes[13] and therefore, the flat band subspace as a whole evolves in the Hilbert space as the magnetic field is increased. In the case of the Lieb tight-binding (TB) model, the band structure has a Dirac point at $\mathbf{k} = (\pi, \pi)$. This model under an evolving magnetic field creates an interesting theoretical scenario: i) a flat band and Dirac bands that touch at the Dirac point when the magnetic flux per plaquette is a multiple of the flux quantum; ii) a perturbation such that the flat band persists, and the Dirac cones disappear and reappear periodically as the perturbation varies.

In this paper, we study the slow time evolution of localized states in the scenario described above. As stated by the adiabatic theorem [14], if the evolution of the perturbation (magnetic field) is slow enough, the evolving state, initially an eigenstate, is expected to closely remain an instantaneous eigenstate of the Hamiltonian at any time, as long as there is an energy difference between that eigenstate and the rest of eigenstates. Since energy levels periodically cross the flat band, this time evolution will periodically leave the adiabatic regime close to the crossing instants.

One of the questions we wish to answer is: near the energy crossing instants, can we picture the flat band system as a three-level system with one zero-energy (flat-band) state and two finite-energy ones? The motivation for this question is two-fold. First, if one considers a finite-size tight-binding lattice, the Dirac cones are replaced by discrete levels and, as the perturbation is increased, two of these levels cross the flat-band level. Second, the application of the perturbation to the flat-band tight-binding system introduces Hamiltonian terms that couple each dispersive state with flat-band states. However, as the flat band is degenerate, one can rotate the basis of the flat-band subspace in a way such that the perturbation couples the dispersive state with only *one* localized state (in analogy with what was done in Ref. [15]). We find that if the magnetic flux is applied linearly and slowly, the localized component of the evolving state oscillates around a constant value, except at energy crossing instants where it varies sharply. This reflects an intricate precession behavior of the evolving state around a state with a small itinerant component. Such a behavior is also found in the case of a three-level system whose energy levels intersect periodically. This precession behavior reflects the existence of an electric field in the Lieb lattice (generated by the time-dependent magnetic field) which breaks the C_4 symmetry of the constant flux Hamiltonian.

The paper is organized in the following way. First, we consider the tight-binding Hamiltonian of the Lieb lattice in the presence of magnetic flux (also called t-ϕ model). When the magnetic

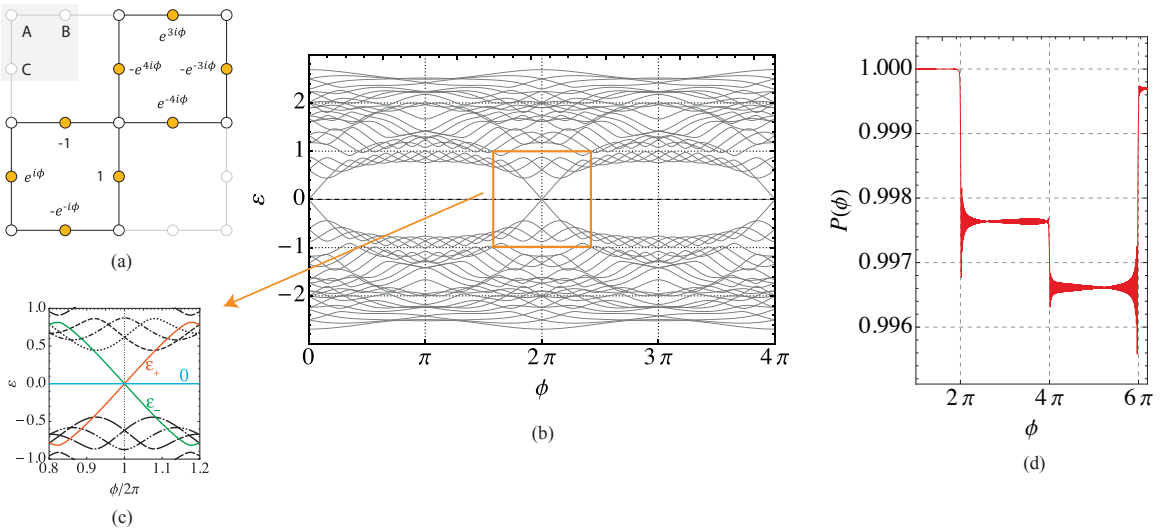

Figure 6.1: (a) Localized state in two contiguous plaquettes of the Lieb lattice with one common site, for the symmetric gauge $\mathbf{A} = \frac{B}{2}(-y, x, 0)$. Labeled circles represent finite wavefunction amplitudes, and the remaining sites are nodes of the wavefunction. (b) Energy spectrum of the Hamiltonian H (see text) as a function of the magnetic flux through a plaquette, ϕ, for the finite Lieb lattice with 4×4 plaquettes. (c) Closeup of an intersection point between the flat band and two dispersive states, which we call the two ε states. (d) Square of the absolute value of the projection of an evolving state $|\psi(t)\rangle$ onto the localized subspace of the eigenvectors of H, as a function of ϕ. The lattice comprises 4 plaquettes (2 in each direction x or y). The initial state is of the form of (a), with $\phi = \pi$. The time evolution is due to the linear change of the magnetic flux, $\phi(t) = \omega t$, $\omega = 2\pi \times 10^{-5}$ and $(x_0, y_0) = (-4, -4)$.

flux per plaquette is a multiple of the flux quantum, the flat band has two extra states, which we label $|\varepsilon_\pm\rangle$ states. We then analyze the time evolution of one of its localized eigenstates, starting at a certain initial magnetic flux and then varying the magnetic flux linearly and slowly. Secondly, we study a toy three-level system with a time-dependent Hamiltonian consisting of one zero-energy eigenstate and two finite-energy ones, whose energy periodically crosses the zero-energy line. We study the slow time evolution of the zero-energy state and find that it is equivalent to a classical precession motion, but with a nutation-like oscillation of the zero-energy component due to the rotation of the Hamiltonian eigenbasis. This precession motion may lead to huge long-time modifications of the state if, when the level crossings occur, the precession axis rotates with finite angular velocity. Thirdly, we show that analogous precession behavior is found in the evolution of any localized state of the Lieb lattice under time-dependent magnetic flux. In this case, since it is this time-dependence that leads to the rotation of the precession axis, we can also say it is a consequence of the electric field generated by the evolving vector potential.

6.2 Lieb lattice under magnetic flux

Let us consider the Lieb tight-binding model without magnetic flux. The Lieb lattice can be obtained from a traditional two-dimensional (2D) square lattice by removing one quarter of

its atoms in a regular pattern (see Fig. 6.1a). It is comprised of three sublattices (A, B and C). The eigenvalues of the nearest-neighbor TB model of this lattice (with unitary hopping constant) consist of three energy bands, one of which is flat, with zero energy[3, 16]. The energy of the dispersive bands has the form $\epsilon_{\pm}(k) = \pm 2\sqrt{\cos^2 \frac{k_x}{2} + \cos^2 \frac{k_y}{2}}$, where (for periodic boundary conditions) $k_\alpha = 2\pi n_\alpha / L_\alpha$, with $n_\alpha = 1, \cdots, L_\alpha$, and L_α is the number of unit cells in the α direction. The total number of unit cells is $N = L_x L_y$. The flat band is a high-degeneracy eigenspace composed of localized states (these states remain eigenstates when the system size is increased, implying that the respective probability density distribution is localized in a region of the lattice).

On an infinite Lieb lattice, the dispersive bands have Dirac cones that touch the flat band at the point $\mathbf{k} = (\pi, \pi)$. On a finite periodic Lieb lattice, this point is only allowed if both L_x and L_y are even. When this is the case, the degeneracy of the zero-energy subspace is $N + 2$. The number of localized states (degeneracy of the flat band) is $N + 1$. The remaining zero-energy state is the eigenstate of the dispersive bands that is located in the Dirac point. A localized state is also located at the Dirac point, effectively creating a two-state subspace that is degenerate for both energy and $\mathbf{k}$. [1] In contrast, on a Lieb lattice with open boundary conditions, the flat band is N-fold degenerate in the absence of magnetic flux. Note that localized states span only over B- and C-type atoms of the lattice, but the zero-energy dispersive state (corresponding to the Dirac point) spans uniquely A-type atoms. This state has finite amplitude at A-type atoms at the edges of the lattice, and consequently it is no longer an eigenstate if more plaquettes are added. The lower and upper dispersive bands involve all three sublattices A, B, and C. An important characteristic of the Lieb TB model is that in the presence of magnetic flux the flat band remains flat, albeit with degeneracy $N - 1$, that is, even in the presence of magnetic flux, one has localized eigenstates of the TB Hamiltonian induced by the wavefunction destructive interference associated with the particular Lieb geometry. [2]

To include a magnetic field in the model, we must consider the Peierls phase gained by the electron when it hops between lattice sites, $\theta_{ij} = \frac{\pi}{\phi_0} \int_i^j \mathbf{A} \cdot d\mathbf{l}$, where i and j label the (x, y) coordinates of the initial and final sites, respectively, $\mathbf{A}$ is the vector potential, and $\phi_0 = h/(2e)$ is the magnetic flux quantum. Assuming the symmetric gauge, $\mathbf{A} = \frac{B}{2}(-(y - y_0), x - x_0, 0)$, where B is the magnitude of the magnetic field and (x_0, y_0) is the center of the vector potential relative to the center of the lattice $(0, 0)$, the Lieb TB Hamiltonian in the presence of magnetic flux is obtained by applying the Peierls substitution to the standard TB Hamiltonian, and is given by[17]

$$\begin{aligned} H = -\sum_{\text{all A sites}} \Big(& e^{-i\phi \frac{(x-x_0)}{8}} B^\dagger_{x,y+1} + e^{i\phi \frac{(x-x_0)}{8}} B^\dagger_{x,y-1} \\ & + e^{i\phi \frac{(y-y_0)}{8}} C^\dagger_{x+1,y} + e^{-i\phi \frac{(y-y_0)}{8}} C^\dagger_{x-1,y} \Big) A_{x,y} + \text{H.c.}, \end{aligned} \tag{6.1}$$

where $\phi = 4B\pi/\phi_0$ is the normalized magnetic flux. Open boundaries are introduced considering only the set of the previous hopping terms within the boundaries of our lattice. The eigenvalues of the Lieb TB Hamiltonian as a function of ϕ are shown in Fig. 6.1b, which includes a

[1] The variable $\mathbf{k}$ should not be designated as momentum in the case of open boundary conditions, since the respective eigenstates are standing waves.

[2] The decrease in the degeneracy can be justified by the fact that, without flux, a localized state can occupy only one plaquette, while with flux, at least two plaquettes are required, which necessarily reduces the number of localized states.

zoomed-in energy-crossing point, Fig. 6.1c (see also Refs. [1, 16, 18]). A double Hofstadter butterfly arises in intervals of 2π.

The introduction of magnetic flux opens gaps between the bands, and two states, $|\varepsilon_+\rangle$ and $|\varepsilon_-\rangle$ (whose energies obey the relation $\varepsilon_+ = -\varepsilon_-$), leave the flat band (see Fig. 6.1c). These two states arise (up to zeroth order on the flux) from a combination of the two states in the zero-flux Dirac point, one dispersive and one localized. In states $|\varepsilon_+\rangle$ and $|\varepsilon_-\rangle$, the electron has equal probability of being at sublattices A or B/C. All A sites have the same probability of occupation, but for the B/C sites the probability increases quasi-exponentially as we move away from the center. This means that the overlap between a localized state and the $|\varepsilon_\pm\rangle$ states is stronger the closer the localized state is to the edge of the lattice. In these two states, the phase difference between nearest-neighbor sites is $\pi/2$ as we move clockwise in one of the ε states and anti-clockwise in the other. This can be interpreted as the two states having opposite angular momenta which, when coupled to the applied magnetic field, confers them symmetric energies at the energy crossing instants.

The zero-energy crossing at zero flux (or more generally, at multiples of the flux quantum) is rather particular. At zero flux and assuming $N_x = N_y$, the Lieb lattice shares the C_{4v} symmetry of the square lattice and therefore, one expects a zero-flux energy spectrum with non-degenerate (double degenerate) states which are even (odd) under the C_2 rotation. However, the zero-energy crossing involves the $|\varepsilon_\pm\rangle$ states which, when $(x_0, y_0) = (0, 0)$, are even under the C_2 symmetry. The introduction of flux lowers the symmetry of the lattice (or better, of the respective tight-binding Hamiltonian), from C_{4v} to C_4, if we consider a vector potential which has C_4 symmetry (as in the case $(x_0, y_0) = (0, 0)$), or to a lower symmetry otherwise.

Let us now consider a time-dependent magnetic flux. The time evolution of a localized eigenstate $|\psi(0)\rangle$ of the Lieb lattice is given by the time-dependent Schroedinger equation, $i\frac{\mathrm{d}}{\mathrm{d}t}|\psi\rangle = H|\psi\rangle$, so that $|\psi(t+\mathrm{d}t)\rangle = e^{-iH(t)\mathrm{d}t}|\psi(t)\rangle$. We considered, as initial state, a localized eigenstate of the Hamiltonian of the Lieb lattice at a certain magnetic flux, and numerically studied its evolution due to a time-dependent Hamiltonian $H(t)$ representing the slow linear change of the magnetic flux, $\phi(t) = \omega t$, where ω is the angular frequency of the Peierls phase. One should again note that a slowly-changing time-dependent vector potential implies a very small electric field[3].

Starting with the localized state of the Lieb lattice in Fig. 6.1a, placed at the center of a Lieb lattice with 2×2 plaquettes, with $\phi(t_0) = \pi$, the projection of $|\psi(t)\rangle$ onto the localized subspace of $H(t)$ is shown in Fig. 6.1d. This projection is given by $P(t) = \sum_i \langle 0_i|\psi(t)\rangle^2$, where the summation is over all zero-energy eigenstates, $|0_i\rangle$, of H. The fast oscillations with modulated amplitude and a larger-scale staircase behavior, seen in Fig. 6.1d, are also observed in larger lattices. Note that the sum of the state projections onto the localized basis is a particular state $|\tilde{0}\rangle$ of the subspace of localized states, $|\tilde{0}\rangle = \sum_i \langle 0_i|\psi(t)\rangle|0_i\rangle$.

The fact that the localized component exhibits a staircase behavior is a consequence of $|\psi(t)\rangle$ acquiring or losing dispersive component in the two ε states (see Fig. 6.1c) whenever the $\varepsilon_\pm$ energies cross the flat band (which occurs periodically, at $\phi = 2\pi n$), in accordance with the adiabatic theorem. This pattern can be successfully reproduced using a three-level toy model, as we show in the next section. We can justify this pattern by analyzing the equation of evolution of $|\psi(t)\rangle$ in the time-dependent eigenbasis $\{|\varepsilon_i(t)\rangle\}$ of the Hamiltonian, where we

[3]In the context of atomic physics, a gauge such that the electric field results from a time-dependent vector potential is designated a velocity gauge.

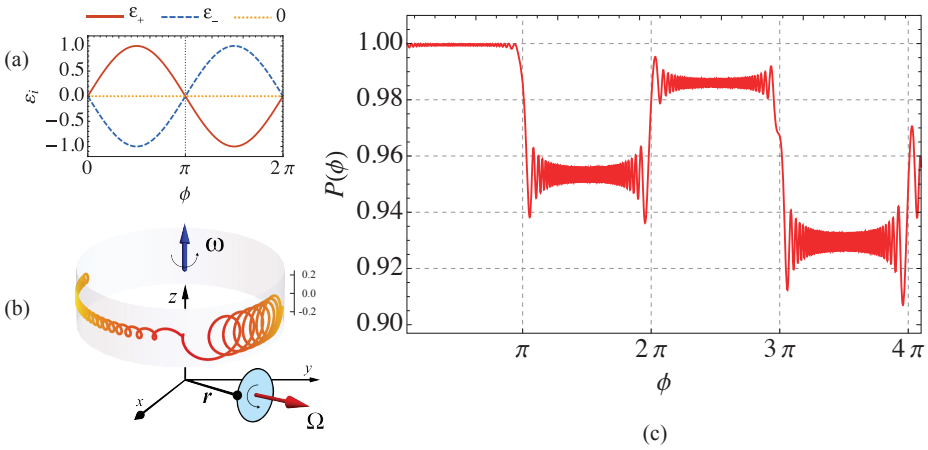

Figure 6.2: (a) Energy spectrum of the three-level toy Hamiltonian H_3 as a function of $\phi = \omega_1 t$. The spectrum includes three energy bands, with energies 0 and $\varepsilon_\pm = \pm\sin(\omega_1 t)$. (b) Illustration of the solution $|\psi(t)\rangle$ of the Schroedinger equation describing our three-level toy model as a classical mechanics precessing position vector $\mathbf{r}(t) = |\psi(t)\rangle$. The vectors here have the same meaning as in Eq. 6.4. The trajectory described by the vector $\mathbf{r}(t)$ is the curly orange line and results from solving Eq. 6.4, with $\omega_1 = \omega_2 = 2\pi/1000$, and initial condition $\mathbf{r}(\omega_1 t = \pi/10) = (\cos(\pi/10), \sin(\pi/10), 0)$, i.e., a purely localized state. Note that the direction of precession changes whenever the sign of $\varepsilon(t)$ changes. (c) Projection of the evolving state $|\psi(t)\rangle$ onto the zero-energy state of the toy Hamiltonian H_3 as a function of ϕ. The parameters considered are the same as in (b).

can write $|\psi(t)\rangle = \sum_i \alpha_i(t)|\varepsilon_i(t)\rangle$. This leads to the equation

$$\mathrm{d}\Psi/\mathrm{d}t = (-iH_d + D)\Psi, \tag{6.2}$$

where $\Psi(t) = \{\alpha_i(t)\}$ is the column vector of the components of $|\psi(t)\rangle$ in the eigenbasis $\{|\varepsilon_i(t)\rangle\}$. In the equation above, H_d is the diagonalized Hamiltonian matrix and $D_{ij} \equiv \frac{\mathrm{d}\langle\varepsilon_i|}{\mathrm{d}t}|\varepsilon_j\rangle = \frac{\mathrm{d}\phi}{\mathrm{d}t}\frac{\mathrm{d}\langle\varepsilon_i|}{\mathrm{d}\phi}|\varepsilon_j\rangle$ where ϕ is the magnetic flux that will be varied quasi-adiabatically over time. This implies $\mathrm{d}\phi/\mathrm{d}t$ is small enough that the energy differences between states i and j, $\Delta\varepsilon_{ij}$, are (mostly) much greater than the elements that couple those states, D_{ij}, so that the matrix D can be considered a perturbation of the system. In this case, the evolution is mostly determined by the diagonalized Hamiltonian, resulting in constant $|\alpha_i|$ of the evolving state. However, if $\Delta\varepsilon_{ij}$ is zero at some instant t_1, the element D_{ij} will dominate the evolution on a finite interval around t_1 for any (finite) choice of $\mathrm{d}\phi/\mathrm{d}t$, resulting in a permanent exchange of component weight between states i and j.

6.3 Three-level toy model

In this section, we show that the fast oscillations with modulated amplitude and the larger-scale staircase behavior of the localized component described in the previous section can be understood considering a simple three-level system. The three-level toy Hamiltonian,

before basis rotation, comprises one zero-energy eigenstate and two finite-energy ones, [4] and its matrix representation at time t can be

$$\tilde{H}_3 = \begin{pmatrix} 0 & 0 & 0 \\ 0 & 0 & \varepsilon(t) \\ 0 & \varepsilon(t) & 0 \end{pmatrix}, \tag{6.3}$$

with eigenvalues 0 and $\varepsilon_\pm = \pm\varepsilon(t)$, where $\varepsilon(t) = \varepsilon_0 \sin(\omega_1 t)$. The eigenvalues are therefore distinct for all times except $\omega_1 t = n\pi$, with $n \in \mathbb{Z}$ (see Fig. 6.2a), an effective simplification of the zero-energy crossing instants which occur in the case of the Lieb lattice (see Fig. 6.1c).

Additionally, a rotation of the eigenbasis of the toy Hamiltonian should be considered. We choose a simple case of a unitary transformation, the rotation matrix U about the z axis, with angular velocity ω_2, so that the zero-energy state mixes with the other two states. The full toy Hamiltonian is $H_3 = U\tilde{H}_3 U^\dagger$. The zero-energy state of H_3 at time t is $|0(t)\rangle = (\cos(\omega_2 t), \sin(\omega_2 t), 0)$, and the (not normalized) eigenstates with energies $\varepsilon_\pm$ are $(\sin(\omega_2 t), \cos(\omega_2 t), \pm 1)$. Other rotations could be considered by substituting $\omega_2 t$ with the appropriate time-dependent functions. We comment the case of a general unitary operator U (with complex matrix entries) in the next section.

The evolution of a quantum state due to this Hamiltonian can then be studied by solving the time-dependent Schroedinger equation, $H_3|\psi(t)\rangle = i\frac{\mathrm{d}}{\mathrm{d}t}|\psi(t)\rangle$. One can then plot the projection of the solution vector, $|\psi(t)\rangle = (x(t), y(t), z(t))$, onto the zero-energy state, $P_0(t) = |\langle\psi(t)|0(t)\rangle|^2$. A numerically-obtained plot of $P_0(t)$ is shown in Fig. 6.2d, where we assumed $\omega_1 = \omega_2$ for simplicity. The energy of the evolving state, $\langle\psi(\varepsilon)|H_3|\psi(\varepsilon)\rangle$, was found to remain zero (lower than 10^{-16} in our numerical calculations) at all times during the evolution.

The solution of this system can actually be visualized in 3D, as a position vector. First, since $x(t)$ and $y(t)$ have zero imaginary part, and $z(t)$ has zero real part, we make all three components purely real, by replacing z with iz and consider the position vector, $\mathbf{r}(t) = (x(t), y(t), z(t))$. That turns the Hamiltonian into a skew-symmetric matrix, which can be identified as the matrix multiplication form of a vector cross product. Finally, the Schroedinger equation $H_3|\psi(t)\rangle = i\hbar\frac{\mathrm{d}}{\mathrm{d}t}|\psi(t)\rangle$ becomes a classical mechanics precession equation,

$$\dot{\mathbf{r}}(t) = \boldsymbol{\Omega}(t) \times \mathbf{r}(t), \tag{6.4}$$

with $\boldsymbol{\Omega}(t) = \frac{\varepsilon_0 \sin(\omega_1 t)}{\hbar}[\cos(\omega_2 t), \sin(\omega_2 t), 0]$. This is the equation of motion that describes the precession of a vector $\mathbf{r}(t)$ around the vector $\boldsymbol{\Omega}(t)$, which in turn rotates about the z axis (Fig. 6.2b). Thus, in this classical perspective, ω_1 is responsible for the change of the length of $\boldsymbol{\Omega}(t)$ over time and ω_2 gives the rotation of $\boldsymbol{\Omega}(t)$ around the z axis.

Because the velocity, $\dot{\mathbf{r}}(t)$, is orthogonal to $\mathbf{r}(t)$ at all times, the norm of $\mathbf{r}(t)$ is kept constant. The vector $\boldsymbol{\Omega}(t)$ is the zero-energy eigenstate of the Hamiltonian, multiplied by $\varepsilon_0 \sin(\omega_1 t)/\hbar$. The zero-energy component of $\mathbf{r}(t)$ is therefore proportional to the cosine of the angle between $\mathbf{r}(t)$ and $\boldsymbol{\Omega}(t)$. At the energy intersection points ($\omega_1 t = n\pi$), the velocity goes to zero and $\mathbf{r}(t)$ moves more slowly. However, at these points, $\boldsymbol{\Omega}(t)$ continues to rotate at the same angular velocity so that, naturally, the angle between the two vectors changes considerably, inducing the sudden increases or decreases in the localized component that can be seen in Fig. 6.2d.

[4] One could also consider a toy system of only two levels corresponding to one zero-energy state and one finite energy state. However, such a toy model would fail to fix the near-zero energy of the evolving state which is observed in flat-band systems. The evolving state needs to be allowed to mix with two other states with symmetric energies, lest the energy change.

Away from the intersection points, $P_0(t)$ displays rapid oscillations which reflect the precession of $\mathbf{r}$ around $\mathbf{\Omega}$, as well as the rotation of $\mathbf{\Omega}$.

In the rotating frame of reference that follows the zero-energy eigenstate, the precession vector acquires a component in the z direction, $\mathbf{\Omega} = [\varepsilon_0 \sin(\omega_1 t)/\hbar, 0, -\omega_2]$. The instantaneous frequency of the rapid oscillations of $P_0(t)$ observed in Fig. 6.2d equals the norm of the precession vector in the rotating frame, $\Omega = \sqrt{(\varepsilon_0 \sin(\omega_1 t)/\hbar)^2 + \omega_2^2}$ (however, if ω_2 is zero, no oscillations will be observed). Indeed, a WKB-like approach can be used to find an approximate solution of the three-level model in the regime $|\varepsilon(t)/\hbar| \gg |\omega_2| \Rightarrow \Omega(t) \approx \varepsilon(t)/\hbar$. The approximate solution for the localized projection $\langle\psi(t)|0(t)\rangle$ between two consecutive zero-energy crossing instants is

$$c\frac{\varepsilon_0}{\Omega}\sin(\omega_1 t) + \sqrt{1-c^2}\frac{\omega_2}{\Omega}\cos\left(-\frac{\varepsilon_0}{\omega_1}\cos(\omega_1 t) + \theta_0\right), \tag{6.5}$$

where $-1 < c < 1$ and θ_0 are initial condition parameters. This is still a valid equation even if we used a more general rotation of the eigenstates, i.e. if the z component of the rotating frame precession vector, $-\omega_2$, was substituted by any time-dependent function. This means that the amplitude of the high frequency oscillation of $|\langle\psi(t)|0(t)\rangle|^2$ will be approximately given by $|\omega_2/\Omega|^2$.

6.4 Electric field symmetry

In the previous section, we showed that a simple three-level system can reproduce the basic features of an evolving localized state in the Lieb lattice, namely the fast oscillations with modulated amplitude of the localized component and the larger-scale staircase behavior. The precession of $\mathbf{r}(t)$ in the case of the toy model implies that the oscillations observed in the case of the Lieb lattice can be qualitatively interpreted as a precession of the evolving state around a state which is approximately the state $|\tilde{0}\rangle$ defined in section 6.2, but also has small $|\varepsilon_\pm\rangle$ components (and even smaller components on other itinerant states). Furthermore, the nodes and antinodes in the amplitude of the oscillations at each step of the staircase (this effect is more explicit for larger lattices) observed in Fig. 6.1d can also be reproduced by the toy model by tweaking ω_2, as it modulates the amplitude of the oscillations. This implies that, if in a certain instant ω_2 is zero, then a node will be observed in the amplitude of the oscillations (see Eq. 6.5).

In the case of the Lieb lattice, and in analogy with the three-level system, a rotation between the $|\varepsilon_\pm\rangle$ states and the localized states occurs as time evolves. Since this rotation occurs as the magnetic flux is increased, one expects the rotation to be proportional to the time derivative of the Hamiltonian. Since the time dependence of the Hamiltonian is present only in the vector potential, the rotation reflects the existence of an electric field. But does any electric field generate such a rotation? Or equivalently, is it possible to define a time-dependent vector potential such that the corresponding electric field does not cause the step-like behavior of the localized component of the evolving state? The answer lies in the relative symmetry of the lattice and the vector potential. As mentioned above, a slowly-changing time-dependent vector potential implies a very small electric field, given by $\mathbf{E} = -\partial\mathbf{A}/\partial t$. In this work, we used the symmetric gauge, $\mathbf{A} = \frac{B(t)}{2}(y_0 - y, x - x_0, 0)$ with a linear time dependence of the magnetic field, $B(t) = \omega t \phi_0/(4\pi)$. The specific case where $(x_0, y_0) = (0, 0)$, meaning the center of the gauge is the same as that of the lattice, leads to the same magnetic field, but a different electric field, and the step-like behavior vanishes. In this case, both the system and the electric

field possess rotation invariance at the center of the lattice and therefore, eigenstates of H have odd or even parity in relation to the center of the lattice. In particular, one can choose a Hamiltonian eigenbasis for the localized states, $\{|0_i(t)\rangle\}$, such that all states have a defined parity.

In a time-dependent evolution, the transition rate between eigenstates $|\varepsilon_+(t)\rangle$ and $|0_i(t)\rangle$ is given by $D_{+0_i}(t) = \langle \frac{\mathrm{d}\varepsilon_+}{\mathrm{d}t}|0_i(t)\rangle$, if $\varepsilon_+ \neq 0$. Using the C_4 symmetries of both states, one can show that the transition rate at the crossing points $\phi = 2\pi n$ is proportional to the amplitude of the uniform component of the electric field, $D_{+0_i}(\phi = 2\pi n) \propto \omega\sqrt{x_0^2 + y_0^2}$ (see Ref. [19] for more details). As stated by the adiabatic theorem, a slow time evolution may only leave the adiabatic regime if an energy difference of zero is met. However, as discussed in the analysis of Eq. 6.2, the adiabatic regime is abandoned when the matrix elements of D are sufficiently larger than the energy differences between the respective states. Since $D_{+0_i} = 0$ exactly at the same time as the energy difference is zero, there is not a finite time interval around the crossing instants where $D_{+0_i} \gg \Delta E_{+0_i}$, so that adiabaticity is not lost even though the energy levels meet, causing the absence of the staircase behavior when the electric field shares its center with the lattice.

6.5 Conclusion

In conclusion, we have studied the slow time evolution of localized states of the Lieb lattice with increasing magnetic flux. A curious step pattern of the localized component has been found and we have shown that this behavior can be interpreted as a precession movement of the evolving state around a time-dependent vector with a large localized component and a much smaller dispersive component. The small dispersive component changes sharply at the energy-crossing points and corresponds mainly to two eigenstates of the Hamiltonian whose energy periodically crosses the zero-energy line. We have shown that this behavior can be understood considering a simple three-level toy model consisting of a Hamiltonian with three time-dependent eigenstates, such that one of them has constant zero energy and the other two periodically cross the zero-energy line.

This behavior should also occur due to perturbations that, similarly to the magnetic and electric fields, lift the C_{4v} symmetry of the Lieb lattice. We also expect that other flat band systems display the same features. For example, similar behavior is found in the AB_2 chain[13], which is bipartite and also has a flat band which is robust against the application of a magnetic field.

Concerning the experimental observation of the physics described in this paper, the step pattern may be observed in Lieb optical lattices under time-dependent perturbations or in Lieb photonic lattices, using a spatial modulation of the properties of the waveguide[20] to replicate the time-dependent magnetic field[21, 22], by measuring the light intensity at an A-type waveguide over its length, we can approximately measure the itinerant component over time.

References

[1] N. Goldman, D. F. Urban, and D. Bercioux. "Topological phases for fermionic cold atoms on the Lieb lattice". *Phys. Rev. A* 83 (2011), p. 063601.

[2] D. Leykam et al. "Localization of weakly disordered flat band states". *arXiv:1601.03784v1* (2016).

[3] S. Mukherjee et al. "Observation of a Localized Flat-Band State in a Photonic Lieb Lattice". *Phys. Rev. Lett.* 114 (2015), p. 245504.

[4] R. A. Vicencio et al. "Observation of Localized States in Lieb Photonic Lattices". *Phys. Rev. Lett.* 114 (2015), p. 245503.

[5] N. Masumoto et al. "Exciton-polariton condensates with flat bands in a two-dimensional kagome lattice". *New Journal of Physics* 14.6 (2012), p. 065002.

[6] F. Baboux et al. "Bosonic Condensation and Disorder-Induced Localization in a Flat Band". *Phys. Rev. Lett.* 116 (2016), p. 066402.

[7] S. Taie et al. "Coherent driving and freezing of bosonic matter wave in an optical Lieb lattice". *Science Advances* 1.10 (2015).

[8] E. H. Lieb. "Two Theorems on the Hubbard model". *Physical Review Letters* 62 (1989), pp. 1201–1204.

[9] A. Mielke. "Exact ground states for the Hubbard model on the Kagome lattice". *Journal of Physics A* 25 (1992), p. 4335.

[10] H. Tasaki. "Ferromagnetism in the Hubbard Models with Degenerate Single-Electron Ground States". *Physical Review Letters* 69 (1992), pp. 1608–1612.

[11] S. Flach et al. "Detangling flat bands into Fano lattices". *EPL (Europhysics Letters)* 105.3 (2014), p. 30001.

[12] R. G. Dias and J. D. Gouveia. "Origami rules for the construction of localized eigenstates of the Hubbard model in decorated lattices". *Scientific Reports, 16852* (2015).

[13] A. A. Lopes and R. G. Dias. "Interacting spinless fermions in a diamond chain". *Phys. Rev. B* 84 (2011), p. 085124.

[14] M. Born and V. Fock. "Beweis des Adiabatensatzes". *Zeitschrift fur Physik* 51.3 (1928), pp. 165–180.

[15] A. A. Lopes, B. A. Z. António, and R. G. Dias. "Conductance through geometrically frustrated itinerant electronic systems". *Phys. Rev. B* 89 (2014), p. 235418.

[16] M. Nita, B. Ostahie, and A. Aldea. "Spectral and transport properties of the two-dimensional Lieb lattice". *Physical* 87 (2013), p. 125428.

[17] A. B. Harris, T. C. Lubensky, and E. J. Mele. "Flux phases in two-dimensional tight-binding models". *Phys. Rev. B* 40 (1989), pp. 2631–2634.

[18] H. Aoki, M. Ando, and H. Matsumura. "Hofstadter butterflies for flat bands". *Phys. Rev. B* 54.24 (1996), R17296–R17299.

[19] I. A. Maceira. "Time evolution of localized states of the Lieb lattice". MA thesis. Portugal: Universidade de Aveiro, 2016.

[20] S. Longhi et al. "Observation of Dynamic Localization in Periodically Curved Waveguide Arrays". *Phys. Rev. Lett.* 96 (2006), p. 243901.

[21] M. Golshani et al. "Impact of Loss on the Wave Dynamics in Photonic Waveguide Lattices". *Phys. Rev. Lett.* 113 (2014), p. 123903.

[22] S. Flach and R. Khomeriki. "Fractional lattice charge transport". *arXiv:1606.03703 [cond-mat.dis-nn]* (2016), pp. 1–5.

Chapter 7

Mean-field phase diagram of the Hubbard model in the Lieb lattice

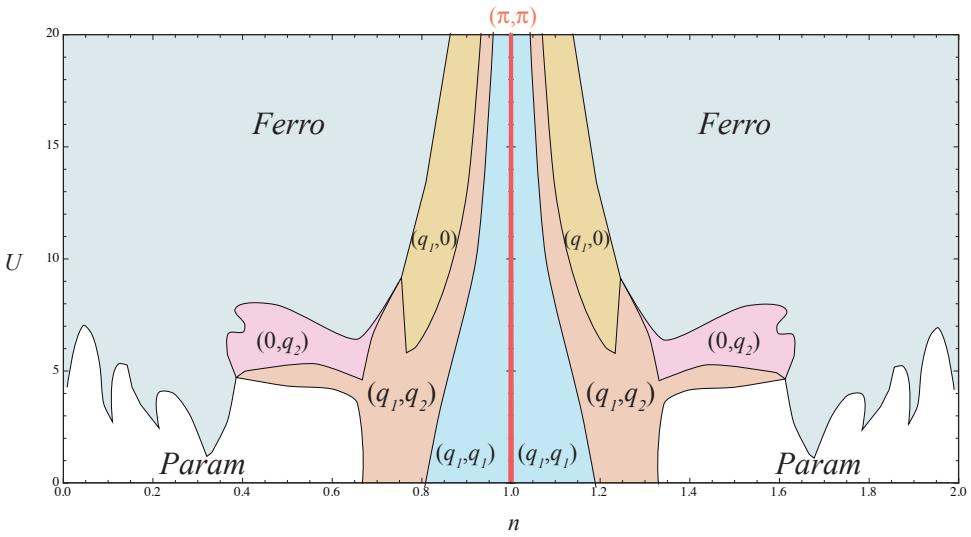

Adapted from:
J. D. Gouveia and R. G. Dias, Magnetic phase diagram of the Hubbard model in the Lieb lattice. Journal of Magnetism and Magnetic Materials, Volume 382, 15 May 2015, Pages 312-317
DOI: 10.1016/j.jmmm.2015.02.005

Abstract

We study the mean-field phase diagram of the repulsive Hubbard model in the Lieb lattice. Far from half-filling, the most stable phases are paramagnetism for low on-site interaction U/t and ferromagnetism for high U/t, as in the case of the mean-field phase diagram of the square lattice Hubbard model obtained by Dzierzawa[1]. At half-filling, the ground state was found to be ferrimagnetic [a (π, π) spiral phase], in agreement with a theorem by Lieb[2]. The total magnetization approaches Lieb's prediction as U/t becomes large. As we move away from half-filling, this ferrimagnetic phase becomes a (q_1, q_1) spiral phase with $q_1 \approx \pi$ and then undergoes a series of first-order phase transitions, $(q_1, q_1) \rightarrow (q_1, q_2) \rightarrow (q_1, 0)$, with $q_2 \approx \pi/2$, before becoming ferromagnetic at large U/t or paramagnetic at low U/t.

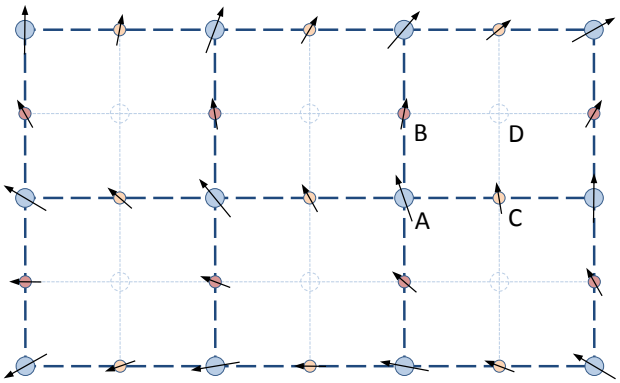

Figure 7.1: A square lattice can be divided into four sublattices A, B, C and D. The circles represent atomic nuclei and the arrows represent spins. The Lieb lattice can be obtained by removing one of the sublattices.

7.1 Introduction

The Hubbard model is one of the most studied models in the area of strongly correlated electron systems [3, 4]. However, it remains unsolved for dimensionality larger than one. For the one-dimensional (1D) case, the exact solution is given by the Bethe Ansatz [5], while in the case of two dimensions (2D), the solution is known only in some limiting cases or by means of approximations, such as mean-field. The fermionic Hubbard model in a square lattice has long been known to display antiferromagnetism (AF) at half-filling [6]. However, away from half-filling, the ground state magnetic ordering is still an open problem [7].

Extensions of the Hubbard model to 2D decorated lattices also show interesting features, such as flat band ferromagnetism (F) [2] and Dirac cones [8]. These decorated 2D lattices fall into three classes: Lieb's [2], Mielke's [9] and Tasaki's [10]. The pursuit for metallic ferromagnetism has motivated the search of crystal structures matching these decorated lattices. However, there are experimental obstacles, such as the lifting of the flat-band degeneracy by the Jahn-Teller effect or the difficulty in controlling the filling of the lattice. An alternative experimental approach is to study quantum dot arrays with these geometries [11]. Decorated lattices can also be realized by manipulating cold atoms in optical lattices [12].

Here, we study one example of a 2D decorated lattice, the Lieb lattice, i.e., a line-centered square lattice [13]. This kind of lattice can be obtained from the usual 2D square lattice by removing a quarter of its atoms (see Fig. 7.1). Each unit cell contains one atom of each kind: A, B and C. As a matter of fact, real materials can have their atoms arranged in a fashion resembling the Lieb lattice. Examples include the well-known high-T_c superconductors with weakly coupled CuO_2 planes [14, 15], such as $La_{2-x}Sr_xCuO_4$ and $YBa_2Cu_3O_7$, which can be studied using the perovskite lattice, a three-dimensional (3D) generalization of the Lieb lattice [16].

Exact results for magnetism in the Lieb lattice are known. For example, an important theorem proven by Lieb [2] states that bipartite lattices (lattices with two sublattices, A and B, such that each site on sublattice A has its nearest neighbors on sublattice B, and vice versa) whose unit cell contains a different number of each kind of atom, have ferromagnetic ground states at half-filling. This is the case of the Lieb lattice [17], as each unit cell contains one A atom and two B-like atoms. One common argument is that these states are in fact

ferrimagnetic [18], in the sense that although each sublattice is ferromagnetic, the full lattice is antiferromagnetic, but the magnetization is finite due to the different number of atoms in each sublattice. This contrasts with the antiferromagnetic ordering of the square lattice Hubbard model in this limit. Note that Lieb's theorem only mentions the total magnetization per unit cell, not on-site magnetization amplitudes, which can be calculated using numerical methods, such as mean-field. This has been done for the multi-layer Lieb optical lattice at half-filling [19].

In this work, we use a mean-field approach to compute the magnetic phase diagram of the Lieb lattice as a function of the average electron density n and Hubbard interaction U, thus going away from both half-filling and the tight-binding limit. The allowed magnetic phases are paramagnetism and spin spiral phases [20]. Ferro- and ferrimagnetism can be obtained as particular cases of spiral phases. Note that we do not consider spatial phase separation. In order to find such regions in the phase diagram, one needs to use the chemical potential as an independent variable [21–23], rather than using the particle density.

The tight-binding Hamiltonian of the Lieb lattice, H_t, is given by [24]

$$\begin{aligned} t \sum_{x=1}^{L_x} \sum_{y=1}^{L_y} \Big[& (A_{x,y}^\dagger B_{x,y} + A_{x,y}^\dagger C_{x,y} + H.c.) \\ & + (A_{x,y}^\dagger B_{x,y-1} + A_{x,y}^\dagger C_{x-1,y} + H.c.) \Big] . \end{aligned} \tag{7.1}$$

L_x (L_y) is the number of unit cells along the x (y) direction. The hopping terms in the first line are intra-unit cell and the remaining ones are inter-unit cell. The eigenvalues of H_t originate three energy bands, one of which is flat. The dispersion relation for periodic boundary conditions is

$$\varepsilon_\pm = \pm 2t \sqrt{\cos^2 \frac{k_x}{2} + \cos^2 \frac{k_y}{2}}, \tag{7.2}$$

for the non-flat energy bands, where $k_\alpha = 2\pi n_\alpha / L_\alpha$ with $n_\alpha = 0, 1, \cdots, L_\alpha$ and $\alpha \in \{x, y\}$. The flat band is $L_x L_y$-fold degenerate with zero energy. The one-particle localized states associated with the flat bands can be written as

$$|\mathrm{loc}; x, y\rangle = \frac{1}{2} \left(B_{x,y}^\dagger - C_{x,y}^\dagger + B_{x,y-1}^\dagger - C_{x-1,y}^\dagger \right) |\mathrm{vac}\rangle . \tag{7.3}$$

These states form a non-orthogonal basis of the flat band subspace.

The three tight-binding energy bands of the Lieb lattice energy bands are shown in Fig. 7.2a. At the point $(k_x, k_y) = (\pi, \pi)$, the three branches touch each other. Expanding the dispersion relation in Eq. 7.2 around this point, we find the Dirac cones $\varepsilon^2 = t^2(k_x^2 + k_y^2)$. The flat band is built up from B- and C-type orbitals in equal shares, while the lower and upper bands involve all three sublattices A, B and C.

The particle density of a sublattice equals the number of electrons at that sublattice divided by the number of atoms the sublattice comprises, or the number of unit cells,

$$\begin{aligned} n_A &= \tfrac{N_A}{L_x L_y} \\ n_B &= \tfrac{N_B}{L_x L_y} \\ n_C &= \tfrac{N_C}{L_x L_y}. \end{aligned} \tag{7.4}$$

In the non-interacting limit and at zero temperature, the particle density on sublattices A, B and C as a function of the global particle density (number of electrons in the whole lattice

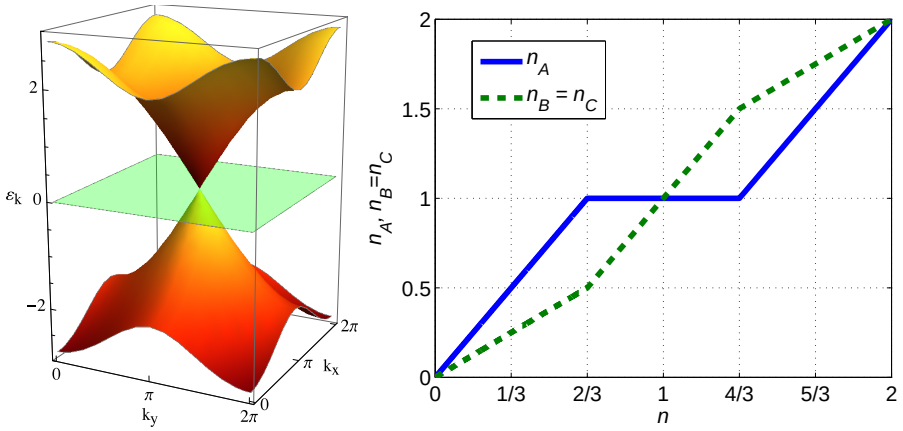

Figure 7.2: (a) Plot of the tight-binding dispersion relation of the Hubbard model in the Lieb lattice and (b) the respective particle density of each sublattice, A, B or C, as a function of the total particle density.

divided by the total number of sites) is as plotted in Fig. 7.2b. The plot can be interpreted as follows. Half of the probability density of the states in the lower dispersive band correspond to the sublattice A, while the other half is evenly distributed among sublattices B and C. Therefore, starting at $n = 0$, as we insert electrons in the system, half "choose" sublattice A, while the other half go to sublattices B or C. At $n = 2/3$, we reach the flat band at $\varepsilon = 0$. At this point, all sites A are singly occupied, while sites B and C are quarter-filled. Any newly-added electrons will only go to sublattices B or C, because the flat band only comprises these two kinds of atoms and going to sublattice A would imply going to the upper dispersive band, which would lead to higher total energy. At $n = 4/3$, the flat band is completely filled, so that for $n > 4/3$ electrons occupy the upper dispersive band going to sites A or B/C at a ratio of 2:1, as in the lower dispersive band, up to the maximum filling $n_A = n_B = n_C = 2$.

In this work, we address magnetism in the Lieb lattice by considering a finite on-site Coulomb repulsion U using a mean-field approach, and build a $n - U$ phase diagram. In the case of a square lattice, one assumes that the occupation number is the same in the whole lattice. Here, in the case of the Lieb lattice, we assume that the occupation number on each sublattice is the same as in the tight-binding limit, for any U (see Fig. 7.2b). This is the correct assumption for small U/t. Moreover, for large U/t, the results of Fig. 7.5 remain qualitatively the same for $n_A = n_B = n_C = n$.

7.2 Calculations

The interaction term of the Hubbard Hamiltonian is

$$H_U = U \sum_{\text{sites}} n_\uparrow n_\downarrow, \tag{7.5}$$

that is, the on-site Coulomb repulsion U times the number of double occupancies in the lattice. Applying the mean-field approximation to the Hubbard Hamiltonian gives single-particle

energies given by the eigenvalues of the 6×6 single-particle Hamiltonian H_{MF} [1, 25, 26],

$$\begin{pmatrix} \frac{Un_A}{2} & -t(1+e^{ik_y}) & -t(1+e^{ik_x}) & -\frac{mU}{2} & 0 & 0 \\ -t(1+e^{-ik_y}) & \frac{Un_B}{2} & 0 & 0 & -\frac{mU}{2}e^{-iq_y} & 0 \\ -t(1+e^{-ik_x}) & 0 & \frac{Un_C}{2} & 0 & 0 & -\frac{mU}{2}e^{-iq_x} \\ -\frac{mU}{2} & 0 & 0 & \frac{Un_A}{2} & -t(1+e^{i(k_y+2q_y)}) & -t(1+e^{i(k_x+2q_x)}) \\ 0 & -\frac{mU}{2}e^{iq_y} & 0 & -t(1+e^{-i(k_y+2q_y)}) & \frac{Un_B}{2} & 0 \\ 0 & 0 & -\frac{mU}{2}e^{iq_x} & -t(1+e^{-i(k_x+2q_x)}) & 0 & \frac{Un_C}{2} \end{pmatrix}, \tag{7.6}$$

plus the diagonal term

$$\frac{UL_{\mathrm{uc}}}{4}(3m^2 - n_A^2 - n_B^2 - n_C^2). \tag{7.7}$$

This is a generalization of the Hamiltonian obtained in previous studies of the 2D square lattice Hubbard model [1, 25, 26], which did not allow for different occupations in the sublattices. The magnetic phase of the system is defined by two order parameters: the vector $\vec{q}$ and the number m, as in the works by Dzierzawa [1] and Singh [25]. The vector $\vec{q} = (q_x, q_y)$ defines the orientation of the spins. For example, $q_x = 0$ is a ferromagnetic phase along the x direction, $q_y = \pi$ represents antiferromagnetism along the y direction, and other values of q_x or q_y give spin spiral phases. The paramagnetic phase is $\vec{q}$-degenerate and is characterized by zero magnetization amplitude. The magnetization amplitude m can be identified as the amplitude of the spin spiral wave,

$$\langle \vec{S}_{\vec{r}} \rangle = \frac{m}{2}\left(\cos(\vec{q}\cdot\vec{r}), \sin(\vec{q}\cdot\vec{r}), 0\right), \tag{7.8}$$

and appears during the mean-field calculations, when computing averages such as

$$\langle A_\uparrow^\dagger A_\downarrow \rangle = \langle S_A^+ \rangle = \langle S_{A,x} + iS_{A,y} \rangle = \frac{m}{2} e^{i\vec{q}\cdot\vec{r}_A}, \tag{7.9}$$

for sublattice A. Fig. 7.3 shows what the configuration of the Lieb lattice looks like when $\vec{q} = (\pi, \pi)$ and m is finite.

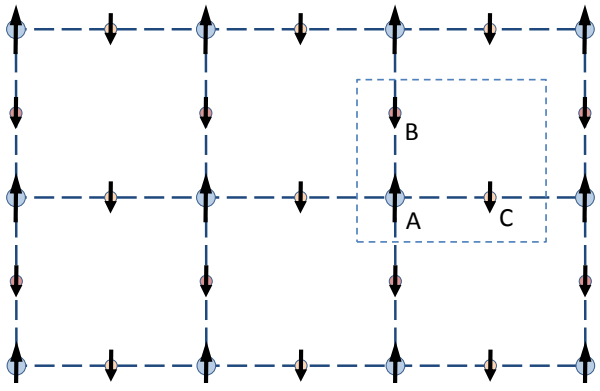

Figure 7.3: According to our definition of $\vec{q}$ (the change in spin orientation between two consecutive lattice sites), a Lieb lattice with $\vec{q} = (\pi, \pi)$ is ferromagnetic within each sublattice. Moreover, because the magnetization amplitude m is the same in every site and each unit cell has two spins in the same direction and one spin in the opposite direction, the total spin per unit cell is nonzero, as predicted by Lieb [2].

From this point forward, we consider $t = 1$, so that U is given in units of t. It is important to remark that, experimentally, although we cannot directly control the value of U (the on-site interaction), we can control the ratio U/t, for example by applying pressure on the sample.

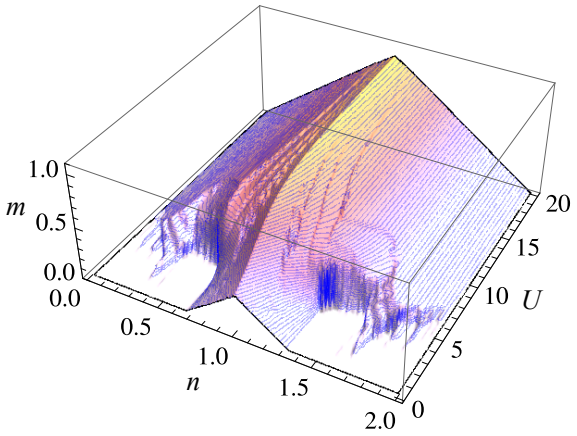

Figure 7.4: Mean-field ground state magnetization (m) of the Lieb lattice as a function of n and U. The plot is very similar to that of the 2D square lattice. The most noticeable difference between the two is that, while the square lattice has zero m in the vicinity of the point $(n, U) = (1, 0)$, the Lieb lattice has finite m in this region of the diagram, more specifically between $n = 2/3$ and $n = 4/3$.

7.3 Results and discussion

The $n - U$ phase diagram is computed in the following way. For each point (n, U), the number of electrons N is well defined, so that we can add the lowest N mean-field energies and find the total energy of the system. By numerically minimizing this total energy (using, for instance, the algorithm in Ref. [27]) with respect to q_x, q_y and m, we find the values of these three magnetic order parameters which lead to the ground state for this pair (n, U). Repeating this process for all desired pairs, one obtains the phase diagram.

7.3.1 Magnetization for high U/t

The plot in Fig. 7.4 shows the mean-field ground state magnetization amplitude m as a function of n and U. This result is similar to that of the square lattice in most regions of the diagram. Indeed, for high U, the magnetization is proportional to n between $n = 0$ and $n = 1$, and proportional to $2 - n$ between $n = 1$ and $n = 2$, reflecting particle-hole symmetry.

This proportionality can be justified analytically in the following way. For very high U, the tight-binding terms of the mean-field Hamiltonian given by Eq. 7.6 are but a small perturbation, which can be neglected as a first approximation. In this case, all sublattices become equivalent, implying $n_A = n_B = n_C = n$, with $t = 0$. Diagonalizing the new Hamiltonian gives two flat bands. A three-fold degenerate band at $\frac{U}{2}(n - m)$ and a three-fold degenerate band at $\frac{U}{2}(n + m)$. Distributing the electrons in the bands and adding up their energies, one obtains the total energy of the system by adding the diagonal term $\frac{3UL_{\text{uc}}}{4}(m^2 - n^2)$ (see Eq. 7.7), so that having positive m yields the same bands as negative m. Let us assume $m > 0$. For $n \in [0, 1]$, electrons occupy only the lowest (degenerate) energy band, with energy $\frac{U}{2}(n - m)$. The total energy is then given by

$$\frac{3UL_{\text{uc}}}{4}(m^2 - n^2) + \frac{U}{2}\sum_{N}(n - m). \tag{7.10}$$

The result of the summation is simply $N(n-m) = 3nL_{\mathrm{uc}}(n-m)$. Minimizing this with respect to m gives the expected result $m = n$. Performing an analogous calculation assuming $n > 1$ yields the relation $m = 2 - n$, i.e., the other half of the plot in Fig. 7.4 for high U.

7.3.2 Magnetization for low U/t

The results for the magnetization amplitude m in the limit $U \to 0$ can be explained using first-order perturbation theory. Let us denote by H_0 (the unperturbed Hamiltonian) the tight-binding terms of Eq. 7.6, that is, Hamiltonian H_{MF} with $U = 0$. Its eigenvalues are

$$\begin{gathered} \pm 2t\sqrt{\cos^2\tfrac{k_x}{2} + \cos^2\tfrac{k_y}{2}}, \\ \pm 2t\sqrt{\cos^2\left(\tfrac{k_x}{2} + q_x\right) + \cos^2\left(\tfrac{k_y}{2} + q_y\right)}, \end{gathered} \tag{7.11}$$

and two coincident flat bands at $\varepsilon = 0$. Using the interaction terms of Hamiltonian 7.6 as a perturbation yields, to first order, two key results. Firstly, the flat bands are split into two non-degenerate nearly flat bands. One of them is shifted to positive energy by an amount proportional to mU, while the other is shifted to negative energy, by the same amount, at each point of the Brillouin zone. Secondly, the four non-flat bands are shifted by $\frac{U}{4}(n_A + n_B)$. These two conclusions allow us to predict the behaviour of m near $U = 0$. For the following calculations, one must keep in mind that the diagonal term in Eq. 7.7 is also to be accounted for.

We begin by filling up the lower bands (which correspond to the bands with minus signs in Eq. 7.11), distributing the particles among the sublattices according to Fig. 7.2b. For n lower than $2/3$, it is best to keep $m = 0$ because, up to first order, the energy of the two lower-energy bands (associated with the Hamiltonian H_0) does not depend on m, and having finite m would only increase the total energy due to the diagonal term in Eq. 7.7. As the total particle density reaches $n \approx 2/3$ (getting closer to $2/3$ as U approaches 0), we start to fill the nearly flat bands at $\varepsilon = 0$. This is the point at which a finite m can be used to lower the energy of one of the flat bands, thus lowering the total energy of the system. After the lower flat band has been filled (note that finite U induces some modulation of the flat bands, but the argument is valid for small perturbations), we are at $n = 1$ and start filling the upper flat band. Now, it becomes advantageous to lower the value of m, so as to reduce the energy of this band. Finally, at $n \approx 4/3$, only the two higher-energy dispersive bands remain empty and between $n = 4/3$ and $n = 2$, the value of m goes back to zero, for the same reason as when filling the two lowest-energy bands.

Let us now compare these assertions with our numerical results in Fig. 7.4. At small U and far from half-filling (outside the n interval $[2/3; 4/3]$), the ground state of the system is paramagnetic ($m = 0$), coinciding with the square lattice result (see Fig. 7.5a). On the other hand, inside the interval $n \in [2/3; 4/3]$, the square lattice becomes paramagnetic (except at exactly $n = 1$, where it is antiferromagnetic, and in a very small region around $n = 1$, where a spiral phase arises; the width of this region goes to zero as $U/t \to \infty$) while our result suggests that the Lieb lattice has a magnetic ordering other than paramagnetism. To know which ordering it is, one needs to look at the results for q_x and q_y.

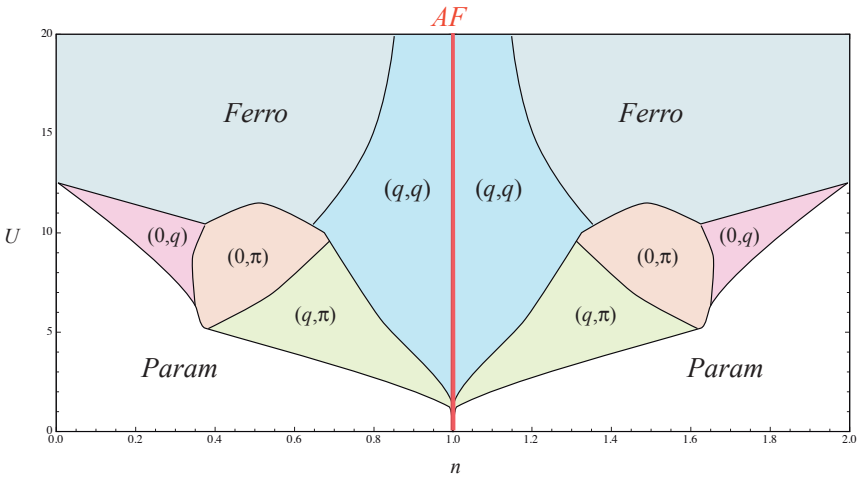

(a)

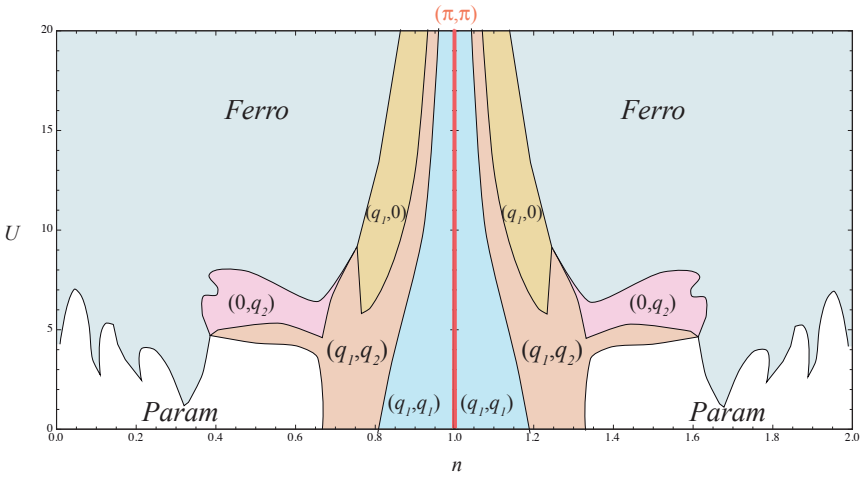

(b)

Figure 7.5: Mean-field magnetic phase diagrams of (a) the square lattice and (b) the Lieb lattice. In the case of the square lattice, the value of q varies continuously in the range $[0, \pi]$, in each region labelled as such. In the case of the Lieb lattice, $q_1 \approx \pi$ and $q_2 \approx \pi/2$, and the transitions between regions labelled using q_1 or q_2 are discontinuous.

7.3.3 Magnetic ordering

Fig. 7.5 shows both the mean-field magnetic phase diagram of the Lieb lattice (bottom plot) and that of the square lattice (top plot), for comparison. The phase diagrams were computed using the independent variables n and U, in the range $(n, U) \in [0, 2] \times [0, 20]$, and were obtained by joining the results for the three order parameters: q_x, q_y and m. Near $n = 0$ and $n = 2$, the system is ferromagnetic for large U and paramagnetic for low U, like the square lattice, albeit with a wider ferromagnetic region. At intermediate U and n near 0.5 or 1.5, the system displays a $(0, q_2)$ spiral phase, characterized by $q_2 \approx \pi/2$.

The spiral phase characterized by $\vec{q} = (\pi, \pi)$ only occurs at exactly $n = 1$, for any U, as in the square lattice. In the latter, this would be called antiferromagnetism. Nonetheless, in the Lieb lattice, a (π, π) phase should be identified with ferrimagnetic ordering [2, 18] (see Fig. 7.3). Indeed, the spin-spin correlation in a (π, π) phase is ferromagnetic in each sublattice, but antiferromagnetic between different sublattices. The total spin per unit cell is finite, because m is finite at half-filling (see Fig. 7.4) and the number of sites per unit cell is odd.

When slightly doped away from half-filling ($0.95 \lesssim n \lesssim 1.05$), both q_x and q_y continuously deviate from π and become a (q_1, q_1) phase with $q_1 \approx \pi$. This area becomes narrower in the n direction as U grows larger. This phase can be interpreted as a $(\pi - \delta, \pi - \delta)$ phase with small δ, that is, a local (looking at only a few unit cells) ferrimagnet with a slow modulation in the direction of spins along the lattice. At large U, when further doped, the system undergoes a first-order phase transition from $\vec{q} \approx (\pi, \pi)$ to $\vec{q} \approx (q_1, q_2)$ with $q_2 \approx \pi/2$, reflecting local antiferromagnetic correlations in the x direction, and sublattice-wise antiferromagnetism in the y direction. In other words, each sublattice is ferromagnetic in the x direction and antiferromagnetic in the y direction. If doped even further away from half-filling, two more first-order phase transitions occur: first to $(q_1, 0)$ and finally to $(0, 0)$ (ferromagnetism). At regular intervals in n (namely 0.11, 0.22, 0.33 and their symmetric counterparts), we find ferromagnetic dips into the paramagnetic region. These can most likely be explained using the symmetry of the lattice and higher-order corrections.

7.4 Conclusion

In summary, we have computed and analysed the n-U mean-field magnetic phase diagram of the Lieb lattice, and compared it to that of the square lattice. Far from half-filling, the two phase diagrams display ferromagnetism [$\vec{q} = (0, 0)$] for high U and paramagnetism ($m = 0$) for low U, while at exactly half-filling (one electron per lattice site) the ground state is a (π, π) spiral phase for both lattices.

Although the diagrams coincide at $n = 1$, it is close to that line that their most remarkable differences arise. In fact, at large U, as we move away from half-filling [(the (π, π) phase)], the Lieb lattice undergoes three first-order phase transitions $(\pi, \pi) \to (\pi, \pi/2) \to (\pi, 0) \to (0, 0)$, unlike in the case of the square lattice, where the transition from antiferromagnetism to ferromagnetism is continuous in $\vec{q}$. On the other hand, near the tight-binding limit and within the interval $n \in [2/3, 4/3]$, the magnetization of the Lieb lattice is finite and the ground state is characterised by spin spirals, contrasting with the paramagnetic ordering of the square lattice in this region of the diagram.

Our numerical results are in agreement with a theorem by Lieb [2], which applies to Hubbard models which comprise sublattices with different number of sites (in our case, we have twice as many B/C sites as we have A sites). The theorem states that the ground state

of such a system at half-filling is ferrimagnetic [18]. According to our results, the ground state at half-filling is characterized by $\vec{q} = (\pi, \pi)$ and finite m, which translates into ferromagnetic sublattices and finite total spin on each unit cell (see Fig. 7.3), which is qualitatively consistent with the theorem. According to this theorem, however, the total magnetization per unit cell in the Lieb lattice at half-filling should be 1 for any U. Our mean-field approach yields that value as U grows large but deviates from 1 at low U (see Fig. 7.4). On the other hand, this theorem is also applicable to a square lattice Hubbard model if one divides the lattice into two sublattices. This has been done before [26] with a square lattice divided into two sublattices, A and B, with the same number of sites each. In consonance with the aforementioned theorem by Lieb, this square lattice has zero total spin per unit cell at half-filling, for any U, regardless of m being zero or not. Therefore, it stands to reason to conjecture that the mean-field calculations performed for the square lattice also return wrong values for m at low U, even though the correct values cannot be deduced from Lieb's theorem, as it only predicts the total spin per unit cell.

The disparity between our mean-field results at half-filling and the prediction of Lieb's theorem may be due to two important restrictions that we imposed in order to simplify our calculations. Firstly, we assumed that the occupation numbers for any U remain the same as in the tight-binding limit ($U = 0$), and secondly, we assumed that the magnetization is the same on every sublattice. If it turns out that these two assumptions are indeed the reason for the discrepancy, that is, if the Lieb's theorem can be satisfied in a mean-field approach applied to this paper's model, albeit with more relaxed constraints, such a result should be taken into account in any other mean-field study of interacting fermions in bipartite lattices or even more complex lattices whose unit cells contain more than two types of atoms. This is an open question that we intend to address in the future.

References

[1] M. Dzierzawa. "Hartree-Fock theory of spiral magnetic order in the 2-d Hubbard model". *Z. Phys. B* 86 (1992), pp. 49–52.

[2] E. H. Lieb. "Two Theorems on the Hubbard model". *Physical Review Letters* 62 (1989), pp. 1201–1204.

[3] J. G. Bednorz and K. A. Müller. "Possible high T_c superconductivity in the Ba-La-Cu-O system". *Zeitschrift fur Physik B Condensed Matter* 64 (1986), pp. 189–193.

[4] M. A. Kastner et al. "Magnetic, transport, and optical properties of monolayer copper oxides". *Rev. Mod. Phys.* 70 (1998), pp. 897–928.

[5] H. Bethe. "Zur Theorie der Metalle". *Zeitschrift für Physik* 71 (1931), pp. 205–226.

[6] R. G. Dias and J. M. B. Lopes dos Santos. "Simple representation of the eigenstates of the $U \to \infty$ one-dimensional Hubbard model". *Journal de Physique I* 2 (1992), pp. 1889–1897.

[7] M. P. Marder. *Condensed Matter Physics*. John Wiley and Sons, 2000.

[8] P. R. Wallace. "The Band Theory of Graphite". *Physical Review* 71 (1947), pp. 622–634.

[9] A. Mielke. "Exact ground states for the Hubbard model on the Kagome lattice". *Journal of Physics A* 25 (1992), p. 4335.

[10] H. Tasaki. "Ferromagnetism in the Hubbard Models with Degenerate Single-Electron Ground States". *Physical Review Letters* 69 (1992), pp. 1608–1612.

[11] H. Tamura, K. Shiraishi, and H. Takayanagi. "Ferromagnetism in Semiconductor Dot Array". *Jpn. J. Appl. Phys.* 39 (2000), p. L241.

[12] N. Goldman, D. F. Urban, and D. Bercioux. "Topological phases for fermionic cold atoms on the Lieb lattice". *Phys. Rev. A* 83 (2011), p. 063601.

[13] H. Wang, S.-L. Yu, and J.-X. Li. "Spin fluctuations and unconventional pairing on the Lieb lattice". *Physics Letters A* 378.45 (2014), pp. 3360–3365.

[14] V. J. Emery. "Theory of high-T_c superconductivity in oxides". *Physical Review Letters* 58 (1987), pp. 2794–4797.

[15] R. T. Scalettar et al. "Antiferromagnetic, charge-transfer and pairing correlations in the three-band Hubbard model". *Physical Review B* 44 (1991), pp. 770–781.

[16] C. Weeks and M. Franz. "Topological insulators on the Lieb and perovskite lattices". *Physical Review B* 82 (2010), p. 085310.

[17] H. Tamura, K. Shiraishi, and H. Takayanagi. "Semiconductor Ferromagnetism in Quantum Dot Array". *physica status solidi (b)* 224 (2001), pp. 723–725.

[18] A. Mielke and H. Tasaki. "Ferromagnetism in the Hubbard model". *Communications in Mathematical Physics* 158.2 (1993), pp. 341–371.

[19] K. Noda, K. Inaba, and M. Yamashita. "Flat-band ferromagnetism in the multilayer Lieb optical lattice". *Phys. Rev. A* 90 (2014), p. 043624.

[20] S. Sarker et al. "Spiral states in the square-lattice Hubbard model". *Phys. Rev. B* 43 (1991), pp. 8775–8778.

[21] E. Langmann and M. Wallin. "Mean Field Magnetic Phase Diagrams for the Two Dimensional $t - t' - U$ Hubbard Model". *Journal of Statistical Physics* 127 (2007), pp. 825–840.

[22] P. A. Igoshev et al. "Incommensurate magnetic order and phase separation in the two-dimensional Hubbard model with nearest- and next-nearest-neighbor hopping". *Phys. Rev. B* 81 (2010), p. 094407.

[23] W. Schumacher. "On incommensurate phases in the magnetic phase diagram of the hubbard model". *physica status solidi (b)* 119.1 (1983), pp. 235–238.

[24] M. Nita, B. Ostahie, and A. Aldea. "Spectral and transport properties of the two-dimensional Lieb lattice". *Physical* 87 (2013), p. 125428.

[25] A. Singh, Z. Tesanovic, and H. H. Kim. "Instability of the spiral state of the doped Hubbard model". *Pramana - J. Phys.* 38 (1992), pp. 211–217.

[26] J. D. Gouveia and R. G. Dias. "Spiral ferrimagnetic phases in the two-dimensional Hubbard model". *Solid State Communications* 185 (2014), pp. 21–24.

[27] J. C. Lagarias et al. "Convergence Properties of the Nelder-Mead Simplex Method in Low Dimensions". *SIAM Journal of Optimization* 9 (1998), pp. 112–147.

Chapter 8

Spin and charge density waves in the Lieb lattice

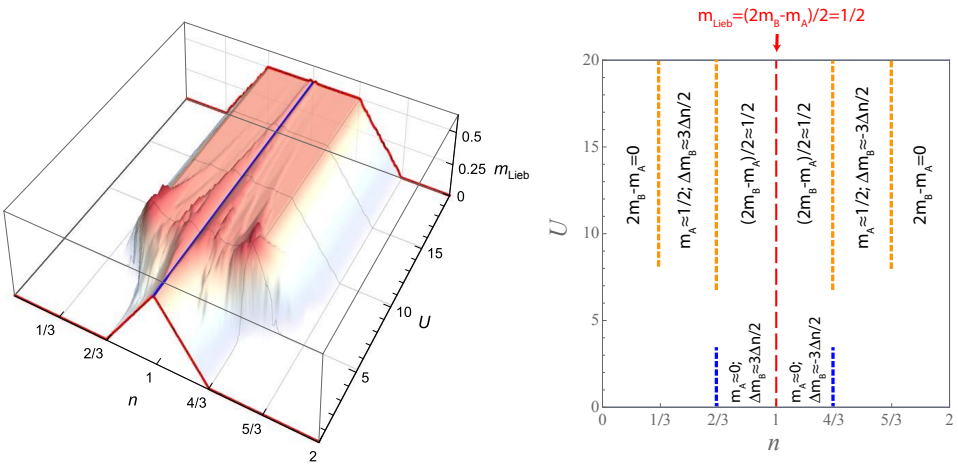

Adapted from:
J. D. Gouveia and R. G. Dias, Spin and charge density waves in the Lieb lattice. Journal of Magnetism and Magnetic Materials, Volume 405, 1 May 2016, Pages 292-303
DOI: 10.1016/j.jmmm.2015.12.096

Abstract

We study the mean-field phase diagram of the two-dimensional (2D) Hubbard model in the Lieb lattice allowing for spin and charge density waves. Previous studies of this diagram have shown that the mean-field magnetization surprisingly deviates from the value predicted by Lieb's theorem [1] as the on-site repulsive Coulomb interaction (U) becomes smaller [2]. Here, we show that in order for Lieb's theorem to be satisfied, a more complex mean-field approach should be followed in the case of bipartite lattices or other lattices whose unit cells contain more than two types of atoms. In the case of the Lieb lattice, we show that, by allowing the system to modulate the magnetization and charge density between sublattices, the difference in the absolute values of the magnetization of the sublattices, m_{Lieb}, at half-filling, saturates at the exact value $1/2$ for any value of U, as predicted by Lieb. Additionally, Lieb's relation, $m_{\mathrm{Lieb}} = 1/2$, is verified approximately for large U, in the $n \in [2/3, 4/3]$ range. This range includes not only the ferromagnetic region of the phase diagram of the Lieb lattice (see Ref. [2]), but also the adjacent spiral regions. In fact, in this lattice, below or at half-filling, m_{Lieb} is simply the filling of the quasi-flat bands in the mean-field energy dispersion both for large and small U.

8.1 Introduction

Despite intense research in the last few decades, the 2D Hubbard model in the square lattice has remained an open theoretical problem in the field of the strong correlated systems [3, 4]. Although it is known that at half-filling, the spin dynamics of the 2D Hubbard model is described by the Heisenberg antiferromagnetic exchange term [5], there is no consensus regarding the ground state magnetic phase diagram of this model. In fact, even at the mean-field (MF) level, depending on the magnetic phases allowed, different authors obtain different diagrams for the square lattice [6]. The traditional orderings are ferromagnetism, antiferromagnetism and paramagnetism [7–11]. Later, spin spiral phases, a generalization of the previous three, were introduced [12]. The MF phase diagram became even more complex with the consideration of spatial phase separation [13–15].

The Hubbard model in decorated 2D lattices has also been extensively studied, motivated by the search for metallic (flat-band) ferromagnetism. These decorated lattices fall into three categories: the Lieb [1], Mielke [16] and Tasaki lattices [17]. All of these lattices share a common feature: the presence of flat bands in the energy dispersion relation. In the particular case of the Lieb's lattices, the flat bands result from the topology of the lattice, while in the case of Mielke and Tasaki lattices, the flat bands reflect longer-range transfer integrals in the system. One of the most representative examples of decorated lattices is the Lieb lattice, which can be obtained from the 2D square lattice, for example, by inserting an extra atom between every two nearest-neighbours (see Fig. 8.1a). Each unit cell (shaded rectangle in Fig. 8.1a) has 3 atoms, one of each kind: A, B and C, whose relative occupation is depicted in Fig. 8.1b, in the limit of no interactions. Fig. 8.1c shows the energy bands of the Lieb lattice in this limit. Examples of materials whose structure resembles the Lieb lattice include $La_{2-x}Sr_xCuO_4$ and $YBa_2Cu_3O_7$, two well-known high-T_c superconductors with weakly coupled CuO_2 planes [18, 19].

A theorem by Lieb [1] states that, in the particular case of bipartite lattices (i.e., lattices with two sublattices, A and B, such that each site on sublattice A has its nearest neighbors on sublattice B, and vice versa), the ground state is ferromagnetic at half-filling ($n = 1$, or one electron per lattice site), as long as the number of atoms of each sublattice is different. However, for example in the case of the Lieb lattice (a line-centered square lattice [20]), this ground state should be identified with ferrimagnetism [21]. In fact, although each sublattice is indeed ferromagnetic, there is antiferromagnetic ordering between every pair of nearest neighbours [2] (see Fig. 8.1a).

The magnetic phase diagram of the Hubbard model in the Lieb lattice was recently studied by us [2]. We showed that the mean-field magnetization per unit cell at half-filling, $m_{\text{Lieb}} = (|m_B| + |m_C| - |m_A|)/2$, assuming the particle density (n) of the tight-binding limit (see Fig. 8.1b) and the same magnetization (m) in the whole lattice, surprisingly deviates from the value predicted by Lieb's theorem [1] as the on-site repulsive Coulomb interaction (U) becomes smaller, although these two assumptions are common in mean-field studies [2, 22–25]. Lieb's theorem predicts that the magnetization per unit cell, m_{Lieb}, is $1/2$ for any U at half-filling. Fig. 8.2 shows both the mean-field phase diagram of the Hubbard model in the Lieb lattice, and the value of m_{Lieb}, using the mean-field results from Ref. [2]. For the results to agree with Lieb's theorem, one should have $m_{\text{Lieb}} = 1/2$ for any U. Although in the strong coupling limit ($U \gg t$), the mean-field result satisfies Lieb's theorem, it is far from correct near the tight-binding limit ($U = 0$).

In this manuscript, we study the magnetic phase diagram of the Lieb lattice allowing

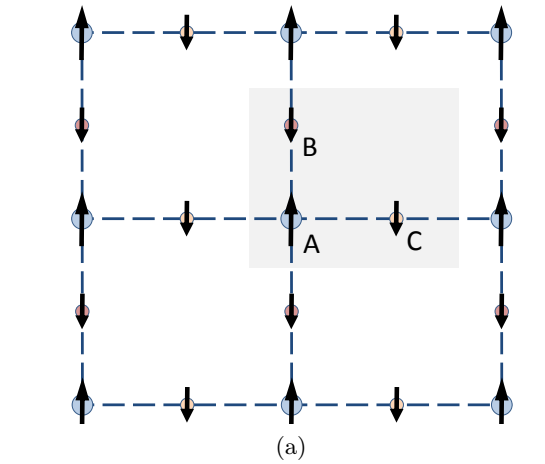

(a)

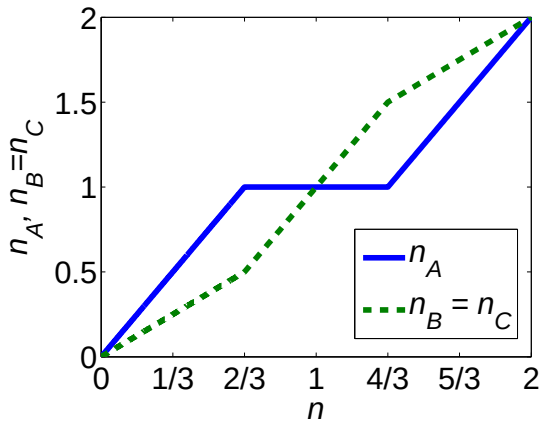

(b)

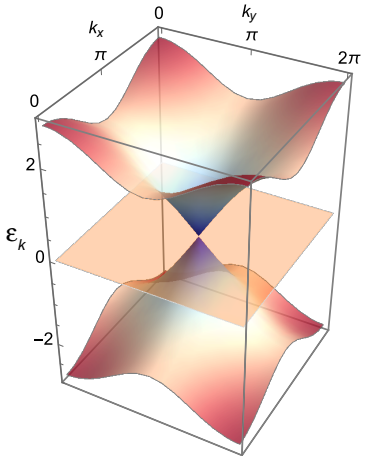

(c)

Figure 8.1: (a) The Lieb lattice is a line-centered square lattice, comprising three sublattices, A, B, and C and having one atom of each type in a unit cell. The circles represent atomic nuclei and the arrows represent spins. At half-filling, the Lieb lattice is ferromagnetic within each sublattice but antiferromagnetic overall. Moreover, at half-filling, the total spin per unit cell is 1/2, as predicted by Lieb [1]. (b) Plot of the tight-binding ($U = 0$) particle density of each sublattice of the Lieb lattice, A, B or C, as a function of the total particle density. (c) Plot of the tight-binding dispersion relation $\varepsilon(k_x, k_y)$ of the Lieb lattice. The flat band is made up entirely of B and C orbitals.

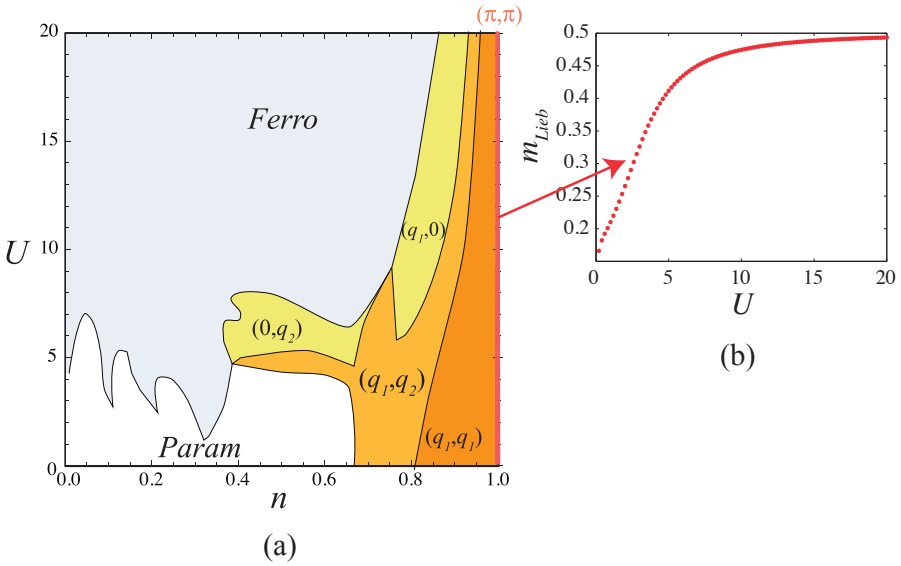

Figure 8.2: (a) Mean-field magnetic phase diagram of the Hubbard model in the Lieb lattice, obtained in Ref. [2] and (b) difference in the absolute values of the magnetization of the sublattices, $m_{\text{Lieb}} = (|m_B| + |m_C| - |m_A|)/2$, of the Lieb lattice at half-filling, using the mean-field results from the same reference, where the on-site magnetization is assumed to be the same on all sublattices.

for different average occupations (n_A, n_B, and n_C) and magnetization amplitudes (m_A, m_B, and m_C) in each sublattice. We find that with these new considerations, Lieb's relation, $m_{\text{Lieb}} = 1/2$, is satisfied for any U at half-filling, and satisfied approximately for large U, in the $n \in [2/3, 4/3]$ range, which includes not only the ferromagnetic region of the phase diagram of the Lieb lattice in Fig. 8.2, but also the adjacent spiral regions (note that, away from half-filling, m_{Lieb} is no longer the unit cell magnetization, but gives the difference in the absolute values of the magnetization of the sublattices). An important point in this result is that finite m_{Lieb} reflects the existence of quasi-flat bands in the mean-field energy dispersion. These quasi-flat bands are present, not only for small U, but also for large U. In fact, below or at half-filling, m_{Lieb} is approximately the filling of the flat bands both for large and small U.

Our mean-field approach follows that of Bach and Poelchau[26] (see also Refs. [13, 27]). The formalism with further mathematical details can be found in Ref. [28].

The organization of this paper is as follows. We begin by presenting some key results for the Hubbard model and mean-field. Secondly, we revisit the tight-binding limit of the Lieb lattice. We then proceed to adding electronic interactions to the Hamiltonian and calculating its mean-field counterpart. Finally, we show our results, discuss their meaningfulness, compare them to analytical calculations and take conclusions. In Appendix A, we briefly outline the derivation which leads to the results in section II, and in Appendix B, we explain in more detail our method of calculating saddle points, which we used to obtain the results in section V.

8.2 Mean-field method for the Hubbard model

In this section, we adapt a key result presented as Theorem 4.14 in Ref. [28]. This derivation was first done by Lieb and his colaborators [27] and simplified by Bach and Poelchau [26]; in Appendix A we show an adaptation of the derivation in Ref. [26]. Alternative approaches can be found in Refs. [25] and [29]. The result consists of the following abridged derivation.

We begin with the Hubbard Hamiltonian, given by

$$H = t \sum_{\langle x,y\rangle,\sigma} c^{\dagger}_{x,\sigma} c_{y,\sigma} + U \sum_{x} \hat{n}_{x,\uparrow}\hat{n}_{x,\downarrow}. \tag{8.1}$$

Here, t is the hopping parameter between nearest neighbours and $c^{\dagger}_{x,\sigma}$ ($c_{y,\sigma}$) is the creation (annihilation) operator of an electron on site x (y) with spin $\sigma =\uparrow,\downarrow$. The letters x and y denote lattice sites, $\langle x,y\rangle$ stands for nearest neighbors and U is the on-site repulsive. The total number of particles is N.

With the intent of finding the mean-field Helmholtz free energy, F_{HF}, associated to this Hamiltonian (note that we use F because we work with fixed number of particles; if we worked with fixed chemical potential, we would use the grand canonical potential instead), we first replace the interaction term, $\hat{n}_{x,\uparrow}\hat{n}_{x,\downarrow}$, with the Hartree and Fock terms,

$$\begin{aligned}\hat{n}_{x,\uparrow}\hat{n}_{x,\downarrow} \to \hat{n}_{x,\uparrow}\langle\hat{n}_{x,\downarrow}\rangle + \langle\hat{n}_{x,\uparrow}\rangle\hat{n}_{x,\downarrow} - \langle\hat{n}_{x,\uparrow}\rangle\langle\hat{n}_{x,\downarrow}\rangle \\ - c^{\dagger}_{x,\uparrow}c_{x,\downarrow}\langle c^{\dagger}_{x,\downarrow}c_{x,\uparrow}\rangle - \langle c^{\dagger}_{x,\uparrow}c_{x,\downarrow}\rangle c^{\dagger}_{x,\downarrow}c_{x,\uparrow} + \langle c^{\dagger}_{x,\uparrow}c_{x,\downarrow}\rangle\langle c^{\dagger}_{x\downarrow}c_{x,\uparrow}\rangle.\end{aligned} \tag{8.2}$$

Replacing the averages by the mean-field parameters $\vec{m}$ and n (see Appendix A for details), it follows that the mean-field Hamiltonian, $H(\vec{m},n)$, corresponding to the Hamiltonian in Eq. 8.1 is

$$H(\vec{m},n) = t \sum_{\langle x,y\rangle,\sigma} c^{\dagger}_{x,\sigma} c_{y,\sigma} + U \sum_{x} \left[\frac{1}{4}\left(\vec{m}_x^2 - n_x^2\right) + \frac{1}{2}\left(n_x\hat{n}_x - \vec{m}_x\cdot\hat{\vec{s}}_x\right)\right], \tag{8.3}$$

where $\hat{\vec{s}}_x$ and $\hat{n}_x$ are the spin and electron density operators at the site x, and $\vec{m}_x$ and n_x are the respective mean-field parameters.

The Helmholtz free energy $F(\vec{m},n)$ is calculated from $H(\vec{m},n)$ using the partition function, $Z(\vec{m},n)$,

$$\begin{aligned}F(\vec{m},n) &= -\frac{1}{\beta}\ln Z(\vec{m},n) = -\frac{1}{\beta}\ln\left(\mathrm{Tr}\left(e^{-\beta H(\vec{m},n)}\right)\right) \\ &= -\frac{1}{\beta}\mathrm{Tr}\left(\ln\left(1+e^{-\beta h}\right)\right) + \frac{U}{4}\sum_{x}\left(\vec{m}_x^2 - n_x^2\right),\end{aligned} \tag{8.4}$$

where

$$h_{x\sigma y\sigma'} = t\delta_{\sigma\sigma'} + \frac{U}{2}\left(n_x\delta_{\sigma\sigma'} - \vec{m}_x\cdot\vec{\sigma}_{\sigma\sigma'}\right)\delta_{xy}, \tag{8.5}$$

Here, $\vec{\sigma}_{\sigma\sigma'}$ is the vector of Pauli matrices.

The important result is that in the Hubbard model, the minimum of the Helmholtz free energy, F_{HF}, corresponds to a saddle point of its mean-field counterpart, $F(\vec{m},n)$,

$$F_{\mathrm{HF}} = \min_{\vec{m}}\max_{n} F(\vec{m},n). \tag{8.6}$$

See Appendix A for a detailed discussion of the above relation.

Computing the partial derivatives of $F(\vec{m}, n)$ with respect to $\vec{m}$ and n and setting them equal to zero, we find the self-consistency relations $n_x = \langle \hat{n}_x \rangle$ and $\vec{m}_x = \langle \hat{\vec{s}}_x \rangle$. In the case of the Hubbard model, solving the Hartree-Fock equations self-consistently is actually equivalent to finding a saddle point of the mean-field energy, $F(\vec{m}, n)$. If one fixes the particle density, n on all sites of the lattice, then the mean-field calculation is reduced to finding a minimum of the mean-field energy with respect to the spin density, $\vec{m}$. Note that these results are for finite temperatures, but they are still valid in the limit $T \to 0$ in the case of the Hubbard model, as shown in Ref. [26].

References [13] and [28] go on to apply Eq. 8.6 to the computation of a mean-field magnetic phase diagram of the Hubbard model in the square lattice, imposing two restrictions that we do not adopt in this work. Namely, they restrict magnetic phases to ferromagnetic (F), antiferromagnetic (AF), and paramagnetic (P), and additionally impose homogeneous particle density throughout the square lattice, in which case the extremization of the free energy given in Eq. 8.6 is reduced to a minimization problem. However, in the case of the Lieb lattice, charge modulation occurs even in the tight-binding limit. For a mean-field calculation to yield the correct result in the tight-binding limit, this charge modulation needs to be taken into account. To the extent of our knowledge, this work is the first application of the result in Eq. 8.6 which uses both n and $\vec{m}$ to extremize $F(\vec{m}, n)$. To accomplish this, we use the generalized HF theory, which turns the original minimization problem for the Helmholtz free energy F into a saddle-point problem for the mean-field Helmholtz free energy $F(\vec{m}, n)$ (see Appendices).

8.3 The Lieb lattice in the tight-binding limit

The Lieb lattice is a square lattice, with a quarter of its atoms removed in a regular pattern. Introducing a different creation operator in each sublattice, $A^\dagger$, $B^\dagger$, and $C^\dagger$, the tight-binding term of the Hamiltonian of such a model, H_t, is given by [30]

$$\begin{aligned} t \sum_{x=1}^{L_x} \sum_{y=1}^{L_y} \Big[& (A^\dagger_{x,y} B_{x,y} + A^\dagger_{x,y} C_{x,y} + \text{H.c.}) \\ & + (A^\dagger_{x,y} B_{x,y-1} + A^\dagger_{x,y} C_{x-1,y} + \text{H.c.}) \Big] . \end{aligned} \tag{8.7}$$

L_x (L_y) is the number of unit cells along the x (y) direction. The hopping terms in the first line are intra-unit cell and the remaining are inter-unit cell. Its eigenvalues originate three energy bands, one of which is flat. The dispersion relation for periodic boundary conditions is

$$\varepsilon_\pm = \pm 2t \sqrt{\cos^2 \frac{k_x}{2} + \cos^2 \frac{k_y}{2}}, \tag{8.8}$$

for the two non-flat energy bands, where $k_\alpha = 2\pi n_\alpha / L_\alpha$ with $n_\alpha = 0, 1, \cdots, L_\alpha$ and $\alpha \in \{x, y\}$. The flat band is $L_x \times L_y$-fold degenerate with zero energy. These three energy bands are shown in Fig. 8.1c. The three branches intersect at the point $(k_x, k_y) = (\pi, \pi)$. Expanding the dispersion relation in Eq. 8.8 around this momentum, we find the Dirac cones $\varepsilon^2 = t^2(k_x^2 + k_y^2)$. The flat band is built up from B- and C-type orbitals, while the lower and upper bands involve all three lattices A, B, and C. This lack of uniformity in the distribution of the sublattices in the energy bands justifies the difference in the occupation numbers of the sublattices presented in Fig. 8.1b.

8.4 Interactions and mean-field

In this section, we add interactions to the tight-binding Hamiltonian of the Lieb lattice, H_t, and reduce the quartic dependance of the resulting Hamiltonian on the creation and destruction operators to a quadratic one, using the mean-field approximation [12].

The key difference between our approach and previous approaches is that we allow sublattices A, B, and C to have a different average occupation number each, while keeping the total number of particles of the system, N, fixed [on each point of the (n, U) phase diagram]. We begin by defining an average particle density on each sublattice,

$$\begin{aligned} n_A &= n + \delta_A \\ n_B &= n + \delta_B \\ n_C &= n + \delta_C, \end{aligned} \tag{8.9}$$

along with the number of particles on each sublattice. For sublattice A, this would be $N_A = n_A L$, where $L = L_x L_y$ is the number of unit cells (which in turn equals the number of sites A). To keep the number of particles equal to N, we apply the restriction $N_A + N_B + N_C = N$, which is equivalent to

$$\delta_A + \delta_B + \delta_C = 0. \tag{8.10}$$

Setting $\delta_A = \delta_B = \delta_C = 0$, we would obtain a lattice with its particles evenly distributed, which is what happens in the usual 2D square lattice: all sites have the same particle density. Aside from total particle number conservation (Eq. 8.10) and motivated by the symmetry of the lattice, we impose is that $\delta_B = \delta_C$. This gives the important relation $\delta_B = \delta_C = -\delta_A/2 \Rightarrow n_B = \frac{1}{2}(3n - n_A)$, which leaves us with one unknown with respect to which $F(\vec{m}, n)$ needs to be maximized. We chose to maximize with respect to δ_A.

In our case, we work at $T = 0$, so that the mean-field free energy of the system can be found by summing the mean-field energies of the lowest levels that the N particles can occupy (this is the usual Fermi sea). On each point (n, U), the total energy of the system, E_{HF}, is obtained by adding the lowest N eigenvalues of the mean-field Hamiltonian H_{HF} [2, 23, 24, 31],

$$H_{\mathrm{HF}} = \begin{pmatrix} H_t(\vec{k}) + H_\delta & H_m \\ H_m^\dagger & H_t(\vec{k} + 2\vec{q}) + H_\delta \end{pmatrix}, \tag{8.11}$$

and then adding the diagonal terms

$$\frac{UL}{4}(m_A^2 + m_B^2 + m_C^2 - (n + \delta_A)^2 - (n + \delta_B)^2 - (n + \delta_C)^2). \tag{8.12}$$

The smaller matrices that compose the Hamiltonian H_{HF} are

$$H_t(\vec{k}) = \begin{pmatrix} 0 & t(1 + e^{ik_y}) & t(1 + e^{ik_x}) \\ t(1 + e^{-ik_y}) & 0 & 0 \\ t(1 + e^{-ik_x}) & 0 & 0 \end{pmatrix}, \tag{8.13}$$

$$H_\delta = \frac{U}{2} \begin{pmatrix} n + \delta_A & 0 & 0 \\ 0 & n + \delta_B & 0 \\ 0 & 0 & n + \delta_C \end{pmatrix}, \tag{8.14}$$

and

$$H_m = -\frac{U}{2}\begin{pmatrix} m_A & 0 & 0 \\ 0 & m_B e^{iq_y} & 0 \\ 0 & 0 & m_C e^{iq_x} \end{pmatrix}. \tag{8.15}$$

The matrix H_{HF} above is written in the basis $\{A_{\vec{k}}, B_{\vec{k}}, C_{\vec{k}}, A_{\vec{k}+2\vec{q}}, B_{\vec{k}+2\vec{q}}, C_{\vec{k}+2\vec{q}}\}$, where the vector $\vec{q} = (q_x, q_y)$ defines the spin orientation in the system, as in the works by Dzierzawa [24] and Singh [31]. In this paper, we assume that the spin spiral wavenumber $\vec{q}$ remains the same as in Ref. [2], even though we allow the system to have spin and charge modulation. $H_t(\vec{k})$ is the matrix that corresponds to the tight-binding term of the Hamiltonian. All other terms have correspondence with the interaction terms of the Hamiltonian in Eq. 8.3. Namely,

$$\begin{aligned}
&\tfrac{U}{4}\sum_x \vec{m}_x^2 \to \tfrac{UL}{4}(m_A^2 + m_B^2 + m_C^2),\\
&\tfrac{U}{4}\sum_x n_x^2 \to \tfrac{UL}{4}((n+\delta_A)^2 + (n+\delta_B)^2 + (n+\delta_C)^2),\\
&\tfrac{U}{2}\sum_x n_x \hat{n}_x \to \tfrac{U}{2}\mathrm{diag}(n+\delta_A, n+\delta_B, n+\delta_C) = H_\delta,\\
&-\tfrac{U}{2}\sum_x \vec{m}\cdot\hat{\vec{s}}_x \to -\tfrac{U}{2}\mathrm{diag}(m_A, m_B e^{iq_y}, m_C e^{iq_x}) = H_m.
\end{aligned} \tag{8.16}$$

The extra imaginary coefficients involving components of $\vec{q}$ arise from coupling sites on unit cells other than the cell labelled as (x, y). From this point forward, we consider $t = 1$, so that U is given in units of t.

8.5 Results and discussion

Our results consist of the values of m_A, m_B and n_A which, for each pair $(n, U) \in [0, 2] \times [0, 20]$, correspond to a saddle point of E_{HF}, the mean-field energy of the Lieb lattice (see Appendix B for a more detailed explanation on how to find these saddle points). From these three quantities, we can calculate $m_C = m_B$, and $n_B = n_C = \frac{1}{2}(3n - n_A)$. We do not impose different occupation or magnetization, we simply let the system choose the values which lead to a saddle point of the mean-field energy. Before performing the calculations for the Lieb lattice, we tested the algorithm for the Hubbard model in a square lattice and found that the occupations of all four sublattices (A, B, C, and D) were the same, i. e., $\delta_A = \delta_B = \delta_C = \delta_D = 0$, while the system chose to have two different magnetizations, $m_A = m_D$ and $m_B = m_C$, reproducing our results in Ref. [23].

The results for the Lieb lattice are in Fig. 8.3. In the following subsections, we discuss each region of interest in more detail. In particular, we study the low U and high U regions separately, and finally the near-half-filling region ($n \approx 1$).

8.5.1 Results near the tight-binding limit ($U \to 0$)

As expected, for low U, the average occupations of the sublattices, n_A and $n_B = n_C$ (Figs. 8.3a and 8.3b, respectively), approach those of the tight-binding limit, described in section 8.3 and plotted in Fig. 8.1b. As for the magnetization amplitudes, sublattice A is paramagnetic ($m_A = 0$) for any n and sublattice B displays a behaviour similar to that of m in Ref. [2] for

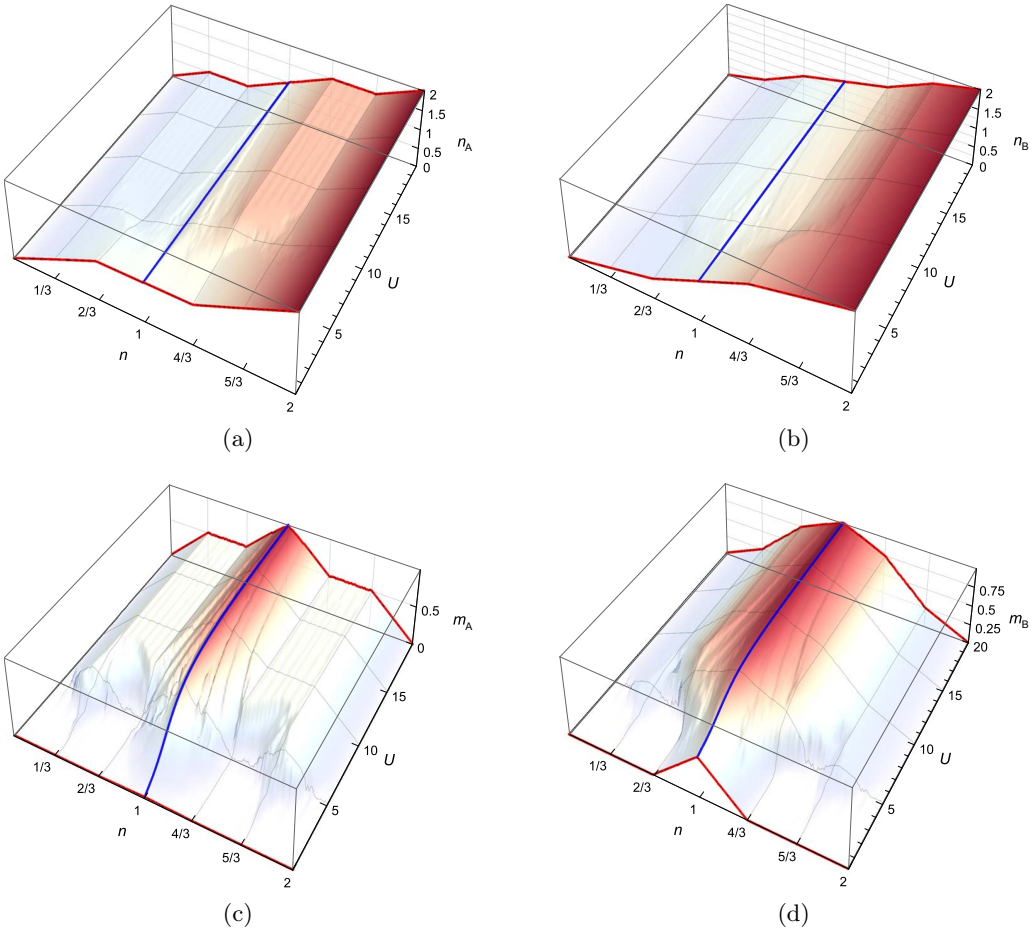

Figure 8.3: Raw numerical results of our mean-field approach, namely for (a) n_A, (b) n_B, (c) m_A and (d) m_B. The bold red lines highlight the $U = 0$ and $U = 20$ edges of the plots, and the bold blue line at the center of each plot allows a clearer visualization of each plot at half-filling ($n = 1$).

low U. In other words, m_B is finite between $n = 2/3$ and $n = 4/3$ and zero otherwise. As explained below, this difference is due to the fact that the flat band only involves B and C orbitals. A first-order perturbation analysis follows, explaining this result.

Without the U perturbation, the system becomes a Lieb lattice without electron-electron interactions and displays the electronic density in Fig. 8.1b. The energy dispersion relation comprises three bands, as in Fig. 8.1c, which can be doubly occupied with no additional energy cost (because of the absence of U). Keep in mind that the dispersive bands comprise A-, B-, and C-type orbitals, while the flat band comprises only B- and C-type orbitals. The introduction of the repulsive first-order perturbation modifies the total energy of the system by shifting the energy bands and adding the diagonal terms of Eq. 8.12. The dispersive bands are shifted by $+\frac{U\delta_A}{8}$ and the flat band is shifted by $-\frac{U\delta_A}{4}$. Additionally, the flat band (which used to have zero energy) splits into two bands, separated by an amount proportional to Um_B.

At zero filling, the energy bands are in their original ($U = 0$) position, because all δ and m are set to zero (having at least one finite m would lead to higher energy due to the term

in Eq. 8.12). As we insert electrons in the system, they occupy the lowest states in the lower dispersive band, with $n_A = 2n_B = 2n_C$. Due to the perturbation, this slowly causes the flat band to shift to lower energy and the dispersive bands to shift to higher energy. Note that before the filling $n \approx 2/3$, the system is able to have the lowest energy by displaying paramagnetism ($m_A = m_B = 0$), because, to first order, the only dependance of the energy on m is in the diagonal term of Eq. 8.12. This dependance is maintained for any n, in the case of m_A. At $n \approx 2/3$, the lower dispersive band is almost full and, due to the flat bands having shifted by the small amount $-\frac{U\delta_A}{4}$, electrons begin to occupy the flat bands, rather than the dispersive bands. From here on, up to $n = 1$, the magnetization amplitude of sublattice B (m_B) increases, in order to separate the flat bands into two, and decrease the energy of the lower flat band, which is the one being filled. Due to the high density of states in the flat bands (which are related to B and C atoms only), newly added electrons choose to occupy sublattices B and C, until both flat bands are filled, which occurs at $n \approx 4/3$. Between $n = 1$ and $n = 4/3$, the magnetization m_B decreases again, because the lower flat band is full and electrons are now occupying the higher flat band, which has energy proportional to m_B. For filling $n \in [1, 2]$, the behaviour is symmetrical to that of the $n \in [0, 1]$ region.

8.5.2 Results in the strong coupling limit ($U \gg t$)

In this subsection, we discuss our results for high U, which we can assume to be nearly identical to those at $U \to \infty$, for two reasons. Firstly, through inspection of the plots in Fig. 8.3, one readily realizes that the behaviour at $U = 20$ is approximately the same as, say, $U = 15$, and therefore should not change with an increase in U. Moreover, if a certain value of U is enough to impose ferromagnetism (and therefore, for $n < 1$, the energy bands are singly occupied with spins in the same direction), higher values of U will have no additional effect. Secondly, the analytical results for $U \to \infty$ which we present in the following paragraphs are in agreement with the numerical results in Fig. 8.3 for $U = 20$.

One important first remark is that, as can be seen from Figs. 8.3a and 8.3b, the value of n_A or n_B for $U = 20$ along the line $n \in [0, 1]$, is the same as for $U = 0$ along the line $n \in [0, 2]$, but divided by two. This is because, at high U, the inequivalence of sublattices is imposed solely by the tight-binding terms of the Hamiltonian (see Eq. 8.11). Therefore, the behaviour of n_A and n_B is the same as in the tight-binding limit, albeit with all spins equally aligned. In fact, at $U = 0$, the tight-binding bands become doubly occupied without any additional energy cost, while for high U this cost is so high that all tight-binding states (thus, all sublattices) become singly occupied before double occupancies are created.

To study the $U \to \infty$ limit from a perturbation theory point of view, we begin by setting $t = 0$ in the Hamiltonian in Eq. 8.11 and taking the result as the unperturbed Hamiltonian. Its eigenvalues are

$$\begin{aligned} &\tfrac{U}{2}(n_A \pm m_A), \\ &\tfrac{U}{2}(n_B \pm m_B), \\ &\tfrac{U}{2}(n_C \pm m_C). \end{aligned} \tag{8.17}$$

These are six flat bands, with L states each. Positive m and negative m give the same set of eigenvalues, so let us assume positive m, with no loss of generality. At $n < 1$, electrons occupy the three lowest energy bands: $\frac{U}{2}(n_A - m_A)$, $\frac{U}{2}(n_B - m_B)$ and $\frac{U}{2}(n_C - m_C)$, so that the total

mean-field energy of the system is given by

$$E_{U\to\infty} = \frac{UL}{4}(m_A^2 + m_B^2 + m_C^2 - n_A^2 - n_B^2 - n_C^2) + \frac{U}{2}\left[\sum_{N_A}(n_A - m_A) + \sum_{N_B}(n_B - m_B) + \sum_{N_C}(n_C - m_C)\right], \quad (8.18)$$

where we have reintroduced the diagonal terms of Eq. 8.12. This expression can be simplified using the symmetries mentioned above: (i) $\delta_A + \delta_B + \delta_C = 0$, (ii) $n_B = n_C$ and (iii) $m_B = m_C$. Using these three relations and performing the summations up to some fixed $\widetilde{N}_A = L\widetilde{n}_A$, the total energy for large U and $n < 1$ becomes

$$E_{U\to\infty} = \frac{UL}{4}(m_A^2 + 2m_B^2 - \frac{3}{2}n_A^2 - \frac{9}{2}n^2 + 3nn_A) + \frac{UL}{2}\left[\widetilde{n}_A(n_A - m_A) + (3n - \widetilde{n}_A)\left(\frac{1}{2}(3n - n_A) - m_B\right)\right]. \quad (8.19)$$

We find the ground state energy by taking $\vec{\nabla}E_{U\to\infty} = \vec{0}$, where the derivatives are taken with respect to m_A, m_B and n_A. The result is the self-consistency $n_A = \widetilde{n}_A$ and the relations $m_A = n_A$ and $m_B = n_B$. These two relations hold true for $U = 20$, as can be realized by comparing n_A with m_A, and n_B with m_B in Fig. 8.3. Going back to $E_{U\to\infty}$ and replacing $n_A = m_A$ and $n_B = m_B$, we find that the three bands in Eq. 8.17 become degenerate with zero energy. Note that setting $n_A = m_A$ and $n_B = m_B$ does not lead to a minimum of $E_{U\to\infty}$, but to a saddle point, as expected. Again, Hartree-Fock mean-field theory is not about finding minima, but rather about finding self-consistency, as explained in section II. Finally, we remark that having $n_A = m_A$ and $n_B = m_B$ is a consequence of a ferromagnetic ground state with the bands being filled with only one spin direction.

The next step in the perturbation analysis is to introduce the hopping terms of the Hamiltonian of Eq. 8.11, as the perturbation. This perturbation lifts the degeneracy of the three zero-energy bands. Up to first order, one of them, comprising B- and C-type orbitals, retains zero energy, while each of the other two bands are pushed to positive or negative energy, proportionally to t, and comprise orbitals of the three types, A, B, and C. This new energy band configuration mimics that of the tight-binding limit. This justifies the relative filling of the sublattices at high U (Figs. 8.3a and 8.3b), and therefore their magnetization $m_A = n_A$ and $m_B = n_B$. We now have a lower band involving A, B, and C orbitals, an intermediate flat band built up from B and C orbitals, and a higher energy band involving all three types of atoms. It follows that, as we begin inserting electrons in the system, sublattice A fills at two times the rate of the B/C sublattices. At $n = 1/3$, the lower band (with energy proportional to $-t$) is full and $n_A = 1/4 = 2n_B = 2 \times 1/8$. Between $n = 1/3$ and $n = 2/3$, the flat band is filled up using only sublattices B and C, therefore n_A does not change. Finally, for $n \in [2/3, 1]$, sublattices A, B, and C become gradually half-filled as the band with energy proportional to $+t$ is filled. For filling $n \in [1, 2]$, the behaviour is symmetrical to that of the $n \in [0, 1]$ region.

8.5.3 Results near half-filling ($n \approx 1$)

At half-filling, the ground state is a $\vec{q} = (\pi, \pi)$ phase. Lieb's theorem [1] states that in bipartite systems, such as our Lieb lattice, the ground state at half-filling is ferrimagnetic

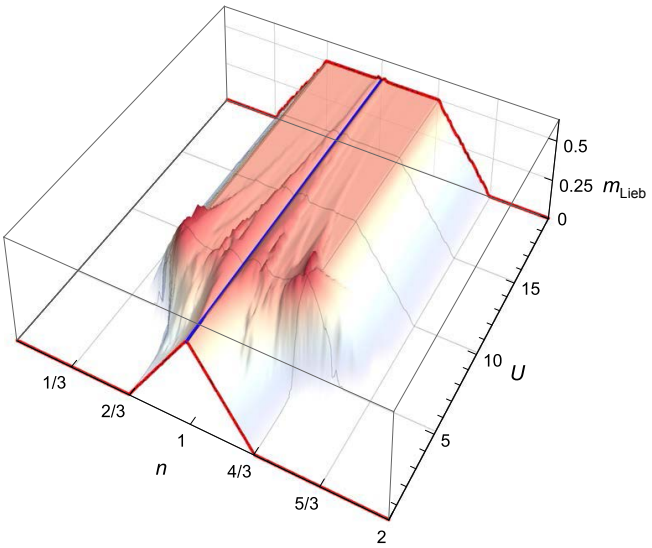

(a)

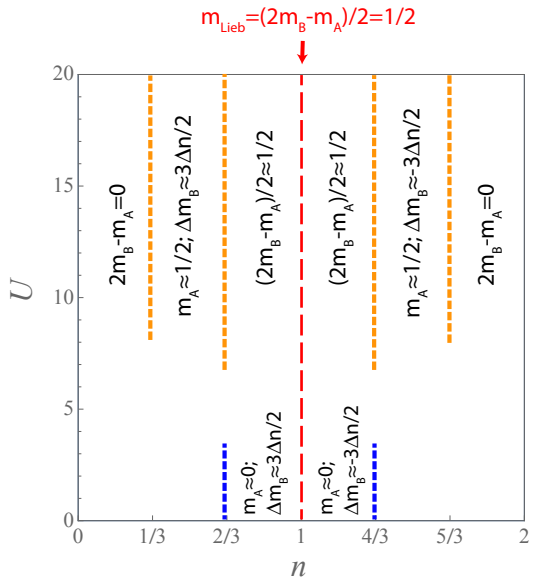

(b)

Figure 8.4: (a) Plot of the difference in the absolute values of the magnetization of the sublattices, $m_{\text{Lieb}} = \frac{1}{2}(2m_B - m_A)$, as a function of n and U, using the data from the plots in Figs. 8.3c and 8.3d. The bold red lines highlight the $U = 0$ and $U = 20$ edges of the plot, and the bold blue line at the center allows for easier visualization of the behaviour of $\frac{1}{2}(2m_B - m_A)$ at half-filling. According to a theorem by Lieb [1], the value of $\frac{1}{2}(2m_B - m_A)$ at half-filling is 1/2, a value which the plot shows to have been achieved by our mean-field approach. (b) Phase diagram illustrating the relative behavior of the magnetization of sublattices A and B, as a function of n and U.

[21]. In our case, this ferrimagnetic ordering is ferromagnetic within each sublattice, and antiferromagnetic between every two nearest-neighbour sites (see Fig. 8.1a). Although Lieb's

theorem does not provide information on the spin per site, it does state that in our system the quantity $\frac{1}{2}(2m_B - m_A)$ should be equal to 1/2. This served as one of the motivations for this work, as previous studies of the Lieb lattice using mean-field [2] failed to yield the value 1/2 at low U. One of the reasons for this was that the magnetization amplitude was the same on all sites, A, B, and C, and the relative occupation of the three sublattices in the tight-binding limit was used for finite U.

One can plot the function $\frac{1}{2}(2m_B - m_A)$, using our results for m_A and m_B, in Figs. 8.3c and 8.3d. Such a plot can be found in Fig. 8.4a. At exactly $n = 1$ (the bold blue line at the center of the plot), our generalized Hartree-Fock approach succeeds in yielding the result $\frac{1}{2}(2m_B - m_A) = \frac{1}{2}$, thus verifying Lieb's theorem. This leads to the conclusion that our mean-field study, allowing for modulation of m and n in the Lieb lattice, produces more accurate results than imposing the same magnetization and electronic density in the whole lattice. Moreover, this plot indicates that Lieb's theorem is verified approximately in the wider $n \in [2/3, 4/3]$ range.

The phase diagram given by Fig. 8.4b was constructed using the relative behavior of the magnetization of sublattices A and B. The dashed lines indicate the boundaries where the behavior of the magnetization of each sublattice changes. The magnetization m_{Lieb} is exactly 1/2 at the central (red) dashed line ($n = 1$). For small U, within the interval $2/3 < n < 4/3$, only sublattice B has finite magnetization. For large U, in the $n \in [2/3, 4/3]$ range, Lieb's theorem is verified approximately. Note that this range includes not only the ferromagnetic region of the phase diagram of Fig. 8.2a, but surprisingly also the adjacent spiral regions.

One other theorem, by Lieb and collaborators, refers to the particle density in the sublattices [32]. This theorem states that in the bipartite Hubbard model, there are no charge density modulations at half-filling. In other words, it means that at half-filling all sublattices are equally occupied and therefore half-filled, $n_A = n_B = n_C = 1$. Plotting n_A and n_B as a function of U at fixed $n = 1$, using our results for n_A and n_B (shown in Figs. 8.3a and 8.3b, respectively), we checked that we obtained the lines $n_A = 1$ and $n_B = 1$. As discussed in Section 8.5.2 of this paper, the behaviour of n_A and n_B at large U consists of two compacted copies of the behaviour at zero U. This holds true for any bipartite system. Consequently, for large U, not only are there not charge density modulations at half-filling, but also there are no charge modulations at $n = 1/2$ and $n = 3/2$.

The contrasting behavior in Fig.8.4b for large and small U can be interpreted as a consequence of the modifications of the mean-field energy dispersion as U increases. More precisely, for small U, one has a single quasi-flat band (twice degenerate with energy $\varepsilon \sim 0$), while for large U, one has two non-degenerate one-particle quasi-flat bands well separated in energy ($\varepsilon \sim 0$ and $\varepsilon \sim U$). Note that the flat bands for large U are present in the exact solution of the Hubbard model in the subspace of eigenstates associated with saturated ferromagnetism. As one can conclude from Fig. 8.4a, the difference in the absolute values of the magnetizations of the sublattices grows only when a flat band is being filled and in fact, we can write

$$m_{\text{Lieb}} = \frac{1}{2}(2m_B - m_A) \approx \text{filling of flat bands}, \tag{8.20}$$

for filling $n \leq 1$, both for large and small U. For $n > 1$, one has the reflected behavior of $n \leq 1$.

8.6 Conclusions

In summary, we have studied the Lieb lattice using a mean-field approach and allowing for charge and spin density modulation. Although theory about the correspondence between Hartree-Fock self-consistency and saddle points of the mean-field energy is relatively old (20 years old), to the extent of our knowledge, this is the first time it is in fact applied to a system where charge modulation is known to occur. We have found that, in the limits of low interaction ($U \to 0$) and very high interaction ($U \to \infty$) results agree with what one would expect. Namely, the relative occupation of sublattices A and B of the bipartite Lieb lattice (where sublattice A comprises the atoms with four nearest neighbours, and B denotes the remaining atoms) in the tight-binding limit coincides with the results in the literature (for instance, in Ref. [20]). We have also found that the profile of the relative occupation of the sublattices in both strong-coupling and tight-binding are analogous, and one can be inferred if the other is known. The argument is relatively simple. On the one hand, in the $U = 0$ limit, the energy dispersion is governed by the tight-binding terms of the Hamiltonian only and the energy bands in the case of the Lieb lattice are as depicted in Fig. 8.1c. On the other hand, in the limit $U \gg t$, the energy bands are separated by a very high energy gap (of the order of U), the lower bands corresponding to no double occupancies and the higher bands to double occupancies. The gradual filling of the system is done by singly filling all sites and only then jumping to the higher bands and doubly occupying all sites. Each one of these two filling regimes follows the relative occupation of sublattices that occurs in the tight-binding limit.

At half-filling, our numerical mean-field results verify two important exact results for the Hubbard model. Firstly, one theorem [1] states that in bipartite lattices with more B-type atoms than A-type atoms, the total spin per unit cell at half-filling is equal to $m_{\text{Lieb}} = (|B| - |A|)/2$, where $|x|$ denotes the number of x-type atoms a unit cell. In the case of our bipartite Lieb lattice, we get $(2-1)/2 = 1/2$. Our results are plotted in Fig. 8.4. At exactly half-filling we obtained the expected value $1/2$. Additionally, for large U, in the $n \in [2/3, 4/3]$ range, we found that $m_{\text{Lieb}} \approx 1/2$. Interestingly, this range includes not only the ferromagnetic region of the phase diagram of Fig. 8.2a, but also the adjacent spiral regions. Secondly, another theorem [32] states that in the bipartite Hubbard model, there are no charge density modulations at half-filling, that is, at half-filling all sublattices are equally occupied and half-filled. Our numerically calculated relative occupations of sublattices A and B of a bipartite Lieb lattice, shown in Figs. 8.3a and 8.3b, are in agreement with this theorem. In addition, we found that, for large U, not only are there no charge density modulations at half-filling, but also there are no charge modulations at $n = 1/2$ and $n = 3/2$.

Away from half-filling, we found that, for large and small U, the difference in the absolute values of the sublattice magnetizations (m_{Lieb}) grows or decreases only when a flat band is being filled and furthermore, for $n \leq 1$, m_{Lieb} is given approximately by the filling of the flat bands. Note that m_{Lieb} is the unit cell magnetization in the case of the $\vec{q} = (\pi, \pi)$, the ferrimagnetic phase of the Lieb lattice found at half-filling.

We suggest that much of the above discussion is valid in the case of other bipartite lattices with flat bands in the energy dispersion. In the case of non-bipartite lattices with more than two types of atoms in the unit cell, the analysis is more complex because, for instance, an antiferromagnet configuration between sublattices may not be commensurate with the unit cell.

Bipartite lattices of various geometries can be realized by manipulating quantum dot arrays [33] or cold atoms in optical lattices [34]. In an experimental setting, it is important to consider

the role of disorder, and one may question how much of the behavior shown in the phase diagram of Fig. 8.2a survives if disorder is introduced in the lattice. Indeed, the interplay of disorder and electronic interactions in lattice models has been addressed in several works, using a variety of theoretical and numerical approaches (such as dynamical mean field theory[35], renormalization group approaches[36] and others[37]). However, consensus concerning the effect of disorder in the Mott metal-insulator transition or the effect of interactions in the metal-insulator transition (induced by disorder) has not been reached[37]. Nevertheless, disorder in lattice models with Hubbard-like interactions is expected to oppose the appearance of the magnetic long range spatial order. In the case of the Lieb lattice, local disorder (reflecting the introduction of impurities or local defects in the lattice) lifts only partially the degeneracy of the flat tight-binding band, since the localized states in their most compact form occupy a single Lieb plaquette, and if no defect or impurity is present in that plaquette, a localized state can be associated to that plaquette. Thus, the flat band survives in the weak disorder limit, but loses states as disorder is increased. Note that such disorder is different from the usual assumption of diagonal disorder (random local potentials) which has been addressed in several works[35, 36, 38–40]. This latter type of disorder model (proposed by Anderson several decades ago [38]) is more appropriate in the limit of stronger disorder, in our opinion. The main justification for the existence of magnetic order even at weak coupling (in the doping interval corresponding to the flat band) in the phase diagram of Hubbard model in a Lieb lattice (see Fig. 8.2a) is the fact that any electronic interaction acts as a strong interaction if degeneracy at the Fermi level is high. So, in the presence of weak disorder which lifts only partially the flat band degeneracy, we still expect to observe magnetic order at weak coupling but in a narrower doping interval. Note that it has been shown that in infinite dimensions, there is always antiferromagnetic order at strong coupling, even with disorder[40].

Another relevant question is the effect of flat band broadening in the magnetic phase diagram of the Hubbard model in the Lieb lattice. The removal of the flat band macroscopic degeneracy can be achieved, for instance, by deforming the lattice, introducing different on-site energies (periodically, not randomly) or introducing additional hopping terms (introducing the third dimension, for example). In such a case, the flat band would be broadened by $\Delta\varepsilon$. The effect of such broadening depends on the ratio of the two energy scales, $\Delta\varepsilon$ and U. If $\Delta\varepsilon$ is large compared with U, we expect behavior similar to that of the Hubbard model in a square lattice, that is, a paramagnetic phase is dominant except at half filling where the antiferromagnetic phase is present (ferrimagnetic phase in the case of the Lieb lattice). If $\Delta\varepsilon$ is small compared with U, magnetic phases should be expected. This implies that at the bottom of our phase diagram (Fig. 8.2a), the magnetic phases would be replaced by a narrow strip of paramagnetic phase (with height of the order of $\Delta\varepsilon$) in the doping interval corresponding to the flat band.

Concerning now the broadening of the flat band due to weak local disorder of the Anderson type, one should take into account weak localization effects that are known to lead to a weak logarithmic increase of resistance as the temperature is reduced, if interactions are absent [41]. However, note that for quasi-2D materials such logarithmic enhancement is absent (3D metals are diffusive in the weak disorder limit[41]), but the magnetic order described in the phase diagram of Fig. 8.2a should survive (the third dimension helps to stabilize magnetic order, since quantum fluctuations are reduced) in the region of the phase space where the energy scale U is dominant.

8.7 Appendix A: Min-Max theorem for the Hubbard model

In this appendix, we discuss how the mean-field method should be applied to the Hubbard model if particle density is not fixed and in particular, we justify Eq. 8.6. Our approach follows the method presented in Ref. [26]. We start by presenting the usual mean-field approach and then we explain, using the method presented in Ref. [26], why this approach is somewhat misleading.

8.7.1 The usual mean-field method

We begin with the Hubbard Hamiltonian, given by

$$H = t \sum_{\langle x,y\rangle,\sigma} c^\dagger_{x,\sigma} c_{y,\sigma} + U \sum_x \hat{n}_{x,\uparrow}\hat{n}_{x,\downarrow} \tag{8.21}$$

We then replace the interaction term with the Hartree and Fock terms (see Eq. 8.2). These terms are obtained by considering that each fermionic operator only deviates slightly from its mean value, so that in a product of operators, we can neglect quadratic terms in these deviations.

The operators $c^\dagger_{x,\uparrow}c_{x,\uparrow}$ and $c^\dagger_{x,\uparrow}c_{x,\downarrow}$ can be identified with the particle density operator n_x and the s^+_x operator. For consistence with the notation in reference [28], the spin operators in this appendix are

$$\begin{aligned} c^\dagger_\uparrow c_\downarrow &= s^+ = \tfrac{1}{2}(s^x + is^y) \\ c^\dagger_\downarrow c_\uparrow &= s^- = \tfrac{1}{2}(s^x + is^y) \\ c^\dagger_\uparrow c_\uparrow - c^\dagger_\downarrow c_\downarrow &= s^z. \end{aligned} \tag{8.22}$$

The vector $\hat{\vec{s}}_x$ is the spin density operator on site x. The peculiarity of this definition of s^+ and s^- is the factor $1/2$ which is often included in operators s^x and s^y instead. Replacing this in the interaction term of the Hamiltonian in Eq. 8.21 gives

$$H_{\text{HF}} = t \sum_{\langle x,y\rangle,\sigma} c^\dagger_{x,\sigma} c_{y,\sigma} + U \sum_x \left[\frac{1}{4}\left(\langle \hat{\vec{s}}_x\rangle^2 - \langle \hat{n}_x\rangle^2 \right) + \frac{1}{2}\left(\langle \hat{n}_x\rangle \hat{n}_x - \langle \hat{\vec{s}}_x\rangle \cdot \hat{\vec{s}}_x \right) \right], \tag{8.23}$$

We now replace the averages by the mean-field parameters $\vec{m}_x$ and n_x. These parameters can be identified with the mean values of the magnetization and particle density, respectively, upon extremization of the mean-field free energy, i.e., when the self-consistency equations are satisfied. The Hartree-Fock Hamiltonian becomes

$$H(\vec{m}, n) = \sum_{x,y,\sigma,\sigma'} h_{x\sigma y\sigma'} c^\dagger_{x,\sigma} c_{y,\sigma'} + \frac{U}{4} \sum_x \left(\vec{m}_x^2 - n_x^2 \right), \tag{8.24}$$

where

$$h_{x\sigma y\sigma'} = t\delta_{\sigma\sigma'} + \frac{U}{2} \left(n_x \delta_{\sigma\sigma'} - \vec{m}_x \cdot \vec{\sigma}_{\sigma\sigma'} \right) \delta_{xy}. \tag{8.25}$$

Here, $\vec{\sigma}_{\sigma\sigma'}$ is the vector of Pauli matrices. The function $F(\vec{m}, n)$ is calculated from $H(\vec{m}, n)$ using the partition function,

$$\begin{aligned} F(\vec{m}, n) &= -\tfrac{1}{\beta} \ln Z(\vec{m}, n) = -\tfrac{1}{\beta} \ln \left(\text{Tr}\left(e^{-\beta H(\vec{m},n)} \right) \right) \\ &= -\tfrac{1}{\beta} \text{Tr}\left(\ln\left(1 + e^{-\beta h} \right) \right) + \tfrac{U}{4} \sum_x \left(\vec{m}_x^2 - n_x^2 \right). \end{aligned} \tag{8.26}$$

At this stage, one usually finds the minimum free energy, F_{HF}, by minimizing $F(\vec{m}, n)$ with respect to the mean-field parameters and this would lead to the usual self-consistency equations [42]. Clearly, this works for fixed particle density, but in the previous expression we allow for variable particle density and the respective quadratic term has a negative coefficient. If one imposed a minimization with respect to the parameter n_x, convergence would not be achieved in a numerical approach, unless one limits the possible values of n_x to a certain interval, in which case the result of the numerical minimization would lie at the boundary of this interval. This reflects the fact that one should not minimize with respect to the parameter n_x, but instead maximize, as we explain in the next subsection.

8.7.2 A different perspective for the mean-field method

In this subsection, we present the mean-field approach which should be applied when one takes into account the possibility of non-uniform particle density in a lattice. For a rigorous proof see, for instance, Refs. [26–28].

Our goal is to know the thermal equilibrium state of the system which minimizes the free energy. These states are defined in terms of density matrices. Having an exact free energy would require having an exact partition function, which in turn would require an exact diagonalization of the Hubbard model. The Hartree-Fock method provides an approximation to the exact equilibrium state, in terms of many-body states of non-interacting particles, replacing the quartic terms of the Hamiltonian by one-particle potentials (which are adjusted to provide the best possible approximation). The free energy obtained in the Hartree-Fock method provides an upper bound to the exact free energy (a consequence of the variational theorem). Since the particles are independent, the Hartree-Fock state can be written as a one-particle density matrix, $\gamma_{ij} = \langle c_i^\dagger c_j \rangle$ [26]. The objective of the mean-field method is indeed to find the minimum free energy in the set of free energies associated with the possible states of N independent particles (or equivalently, associated with the possible one-particle density matrices),

$$F_{HF} = \min_{\gamma} F(\gamma) = \min_{\gamma} [E(\gamma) - \frac{1}{\beta} S(\gamma)]. \tag{8.27}$$

where β is the einverse temperature. In the previous expression, no mean field parameters are present and the free energy is determined for each γ using the exact Hamiltonian (the mean field approximation is associated with the state, not with the Hamiltonian). However, calculating $\min_\gamma F(\gamma)$ going through all γ is not pratical, so one introduces mean-field parameters. In the next paragraphs, we introduce these parameters, following a derivation in Ref. [26]. For now, let us assume zero temperature.

In the case of the Hubbard Hamiltonian, the Hartree-Fock energy functional, $E(\gamma)$, can be written as (Ref. [26] Lemma 2)

$$E(\gamma) = \mathrm{Tr}[T\gamma] + U \sum_x [\langle \hat{n}_x \rangle^2 - \langle \hat{\vec{s}}_x \rangle^2], \tag{8.28}$$

where x labels the lattice sites and T is the matrix whose elements t_{xy} are the transition amplitudes of an electron to move from site x to site y or vice versa. The averages of the electronic and spin densities at site x are

$$\begin{aligned} \langle \hat{n}_x \rangle &= \mathrm{Tr}\left[\hat{\mathbb{I}} \cdot \gamma \right], \\ \langle \hat{\vec{s}}_x \rangle &= \mathrm{Tr}\left[(\hat{\mathbb{I}} \otimes \hat{\vec{\sigma}}) \cdot \gamma \right], \end{aligned} \tag{8.29}$$

respectively.

The first step to introduce the variational parameters is to use the simple fact that

$$x^2 \geq 2xy - y^2 \quad \text{for all } x, y \in \mathbb{R}^n, \tag{8.30}$$

where equality holds if and only if $x = y$. This implies

$$x^2 = \max_y (2xy - y^2), \tag{8.31}$$

and therefore, we can write

$$\langle \hat{n}_x \rangle^2 = \max_{n_x} \left\{ 2\langle \hat{n}_x \rangle n_x - n_x^2 \right\} \tag{8.32}$$

and

$$-\langle \hat{\vec{s}}_x \rangle^2 = \min_{\vec{m}_x} \left\{ \vec{m}_x^2 - 2\langle \hat{\vec{s}}_x \rangle \cdot \vec{m}_x \right\}. \tag{8.33}$$

where n_x and $\vec{m}_x$ are, at this point, an arbitrary constant and vector. Inserting this into Eq. 8.28, the energy for a given state γ at zero temperature assumes the form

$$E(\gamma) = \min_{\vec{m}} \max_n \left\{ E(n, \vec{m}, \gamma) \right\}, \tag{8.34}$$

where $E(n, \vec{m}, \gamma)$ is given by

$$E(n, \vec{m}, \gamma) = \mathrm{Tr} \left[\left(T - U \sum_{\text{all sites}} \left[n_x \cdot \hat{\mathbb{I}} - \vec{m}_x \cdot \hat{\vec{\sigma}} \right] \right) \gamma \right] + U \sum_{\text{all sites}} \left(\vec{m}_x^2 - n_x^2 \right), \tag{8.35}$$

The aim of the mean-field method is to obtain

$$\min_\gamma E(\gamma) = \min_\gamma \min_{\vec{m}} \max_n \left\{ E(n, \vec{m}, \gamma) \right\}. \tag{8.36}$$

The crucial point of the mean-field method is the possibility of exchanging the order of the extremization, which is implicitly done in standard mean-field. In fact, if particle density is fixed, one has

$$\min_\gamma E(\gamma) = \min_\gamma \min_{\vec{m}} \left\{ E(\vec{m}, \gamma) \right\} = \min_{\vec{m}} \min_\gamma \left\{ E(\vec{m}, \gamma) \right\}, \tag{8.37}$$

since the order of minimization is irrelevant, and one recovers the usual mean-field picture, in which one has to minimize the energy with respect to the mean-field parameter $\vec{m}$.

On the other hand, if the particle density n_x is allowed to actually depend on x, in Ref. [26] it was shown that indeed

$$\min_\gamma \min_{\vec{m}} \max_n \left\{ E(n, \vec{m}, \gamma) \right\} = \min_{\vec{m}} \max_n \min_\gamma \left\{ E(n, \vec{m}, \gamma) \right\}. \tag{8.38}$$

Here, we present a simple physical interpretation for this result.

First, one should note that Eq. 8.35 for given $\vec{m}$ and n corresponds to the energy of independent particles subjected to one-particle potentials which depend on the given $\vec{m}$ and n. Looking at the left-hand side of Eq. 8.38, after one has minimized and maximized $E(n, \vec{m}, \gamma)$ with respect to $\vec{m}$ and n respectively, the remaining minimization (with respect to γ) will lead, at zero temperature, to a filled Fermi sea associated to these one-particle potentials. These

one-particle potentials might, for instance, generate imbalance between the number of up and down spins and lead to finite magnetization.

Second, Eqs. 8.32 and 8.33, associated with minimization and maximization with respect to $\vec{m}$ and n, imply the self-consistency equations

$$\begin{aligned} \langle \hat{n}_x \rangle &= n_x, \\ \langle \hat{\vec{s}}_x \rangle &= \vec{m}_x, \end{aligned} \tag{8.39}$$

and therefore, computing the left-hand side of Eq. 8.38 can be interpreted as the following instruction: "Among the set of one-particle density matrices that satisfy the self-consistency equations, find the one with minimum energy". As we said above, this minimum energy corresponds to a filled Fermi sea at zero temperature, so in the set of states corresponding to filled Fermi seas, there is one that satisfies the self-consistency equations. This helps us understand the right-hand side of Eq. 8.38 in the following way: "Among the set of all filled Fermi seas, find (the energy of) the state which satisfies the self-consistency equations".

This argument can be generalized for finite temperature [26], taking into account the entropy contribution. In this case, instead of filled Fermi seas, one has the one-particle density matrices that minimize the free energy in the case of independent particles. If instead of fixed number of particles, one imposes a fixed chemical potential (in which case the grand-canonical potencial would replace the free energy), this one-particle density matrix would become the Fermi-Dirac distribution function.

8.8 Appendix B: How to extremize $E_{\mathbf{HF}}$

In this appendix, we explain in more detail the algorithm we used for finding saddle points.

Our first approach to extremize E_{HF} was perhaps the most intuitive non-brute force one. It consisted in maximizing E_{HF} with respect to δ_A, δ_B, and δ_C using our results for q_x, q_y, m_A and m_B of the Hubbard model in a square lattice [23]. The lattice size was also kept at 100×100. Due to the two restrictions imposed (fixed number of particles in the system and equivalence of B and C sites), we are left with one parameter as maximizer of E_{HF}. We used δ_A. We note that the minimum of E_{HF} with respect to δ_A was found to be negative infinity (using the results in Ref. [23] for m_A and m_B as starting points). Fixing q_x, q_y, m_A and m_B means that the magnetic phases are kept the same as our previous ones, only the occupation numbers in the sublattices change. However, finding saddle points by starting from a minimum with respect to one direction (the m direction) and then finding the maximum with respect to an orthogonal direction (the n direction) turned out to diverge on most points of the phase diagram. In fact, the suggestion that saddle points of a function can be found by starting at a random point in the function, minimizing the function with respect to the minimizer variables, and then using those new points to maximize the function with respect to the maximizer variables, is false. As a matter of fact, this statement remains false even in a more generalized case. One might think that by successively minimizing and maximizing the function, one would eventually reach a saddle point. This is also not necessarily true. When trying to use this method to extremize E_{HF}, one finds that, in most points of the diagram, the value of E_{HF} resulting from the last maximization and the value of E_{HF} resulting from the last minimization differ by orders of magnitude comparable to those of E_{HF} itself. Additionally, the values of m_A, m_B, δ_A and δ_D which extremize E_{HF} (or so one thought) do not converge on each successive iteration, they alternate between several possible results.

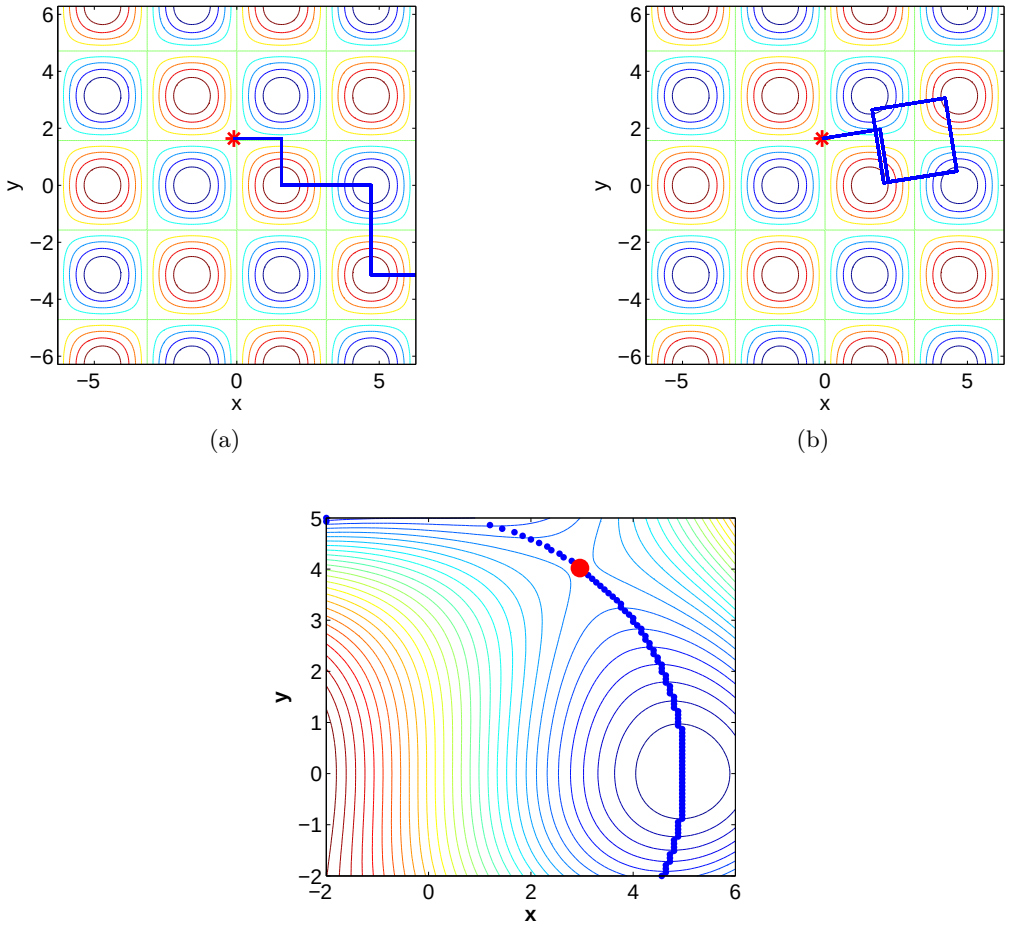

Figure 8.5: (a,b) Contour plots of the function function $f(x, y) = \sin(x)\cos(y)$ in the range $x, y \in [-2\pi, 2\pi]$. The maxima are at the center of the red circles, the minima are at the center of the blue circles, and the saddle points are at the intersections of the green lines. The straight bold lines overlapped with the contour plots are the path taken by an algorithm which attempts to find a saddle point of $f(x, y)$, by starting at point $(-0.1, \pi - 1.5)$ (red asterisk), and (a) successively minimizing in the x direction and maximizing in the y direction, and (b) successively minimizing in the direction which makes an angle of $\pi/10$ with the x axis and maximizing in a direction which makes an angle of $\pi/10$ with the y axis. (c) Contour plot of the function $f(x, y) = 2x^3 + 6xy^2 - 3y^3 - 150x$ in the range $(x, y) \in [-2, 6] \times [-2, 5]$. The small (blue) dots represent minima of $f(x, y)$ with respect to the x direction and the large (red) dot represents the maximum of these minima, which is a good approximation of a saddle point.

In order to better understand why this method may fail to find saddle points, one can consider a much simpler example, the function $f(x, y) = \sin(x)\cos(y)$. This function is periodic, oscillates between -1 and 1, and has infinitely many minima, maxima and saddle points (Fig. 8.5). Let us now assume that we want to find the saddle points of $f(x, y)$ using the method of minimizing and maximizing several times alternating between the two, using x

as minimizer and y as maximizer. If we start with a non-saddle point, the algorithm fails to find a saddle point and instead, after 2 ou 3 steps, alternates between absolute minima and maxima. Even if we start at a saddle point, successive iterations will move away from it and back to jumping between maxima and minima (see Fig. 8.5a). No initial point will allow this algorithm to converge to a saddle point, no matter how close it is to it. This is precisely what happened with the case of E_{HF}. Depending on the pair (n, U) in question, E_{HF} may or not behave in a way that allows saddle points to be found using this method.

One possible alternative approach to finding saddle points of $f(x, y)$ is to attempt to extremize the function in a different direction (or rotating the axes, which is another way to see it). Instead of using x and y as variables, we can use two auxiliary variables which are linear combinations of x and y but still orthogonal. For instance, we can alternate between the following two:

- replace $x \to x_0 + r\cos\theta$, and $y \to y_0 + r\sin\theta$, and minimize with respect to r;
- replace $x \to x_0 + r\sin\theta$, and $y \to y_0 - r\cos\theta$, and maximize with respect to r.

Setting $\theta = 0$ would reduce this to simply minimizing with respect to x and maximizing with respect to y, as described above. Due to the symmetry of the simple function we used, we should ideally use $\theta = \pi/4$ for the fastest convergence. For angles close enough to $\pi/4$ we can indeed find a good approximation for a saddle point. Nevertheless, if we deviate too much from $\pi/4$, saddle points may not be found anymore. Using a "wrong" angle will make the algorithm diverge even if we start very close to a saddle point, even if the starting point is a saddle point itself. The algorithm will often be circling the saddle point (see Fig. 8.5b).

The conclusion is that alternating between maximization and minimization is too sensitive to the initial point to be used to find saddle points. In the case of the simple highly-symmetric function $f(x, y)$, the saddle point is located at the center of the squares or rectangles that are drawn when connecting the points given by the algorithm, but this was shown to not be the case with E_{HF}. Moreover, this ideal angle depends on the pair (n, U) which is being studied, and some angles may not even produce closed polygons, but rather diverge to infinity in a certain direction.

The working alternative is failproof in the sense that it will always converge to one saddle point. It consists of calculating the value of $f(x, y)$ for many points in an area which is known to contain at least one saddle point, making a list of the maximum value of the function for each x and then finding the minimum of all the maxima that were found. If $f(x, y)$ is continuous we will end up on a saddle point. In the case of E_{HF}, we have not two variables but three: m_A, m_B and δ_A. In order to achieve an acceptable precision, it would be reasonable to calculate, say, 100 values of E_{HF} in each direction (m_A, m_B, and δ_A), for a total of 10^6 values for each pair (n, U) in our phase diagram, which could take a long time and would have a precision of about two decimal places. A more efficient alternative is to divide each direction into fewer parts, say 7 or 8, finding an initial approximation to the saddle point, and then repeating this a dozen times considering a smaller hypercube centered on the new point. Assuming each direction is divided into 7 parts (i.e. we calculate 8 function values in each direction) and the side of the hypercube is halved with each of 12 iterations, we now calculate a total of $7^3 \times 12 \approx 4000$ values of E_{HF} per pair (n, U). This was the procedure we used, which has a precision of around $1/4096$, or three decimal places. An illustration of this method is shown in Fig. 8.5c, where we have used the function $f(x, y) = 2x^3 + 6xy^2 - 3y^3 - 150x$ and successfully found the saddle point $(3, 4)$.

References

[1] E. H. Lieb. "Two Theorems on the Hubbard model". *Physical Review Letters* 62 (1989), pp. 1201–1204.

[2] J. Gouveia and R. Dias. "Magnetic phase diagram of the Hubbard model in the Lieb lattice". *Journal of Magnetism and Magnetic Materials* 382 (2015), pp. 312–317.

[3] J. G. Bednorz and K. A. Müller. "Possible high T_c superconductivity in the Ba-La-Cu-O system". *Zeitschrift fur Physik B Condensed Matter* 64 (1986), pp. 189–193.

[4] M. A. Kastner et al. "Magnetic, transport, and optical properties of monolayer copper oxides". *Rev. Mod. Phys.* 70 (1998), pp. 897–928.

[5] R. G. Dias and J. M. B. Lopes dos Santos. "Simple representation of the eigenstates of the $U \to \infty$ one-dimensional Hubbard model". *Journal de Physique I* 2 (1992), pp. 1889–1897.

[6] M. P. Marder. *Condensed Matter Physics*. John Wiley and Sons, 2000.

[7] D. R. Penn. "Stability Theory of the Magnetic Phases for a Simple Model of the Transition Metals". *Phys. Rev.* 142 (1966), pp. 350–365.

[8] J. Dorantes-Dávila, J. L. Morán-López, and M. Avignon. "Ground-state solutions of the Hubbard model". *Phys. Rev. B* 27 (1983), pp. 575–577.

[9] E. Kaxiras and E. Manousakis. "Ground state of the strong-coupling Hubbard Hamiltonian: A numerical diagonalization study". *Phys. Rev. B* 37 (1988), pp. 656–659.

[10] S. N. Coppersmith and C. C. Yu. "Phase diagram of the Hubbard model: A variational wave-function approach". *Phys. Rev. B* 39 (1989), pp. 11464–11474.

[11] A. Richter, G. Röpke, and F. Goedsche. "Functional Integral Approach for the Hubbard Model with Arbitrary Electron Density". *Physica Status Solidi B Basic Research* 88 (1978), pp. 189–198.

[12] S. Sarker et al. "Spiral states in the square-lattice Hubbard model". *Phys. Rev. B* 43 (1991), pp. 8775–8778.

[13] E. Langmann and M. Wallin. "Mean Field Magnetic Phase Diagrams for the Two Dimensional $t - t' - U$ Hubbard Model". *Journal of Statistical Physics* 127 (2007), pp. 825–840.

[14] P. A. Igoshev et al. "Incommensurate magnetic order and phase separation in the two-dimensional Hubbard model with nearest- and next-nearest-neighbor hopping". *Phys. Rev. B* 81 (2010), p. 094407.

[15] W. Schumacher. "On incommensurate phases in the magnetic phase diagram of the hubbard model". *physica status solidi (b)* 119.1 (1983), pp. 235–238.

[16] A. Mielke. "Exact ground states for the Hubbard model on the Kagome lattice". *Journal of Physics A* 25 (1992), p. 4335.

[17] H. Tasaki. "Ferromagnetism in the Hubbard Models with Degenerate Single-Electron Ground States". *Physical Review Letters* 69 (1992), pp. 1608–1612.

[18] V. J. Emery. "Theory of high-T_c superconductivity in oxides". *Physical Review Letters* 58 (1987), pp. 2794–4797.

[19] R. T. Scalettar et al. "Antiferromagnetic, charge-transfer and pairing correlations in the three-band Hubbard model". *Physical Review B* 44 (1991), pp. 770–781.

[20] H. Wang, S.-L. Yu, and J.-X. Li. "Spin fluctuations and unconventional pairing on the Lieb lattice". *Physics Letters A* 378.45 (2014), pp. 3360–3365.

[21] A. Mielke and H. Tasaki. "Ferromagnetism in the Hubbard model". *Communications in Mathematical Physics* 158.2 (1993), pp. 341–371.

[22] K. Noda, K. Inaba, and M. Yamashita. "Flat-band ferromagnetism in the multilayer Lieb optical lattice". *Phys. Rev. A* 90 (2014), p. 043624.

[23] J. D. Gouveia and R. G. Dias. "Spiral ferrimagnetic phases in the two-dimensional Hubbard model". *Solid State Communications* 185 (2014), pp. 21–24.

[24] M. Dzierzawa. "Hartree-Fock theory of spiral magnetic order in the 2-d Hubbard model". *Z. Phys. B* 86 (1992), pp. 49–52.

[25] E. Langmann and M. Wallin. "Restricted path integral approach to the doped Hubbard model". *Europhysics Letters* 37 (3) (1997), pp. 219–224.

[26] V. Bach and J. Poelchau. "Hartree-Fock Gibbs states for the Hubbard model". *Markov Processes and Rel Fields* 2(1) (1996), pp. 225–240.

[27] V. Bach, E. H. Lieb, and J. P. Solovej. "Generalized Hartree-Fock theory and the Hubbard model". *Journal of Statistical Physics* 76 (1994), pp. 3–89.

[28] J. de Woul. "A restricted Hartree-Fock study of the 2D Hubbard model". MA thesis. Royal Institute of Technology, 2007.

[29] E. Langmann and M. Wallin. "Mean-field approach to antiferromagnetic domains in the doped Hubbard model". *Physical Review B* 55 (1997), pp. 9439–9451.

[30] M. Nita, B. Ostahie, and A. Aldea. "Spectral and transport properties of the two-dimensional Lieb lattice". *Physical* 87 (2013), p. 125428.

[31] A. Singh, Z. Tesanovic, and H. H. Kim. "Instability of the spiral state of the doped Hubbard model". *Pramana - J. Phys.* 38 (1992), pp. 211–217.

[32] E. H. Lieb, M. Loss, and R. J. McCann. "Uniform density theorem for the Hubbard model". *Journal of Mathematica Physics* 34 (1993), pp. 891–898.

[33] H. Tamura, K. Shiraishi, and H. Takayanagi. "Ferromagnetism in Semiconductor Dot Array". *Jpn. J. Appl. Phys.* 39 (2000), p. L241.

[34] N. Goldman, D. F. Urban, and D. Bercioux. "Topological phases for fermionic cold atoms on the Lieb lattice". *Phys. Rev. A* 83 (2011), p. 063601.

[35] Y. Song, R. Wortis, and W. A. Atkinson. "Dynamical mean field study of the two-dimensional disordered Hubbard model". *Phys. Rev. B* 77 (2008), p. 054202.

[36] E. Kuchinskii, N. Kuleeva, and M. Sadovskii. "Attractive Hubbard model with disorder and the generalized Anderson theorem". English. *Journal of Experimental and Theoretical Physics* 120.6 (2015), pp. 1055–1063.

[37] S. S. Kondov et al. "Disorder-Induced Localization in a Strongly Correlated Atomic Hubbard Gas". *Phys. Rev. Lett.* 114 (2015), p. 083002.

[38] P. W. Anderson. "Absence of Diffusion in Certain Random Lattices". *Phys. Rev.* 109 (1958), pp. 1492–1505.

[39] G. T. Zimanyi and E. Abrahams. "Disorder and interactions in the Hubbard model". *Phys. Rev. Lett.* 64 (1990), pp. 2719–2722.

[40] M. Ulmke, V. Janis, and D. Vollhardt. "Anderson-Hubbard model in infinite dimensions". *Phys. Rev. B* 51 (1995), pp. 10411–10426.

[41] E. Abrahams et al. "Scaling Theory of Localization: Absence of Quantum Diffusion in Two Dimensions". *Phys. Rev. Lett.* 42 (1979), pp. 673–676.

[42] H. Bruus and K. Flensberg. *Many-Body Quantum Theory in Condensed Matter Physics: An Introduction*. Oxford Graduate Texts. OUP Oxford, 2004.

Chapter 9

Conclusions

This thesis presents the results of research performed from January 2012 to July 2016, at the Physics Department of the University of Aveiro. The subject under consideration was magnetism and spin dynamics of electronic systems with non-trivial geometries. The research was done in collaboration with my supervisor, Prof. Ricardo Dias. The results concerning the time evolution of localized states in the Lieb lattice were obtained with Ivo Maceira (M. Sc. student).

The two-dimensional Hubbard model is the most extensively studied model in condensed matter physics, both analytically and numerically. Nevertheless, exact results are rare and apply only to certain limits, such as setting some parameters to zero or infinity, or considering all sites of the system are singly occupied. Performing numerical calculations to model a certain system inevitably forces its discretization, and imposes restrictions upon its size, giving rise to unwanted finite-size effects. In addition, these approximate methods rely on assumptions, and the mean-field method, used in this thesis, is no exception. In the case of the Hubbard model, researchers have long been considering different assumptions, producing a variety of results. One example of this is the qualitative and quantitative diversity of magnetic phase diagrams of the two-dimensional Hubbard model which exists in the literature, every one of them correct under its respective assumptions.

The aim of this thesis is to contribute for the understanding of the behavior of the two-dimensional Hubbard model in what concerns its dependence on the geometry of the underlying lattice, both in terms of boundary conditions and geometric frustration.

In Chapter 3, we extend the mean-field studies of the Hubbard model on square lattices. Every mean-field study has its limitations, namely due to the restrictions in the allowed types of magnetic ordering. The research which ultimately led to the results presented in this chapter lifted one of these limitations: that the magnetization be the same throughout the whole lattice. By lifting the aforementioned limitation, we were able to obtain ground-state energies which are lower than the ones obtained otherwise. This shows that one should exercise caution when using approximate methods to study the 2D Hubbard model. Furthermore, although it cannot be seen just by inspecting the mean-field magnetic phase diagram, the energies corresponding to the different magnetic phases are very close in the limit of high Hubbard U, which contrasts with the opposite limit, where the different phases are well separated energetically. The results were published as

> J. D. Gouveia and R. G. Dias, *Spiral ferrimagnetic phases in the two-dimensional Hubbard model*. Solid State Communications, Volume 185, May 2014, Pages 21-24

DOI: 10.1016/j.ssc.2014.01.004

In Chapter 4, we introduce our first case of a non-trivial geometry: the helicoidal lattice. On the one hand, this lattice is similar to a 1D chain in what concerns electronic motion. On the other hand, it resembles a 2D periodic square lattice (a torus) in terms of shape, differing only on the boundary conditions. We show that a spin queue model is generated by the transversal hopping term ($t_\perp$) of the Hamiltonian in the $U = \infty$ limit. While this model appears in first order in $t_\perp$, it provides insight on the spin dynamics of the $U = \infty$ Hubbard model on a square lattice. Further studies are required concerning, for example, the presence of several holes in the lattice.

The remaining four chapters of this thesis are dedicated to flat-band systems, focusing on the Lieb lattice. In Chapter 5, we present a set of rules for constructing localized eigenstates of both tight-binding and Hubbard Hamiltonians in decorated lattices. While the simplest form of localized eigenstates of these lattices was known, they were considered unrelated. By using what we called the "origami rules", one can find the form of localized states of a certain type of decorated lattice, starting from a localized state of another type of lattice. The rules were obtained through simple tight-binding calculations and can be used to obtain localized states of flat-band systems with other shapes or dimensionalities. The results were published as

R. G. Dias and J. D. Gouveia, *Origami rules for the construction of localized eigenstates of the Hubbard model in decorated lattices.* Scientific Reports 5, Article number: 16852 (2015)

DOI: 10.1038/srep16852

Chapter 6 is dedicated to the time evolution of localized states in Lieb lattices. Unexpectedly, this subject was found to be related to classical precession systems and to the subtleties of vector potentials. Indeed, we found that as one slowly introduces a magnetic field perpendicular to the Lieb lattice, two zero-energy eigenstates leave the flat band and rejoin it periodically in the magnetic flux. This causes an initially-localized eigenstate to abruptly decrease or increase its localized character whenever those two eigenstates join the flat band. The loss or gain of localized component is justified by the difference in the symmetries of the lattice and the vector potential associated to the applied magnetic field. In fact, if one chooses a vector potential with the same symmetry as the lattice, the sudden jumps cease to occur. While one might argue that the physical characteristics of the magnetic field are independent of the chosen gauge, it is also a fact that a time-dependent vector potential generates an electric field. It so happens that a three-level toy model, with a zero-energy state and two states which periodically cross the energy of the first state, correctly reproduces this behavior. Furthermore, the solution of this toy model (a three-component time-dependent vector) can be mapped onto a classical precession motion, with a uniformly-rotating precession vector. In the future, we aim to extend this kind of study to other flat-band systems, like the AB_2 chain. The results have been submitted to Physical Review B and the submitted manuscript is available as

J. D. Gouveia, I. A. Maceira and R. G. Dias, *Time evolution of localized states in Lieb lattices.* arXiv:1607.04326 [quant-ph] (2016)

In Chapter 7, we present the results of our mean-field analysis of the Hubbard model in a Lieb lattice, in the form of a magnetic phase diagram. The diagram was obtained using

standard mean-field theory, which assumes constant magnetization throughout the lattice. We additionally assumed that the electron distribution among the sublattices was the same as the tight-binding case (non-interacting electrons). Even with these simplifications, and even though there are numerous similar studies for the square lattice in the literature, there was no other diagram of the sort for the Lieb lattice. The phase diagram obtained for the Lieb lattice is qualitatively similar to that of the square lattice far from half-filling (ferromagnetism for high U, paramagnetism otherwise). At half-filling the Lieb lattice displays ferrimagnetism, i.e. each sublattice is ferromagnetic, the full lattice is antiferromagnetic, and the magnetization per unit cell is finite due to the different number of atoms of each sublattice. This contrasts with the well-known antiferromagnetic ground state of the square lattice at half-filling. In fact, this ferrimagnetism at half-filling is a consequence of Lieb's theorem, and therefore serves as qualitative confirmation of our mean-field results. An important point reflected by the phase diagram is that, for fillings corresponding to the flat band, we are always in the strong-coupling limit.

While Lieb's theorem predicts a specific value of magnetization per unit cell at half-filling, independent of U, our results only yield the correct value at high U. This discrepancy between mean-field results and exact ones is more easily noticeable in the Lieb lattice than in the square lattice: when assuming the same magnetization on all sites of a bipartite square lattice, the total magnetization per unit cell will be zero (agreeing with Lieb's theorem), even if the on-site magnetization given by mean-field calculations is wrong. The results may be considered somewhat disappointing in terms of correctness, but constituted the motivation for our using the generalized Hartree-Fock theory, a study whose results are presented in Chapter 7.

In order to fix the quantitatively wrong results of our standard mean-field approach of the Hubbard model in a Lieb lattice, we allowed the lattice to have a different magnetization on each sublattice, and allowed the particle density to deviate from its non-interacting values. For that, a more complex mean-field approach was followed. This approach, which takes into account the correspondence between Hartree-Fock self-consistency and saddle points of the mean-field energy, is relatively old (around 20 years old) but, as far as our search led us, ours was the first instance of application of this method to a system which is known to display charge density modulation. As it turned out, our new results agree with Lieb's theorem and the uniform density theorem, in both the $U = 0$ and $U = \infty$ limits. More specifically, at half-filling, the magnetization of each unit cell saturated at the correct value of $1/2$ and the electrons were distributed uniformly throughout the two sublattices. Moreover, the mean-field calculations produced the correct profile for the relative filling of the sublattices in both strong- and non-interacting regimes, and for any value of lattice filling. Our results thus show that the mean-field theory is more reliable than one might expect.

The results of these two chapters were published in the following two papers

J. D. Gouveia and R. G. Dias, *Magnetic phase diagram of the Hubbard model in the Lieb lattice*. Journal of Magnetism and Magnetic Materials, Volume 382, 15 May 2015, Pages 312-317

DOI: 10.1016/j.jmmm.2015.02.005

J. D. Gouveia and R. G. Dias, *Spin and charge density waves in the Lieb lattice*. Journal of Magnetism and Magnetic Materials, Volume 405, 1 May 2016, Pages 292-303

DOI: 10.1016/j.jmmm.2015.12.096

Many questions remain unanswered or open to further exploration. For example, in the case of the mean-field magnetic phase diagram of the square lattice, we expect that dividing the lattice into more than two sublattices yields even lower ground-state energies. On another topic, can analytic solutions of the quantum spin queue model for more than one inverted spin or additional holes be obtained? Recalling the fact that our origami rules in the $U \to \infty$ limit imply a ferromagnetic spin configuration in a small region around the localized hole state, what consequences does that imply for the magnetic behavior of the material as a whole? Concerning the time evolution of localized states, can our conclusions be adapted and/or generalized in some way for other kinds of perturbations? These are questions we intend to address in the future.